

AN ABSTRACT OF THE THESIS OF

Anthony F. Bouchard for the degree of Master of Science in

Electrical & Computer Engineering presented on July 9, 1999. Title:

ACTFEL Device Simulation with Impact Ionization Using a Two-Sheet Charge Model

Redacted for Privacy

Abstract approved:

John F. Wager

The main achievement of this thesis is the development of a two-sheet charge simulation model with space charge creation by trap-to-band impact ionization to describe the electrical characteristics of alternating-current thin-film electroluminescent (ACTFEL) devices. The two-sheet charge model localizes all of the space charge in the phosphor region of an ACTFEL device at two sheets of positive charge. The locations of these two sheets represent charge centroids within the phosphor region of the ACTFEL device. Simulation results demonstrate that space charge creation by trap-to-band impact ionization yields more capacitance-voltage (C-V) and internal charge-phosphor field ($Q - F_p$) overshoot than when space charge is created by field emission from bulk traps within the phosphor region of an ACTFEL device. The increased C-V and $Q - F_p$ overshoot observed in simulation when trap-to-band impact ionization is employed as the mechanism for space charge creation corresponds to trends observed experimentally in SrS ACTFEL devices.

Several of the model parameters are varied to determine the sensitivity of the simulation to these parameters. The parameters with the greatest influence on simulation performance include the trap density in the phosphor region, the value of the series resistance used in the experimental test circuit, and the characteristic fields for trap-to-band impact ionization, band-to-band impact ionization, and electron capture.

©Copyright by Anthony F. Bouchard

July 9, 1999

All rights reserved

ACTFEL Device Simulation with Impact Ionization Using a Two-Sheet Charge Model

by

Anthony F. Bouchard

A THESIS

submitted to

Oregon State University

in partial fulfillment of
the requirements for the
degree of

Master of Science

Completed July 9, 1999
Commencement June 2000

Master of Science thesis of Anthony F. Bouchard presented on July 9, 1999

APPROVED:

Redacted for Privacy

Major Professor, representing Electrical & Computer Engineering

Redacted for Privacy

Chair of the Department of Electrical & Computer Engineering

Redacted for Privacy

Dean of the Graduate School

I understand that my thesis will become part of the permanent collection of Oregon State University libraries. My signature below authorizes release of my thesis to any reader upon request.

Redacted for Privacy

Anthony F. Bouchard, Author

ACKNOWLEDGMENT

I would like to thank Dr. John Wager for his help and support during the process of researching and writing this thesis.

I would also like to thank Paul Keir and John Hitt for their sharing their expertise on ACTFEL device modeling. Thanks also to Beau Baukol, Arkady Grudzinsky, and Jeff Bender for their assistance.

This work was sponsored by the Defense Advanced Research Projects Agency under contract MDA 972-94-C-0023 and under the Phosphor Technology Center of Excellence contract MDA 972-93-1-0030.

TABLE OF CONTENTS

	<u>Page</u>
1. INTRODUCTION	1
2. ACTFEL DEVICE BASICS AND LITERATURE REVIEW OF ACTFEL DEVICES	4
2.1 Device Structure	4
2.2 Device Operation	5
2.3 Phosphor Space Charge	9
2.4 Previous Modeling Efforts	11
2.4.1 SPICE Modeling	11
2.4.2 Device Physics Modeling	14
2.4.3 State-Space Modeling	15
2.5 Electrical Characterization	16
2.5.1 The Experimental Test Set-up	16
2.5.2 External Charge - External Voltage (Q-V) Analysis	17
2.5.3 Capacitance - Voltage (C-V) Analysis	19
2.5.4 Internal Charge - Phosphor Field ($Q - F_p$) Analysis	20
3. DERIVATION OF DEVICE EQUATIONS FOR THE TWO-SHEET CHARGE MODEL	23
3.1 The Two-Sheet Charge Model	23
3.1.1 Basic Operation of the Modeling Program	23
3.1.2 The Quasi-Static Two-Sheet Charge Model	24
3.1.3 The Dynamic Two-Sheet Charge Model	27
3.2 Electron Emission from Insulator-Phosphor Interfaces	35
3.3 Electron Multiplication	38
3.3.1 Trap-to-Band Impact Ionization	38
3.3.2 Band-to-Band Impact Ionization	42
3.4 Field-Dependent Capture	44
3.5 Effects of the Test Circuit on Device Characterization	48
3.6 Model Stability	52
4. SIMULATION RESULTS	56
4.1 Static and Dynamic Space Charge	56

TABLE OF CONTENTS (Continued)

	<u>Page</u>
4.2 Simulation Results Using the Two-Sheet Charge Model with Space Charge Creation by Field Emission.....	58
4.2.1 Simulation Results Using Standard Voltage Pulses.....	58
4.2.2 Simulation Results Using Long Voltage Pulses.....	61
4.3 Simulation Results With Space Charge Creation by Trap-to-Band Impact Ionization.....	65
4.4 Simulation Results With Effects of the Test Circuit Considered.....	67
4.4.1 Simulation With Space Charge Creation by Trap-to-Band Impact Ionization.....	68
4.4.2 Variation of Simulation Parameters.....	72
4.4.3 Simulation With Space Charge Creation by Field Emission.....	79
4.4.4 Summary of Simulation Results.....	82
5. CONCLUSIONS AND RECOMMENDATIONS FOR FUTURE WORK.....	84
5.1 Achievements.....	84
5.2 Recommendations for Future Work.....	85
BIBLIOGRAPHY.....	88

LIST OF FIGURES

<u>Figure</u>	<u>Page</u>
2.1 ACTFEL device structure.....	5
2.2 The bipolar trapezoidal waveform.	6
2.3 ACTFEL device energy-band diagram under thermal equilibrium.	7
2.4 ACTFEL device energy-band diagram under a positive applied voltage. .	8
2.5 ACTFEL device energy-band diagram showing a counterfield in the phosphor region.	9
2.6 ACTFEL device energy-band diagram under a negative applied voltage. .	10
2.7 ACTFEL device energy-band diagram for a device with positive phosphor space charge.	11
2.8 ACTFEL device energy-band diagram showing space charge creation by trapping of holes created by band-to-band impact ionization.	12
2.9 The capacitive stack equivalent circuit.	13
2.10 The experimental test circuit.....	17
2.11 A typical experimental Q-V curve.	18
2.12 A typical experimental C-V curve for a ZnS:Mn device.	19
2.13 A typical experimental C-V curve for an SrS ACTFEL device.	20
2.14 A typical experimental $Q - F_p$ curve.	21
3.1 The two-sheet charge model of the ACTFEL device.	25
3.2 Energy band diagram showing current flow in the two-sheet charge model.	28
3.3 Energy band diagram showing current flow for a negative applied voltage.	33
3.4 Energy band diagram showing current flow during unusual field conditions in which both phosphor-insulator interfaces emit electrons.	34
3.5 The three field emission mechanisms from the phosphor-insulator interfaces.	36
3.6 A trap-to-band impact ionization event.....	39
3.7 Band-to-band impact ionization.	43
3.8 Field situation with trapping at the space charge layer likely.	46

LIST OF FIGURES (Continued)

<u>Figure</u>	<u>Page</u>
3.9 Field situation with trapping at the space charge layer unlikely.	47
3.10 The ACTFEL device test circuit.	48
3.11 The iterative procedure used to include external test circuit effects.....	50
3.12 Energy band diagram illustrating feedback effects during the rising edge of a positive voltage pulse for (1) interface emission (negative feedback), (2) space charge creation (positive feedback), and (3) band-to-band impact ionization (negative feedback). A downward arrow indicates a lowering of the energy band at a sheet in the phosphor region, while a curved arrow indicates a reduction in the slope of a portion of the energy band..	53
4.1 The space charge creation cycle.	57
4.2 Simulated (solid line) and experimental (dashed line) $Q - F_p$ curves for a SrS:Ce ACTFEL device using the field emission program.	60
4.3 Simulated (solid line) and experimental (dashed line) $Q - F_p$ curves for a SrS:Ce ACTFEL device with greater simulated phosphor field overshoot.	61
4.4 Simulated (solid line) and experimental (dashed line) C-V curves for a SrS:Ce ACTFEL device with a small amount of simulated overshoot.	62
4.5 The long trapezoidal voltage pulse waveform.	62
4.6 Simulated (solid line) and experimental (dashed line) $Q - F_p$ curves for a SrS:Ce device obtained using long pulses.	63
4.7 Simulated (solid line) and experimental (dashed line) C-V curves obtained for a SrS:Ce ACTFEL device using long pulses.	64
4.8 Electron emission rate from the space charge layer closest to the cathodic insulator-phosphor interface for both field emission and trap-to-band impact ionization.....	65
4.9 Generic simulated $Q - F_p$ curve obtained using the two-sheet charge model with space charge creation by trap-to-band impact ionization.	66
4.10 Generic simulated C-V curve obtained using the two-sheet charge model with space charge creation by trap-to-band impact ionization.	67

LIST OF FIGURES (Continued)

<u>Figure</u>	<u>Page</u>
4.11 Simulated $Q - F_p$ curve obtained using the two-sheet charge model with space charge creation by trap-to-band impact ionization and effects of the test circuit considered, with $R_s = 400 \Omega$ and $C_s = 101 \text{ nF}$	68
4.12 Simulated C-V curve obtained using the two-sheet charge model with space charge creation by trap-to-band impact ionization and effects of the test circuit considered, with $R_s = 400 \Omega$ and $C_s = 101 \text{ nF}$	69
4.13 Simulated (solid line) and experimental (dashed line) $Q - F_p$ curves for a SrS:Ce ACTFEL device with matching maximum field and charge. . . .	72
4.14 Family of simulated $Q - F_p$ curves with N_T set at $1.5 \times 10^{17} \text{ cm}^{-3}$ (solid line), $2 \times 10^{17} \text{ cm}^{-3}$ (dashed line), and $2.3 \times 10^{17} \text{ cm}^{-3}$ (dotted line). Nominal simulation parameters are given in Table 4.2.	73
4.15 Family of simulated C-V curves with N_T set at $1.5 \times 10^{17} \text{ cm}^{-3}$ (solid line), $2 \times 10^{17} \text{ cm}^{-3}$ (dashed line), and $2.3 \times 10^{17} \text{ cm}^{-3}$ (dotted line). Note that maximum C-V overshoot is obtained for the intermediate trap density case. Nominal simulation parameters are given in Table 4.2.	74
4.16 Simulated $Q - F_p$ curves with R_s varied from 400Ω (solid line) to 1000Ω (dashed line). Nominal simulation parameters are given in Table 4.2. . .	75
4.17 Simulated C-V curves with R_s varied from 400Ω (solid line) to 1000Ω (dashed line). Nominal simulation parameters are given in Table 4.2. . . .	76
4.18 Family of simulated $Q - F_p$ curves with the characteristic field for trap-to-band impact ionization set at 2.6 MV/cm (solid line), 3.0 MV/cm (dashed line), and 3.4 MV/cm (dotted line). Nominal simulation parameters are given in Table 4.2.	77
4.19 Family of simulated C-V curves with the characteristic field for trap-to-band impact ionization set at 2.6 MV/cm (solid line), 3.0 MV/cm (dashed line), and 3.4 MV/cm (dotted line). Nominal simulation parameters are given in Table 4.2.	78
4.20 Simulated family of C-V curves with the characteristic field for band-to-band impact ionization set at 2.7 MV/cm (solid line), 3.1 MV/cm (dashed line), and 4.0 MV/cm (dotted line). $R_s = 600 \Omega$ for this plot. Note that maximum overshoot is obtained for the intermediate characteristic field value. Nominal simulation parameters are given in Table 4.2.	79

LIST OF FIGURES (Continued)

<u>Figure</u>	<u>Page</u>
4.21 Family of simulated $Q - F_p$ curves with the characteristic field for electron capture set at 3 MV/cm (solid line), 5.0 MV/cm (dashed line), and 7.0 MV/cm (dotted line). Nominal simulation parameters are given in Table 4.2.	80
4.22 Simulated $Q - F_p$ curve obtained using the two-sheet charge model with space charge creation by field emission and effects of the test circuit considered for a SrS ACTFEL device	81
4.23 Simulated C-V curve obtained using the two-sheet charge model with space charge creation by field emission and effects of the test circuit considered for a SrS ACTFEL device.....	82
5.1 Experimental $Q - F_p$ curve demonstrating charge collapse.	86

LIST OF TABLES

<u>Table</u>		<u>Page</u>
4.1	Simulation parameters for the field emission two-sheet charge model.	59
4.2	Simulation parameters for the trap-to-band impact ionization model.	71

ACTFEL Device Simulation with Impact Ionization Using a Two-Sheet Charge Model

1. INTRODUCTION

In the past decade, computer use in society has become increasingly pervasive. While computers were once used only by a few, computers today are found in an ever increasing number of locations, from businesses to homes to cars and even tanks. Because of the large number of applications in which computers are used, traditional display devices may not always be appropriate for a given situation. While a cathode ray tube (CRT) is fine for personal computers, a bulky CRT may not be ideal for many computer installations.

For many applications, a display device smaller than a CRT is desirable. The most commonly used of the flat display devices are liquid-crystal displays (LCD's). In addition to flatness and low weight, LCD's have the advantage of being a relatively mature technology. This technology suffers, however, from a number of drawbacks. LCD's are not very bright, they have a poor viewing angle, and they are not highly durable. These weaknesses make LCD's a less than ideal choice for military and other applications where a flat panel display is desirable. Because of these LCD performance limitations, a number of other flat panel display technologies are in development. Plasma displays (PD's) show potential as a flat panel solution for large display devices, but they still have a poor viewing angle like LCD's. A display technology which appears to solve many of the problems of the other technologies is electroluminescent (EL) technology. Although EL technology has several variants, perhaps the most interesting form of EL technology is alternating-current thin-film electroluminescent (ACTFEL) technology. ACTFEL displays offer the potential for high brightness, wide viewing angle, and good durability in a flat panel display.

Despite their promise, ACTFEL displays are not yet widely available because of the immaturity of ACTFEL technology. While a yield rate of 75% of the die on given wafer for integrated circuits is considered acceptable, 100% of the pixels of an ACTFEL display must be functional. ACTFEL devices also operate at high voltages, making the design of the display driving electronics non-trivial. Although the internal operation of ACTFEL devices is much better understood than it was just a few years ago, the variation in device performance seen in different types of ACTFEL devices cannot be fully explained at present. Electrical characterization of ACTFEL devices reveals significant variations in device performance with changes in phosphor material, dopant, and method of dopant deposition. The typical method of assessing the impact of a certain process step on device performance is simply to make a new device and then observe its properties. While this method is acceptable during the early stages of device development, it becomes less acceptable as the technology matures. If ACTFEL display devices become widespread in the future, design engineers will want to have tools that allow them to reliably estimate device performance before the device is fabricated. Additionally, an accurate device physics simulation of a device can serve to confirm theories of device operation.

Obtaining a realistic computer simulation of ACTFEL devices has proven difficult. Others have made progress towards achieving realistic ACTFEL device simulation, but much work remains before a tool is available that can be used by the typical design engineer. Specifically, more work needs to be done to understand how to be able to vary such basic device parameters as phosphor and dopant type and device thickness while obtaining an accurate computer simulation. Also, current ACTFEL device simulators do not realistically model the capacitance-voltage (C-V) overshoot seen when characterizing SrS ACTFEL devices.

The goal of this thesis is to develop an ACTFEL device computer simulation program that allows the user to vary a number of essential ACTFEL device parameters and obtain results which correspond to the electrical characteristics obtainable experimentally.

An additional aim of this thesis is to obtain a realistic simulation of C-V and $Q - F_p$ overshoot and to offer an explanation for the overshoot seen experimentally in some ACTFEL devices.

The organization of this thesis is as follows. Chapter 2 presents an overview of ACTFEL device basics and a summary of literature on the nature of space charge in ACTFEL devices and previous modeling efforts. In Chapter 3, the device physics model used for ACTFEL device simulation in this thesis is presented. Chapter 4 shows the results obtained from simulation in comparison to experimental results for various types of ACTFEL devices. Chapter 5 contains conclusions and recommendations for future work.

2. ACTFEL DEVICE BASICS AND LITERATURE REVIEW OF ACTFEL DEVICES

2.1 Device Structure

An ACTFEL device is a two-terminal solid-state device consisting of a layer of phosphor material sandwiched between two insulator layers. Contacts are found on the outside of the insulator layers, as shown in Fig. 2.1. The entire device is typically deposited on a glass substrate. The phosphor material is usually a II-VI compound, and the most common devices have ZnS or SrS phosphor layers. The phosphor layer is typically 500-1000 nm thick and is doped with a luminescent impurity. The insulator layers are typically on the order 200 nm thick each and are usually both made of the same material, aluminum-titanium oxide (ATO), if atomic-layer epitaxy (ALE) is employed. Occasionally, some types of SrS devices are created with asymmetrical insulator layers, e.g. one ATO insulator layer and the other barium tantalate (BTO). The contact material on the glass substrate side of the device is made of a transparent conductor, commonly indium-tin oxide (ITO). The transparent nature of ITO allows light to shine through it and be viewed on the opposite side of the glass substrate. The back contact of the ACTFEL device is typically aluminum, and the glass substrate is usually 1 mm thick. The ACTFEL devices considered in this thesis are grown primarily by ALE.

The motivation for using different phosphor materials and different dopants is to achieve different color displays. One of the older phosphor materials is ZnS:Mn, which results in a yellow display. The SrS class of devices result in blue-green to blue displays, with SrS:Ce, SrS:Cu and SrS:Cu,Ag all resulting in slightly different peak emission wavelengths. One of the goals of ACTFEL device research is to produce devices which have peak emissions at specific locations in the red, green, and blue regions. This will allow for the creation of full-color RGB displays. Another class of ACTFEL devices now being

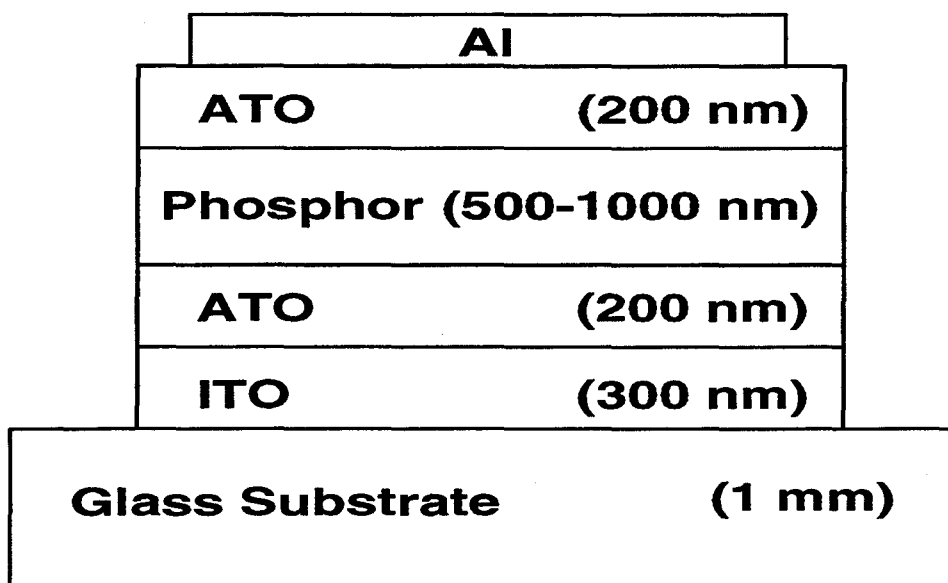


Figure 2.1: ACTFEL device structure.

researched are white devices, which consist of a hetero-phosphor layer and emit light over a broad range of wavelengths. SrS ACTFEL devices are the focus of the modeling effort presented in this thesis.

2.2 Device Operation

Historically, electroluminescence has been observed by the application of a high voltage AC signal to an electroluminescent material. This situation is also the case for ACTFEL devices. The bipolar trapezoidal waveform of Fig. 2.2 is the driving force applied throughout the remainder of this thesis. As shown, the applied voltage pulses have rise and fall times of $5 \mu\text{s}$ and a total duration of $40 \mu\text{s}$. These pulses are usually applied at a frequency of 1000 Hz with a maximum amplitude of around 150 V. The bipolar trapezoidal waveform is applied to the Al electrode relative to the grounded ITO electrode.

High voltage excitation waveforms are required to produce light in ACTFEL devices. Figure 2.3 shows an idealized ACTFEL device energy-band diagram under the condition

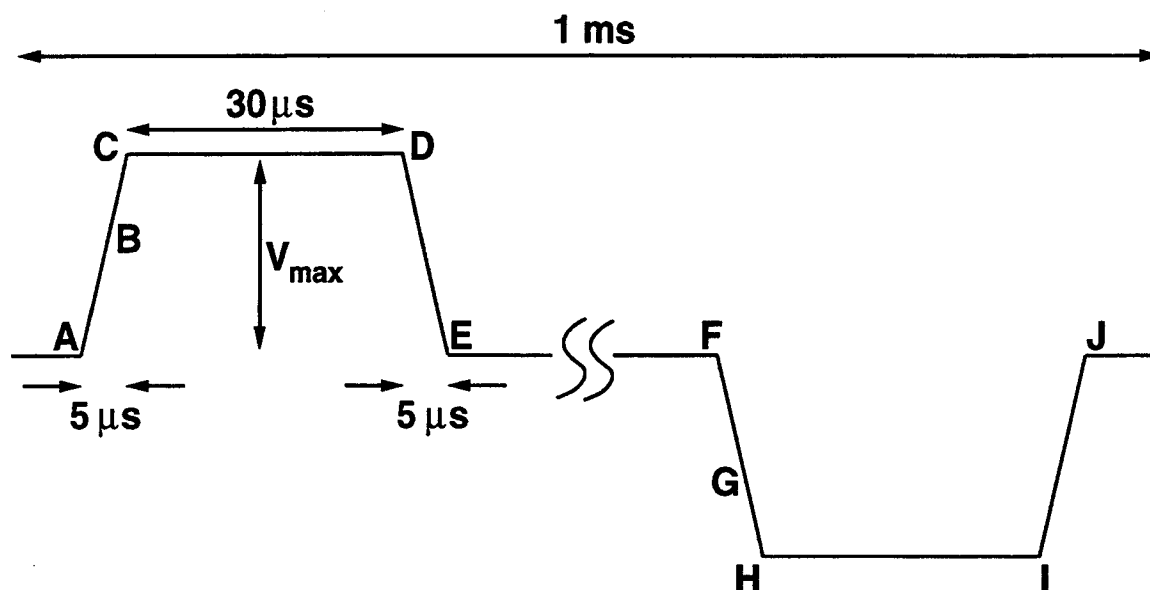


Figure 2.2: The bipolar trapezoidal waveform.

of thermal equilibrium. The Al electrode is at the right side of the device, as shown in Fig. 2.3; this convention is maintained throughout the remainder of this thesis. The flat-band condition of the ACTFEL device, as shown in Fig. 2.3, rests on the assumption of a symmetrical distribution of interface states at each of the phosphor-insulator interfaces of the ACTFEL device. This assumption is also maintained throughout the remainder of this thesis.

As a positive voltage pulse is applied to the Al electrode, the conditions shown in Fig. 2.4 result. When a certain threshold voltage is reached, electrons are emitted from states in the phosphor-insulator interface on the left side of Fig. 2.4 and travel across the phosphor layer where they are captured at the opposite phosphor-insulator interface. The electron-emitting interface is referred to as the cathodic interface while the electron receiving interface is called the anodic interface. Energetic conduction band electrons in the phosphor region may strike impurity atoms as they make their way across the device.

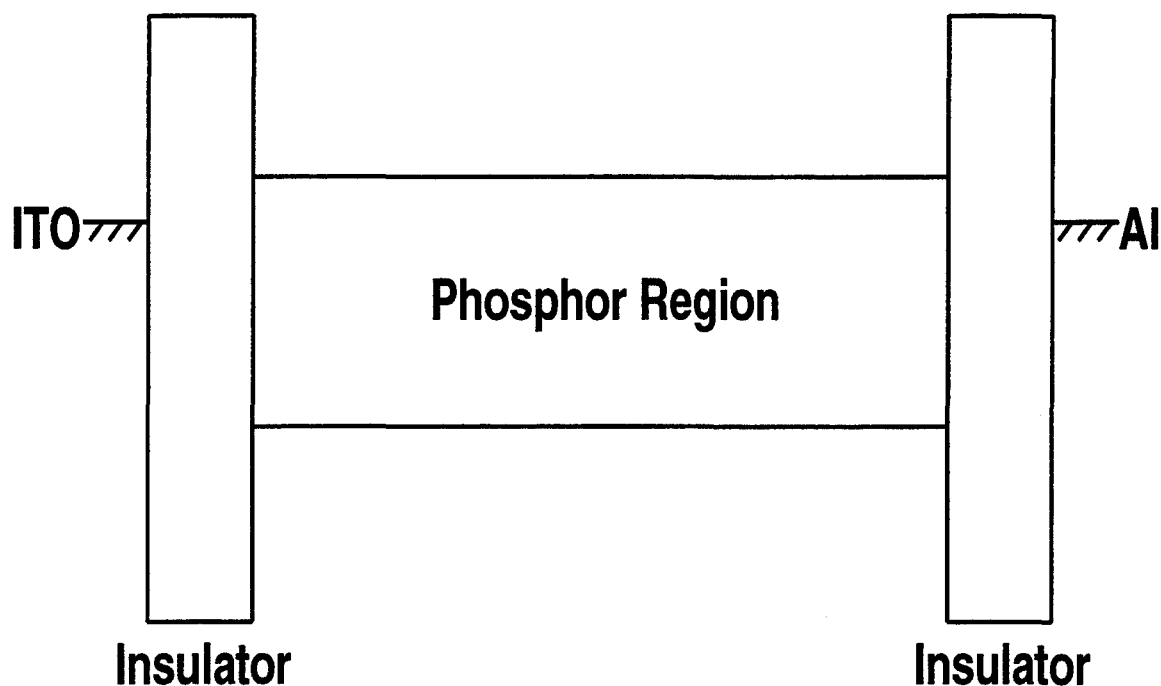


Figure 2.3: ACTFEL device energy-band diagram under thermal equilibrium.

These collisions can cause energy transfers that promote electrons of the impurity atoms to excited states. As these excited impurity atom electrons decay back to their ground states, photons can be emitted. These photons result in the light output of ACTFEL devices.

After the threshold voltage has been reached and the applied voltage pulse achieves its maximum value, a large number of electrons have transited the phosphor layer. The capture of these electrons at the anodic interface leads to a net negative charge at this interface. Similarly, positive charge now exists at the cathodic interface because of the interface states that have been emptied through electron emission. This new distribution of interface charge leads to a counterfield within the device that is opposite in polarity to the electric field due to the applied voltage pulse, as shown in Fig. 2.5. This counterfield condition persists during the interpulse interval between applied voltage pulses. If the

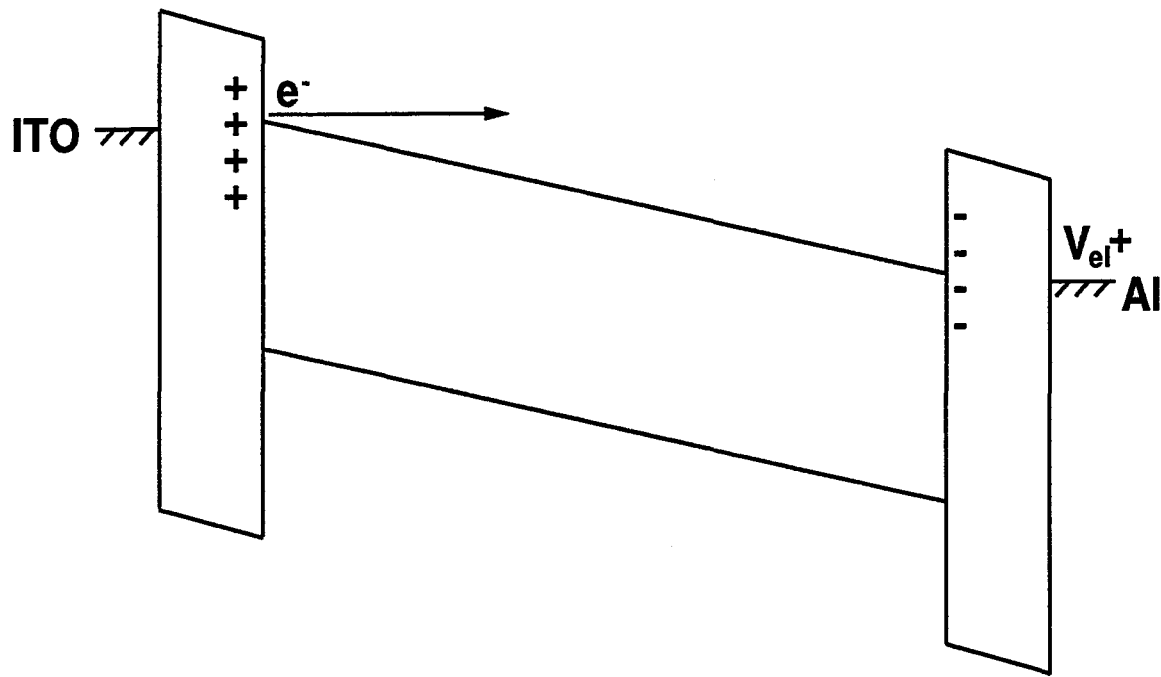


Figure 2.4: ACTFEL device energy-band diagram under a positive applied voltage.

counterfield is of a large enough magnitude, electrons can tunnel from the formerly anodic interface into the phosphor region. Such charge flow during the interpulse interval is known as leakage charge.

When a negative voltage pulse is applied to the Al electrode at the end of the interpulse interval, the remaining electric field in the phosphor region now aids in the emission of electrons from the right interface in Fig. 2.6, now the cathodic interface. The threshold voltage for electron emission from the cathodic interface is now less than that found for the first positive pulse applied to a device under flat-band conditions. After the first negative voltage pulse, another interpulse interval follows and then the cycle begins again. Eventually the threshold voltage, leakage charge, and other device characteristics will reach steady-state values.

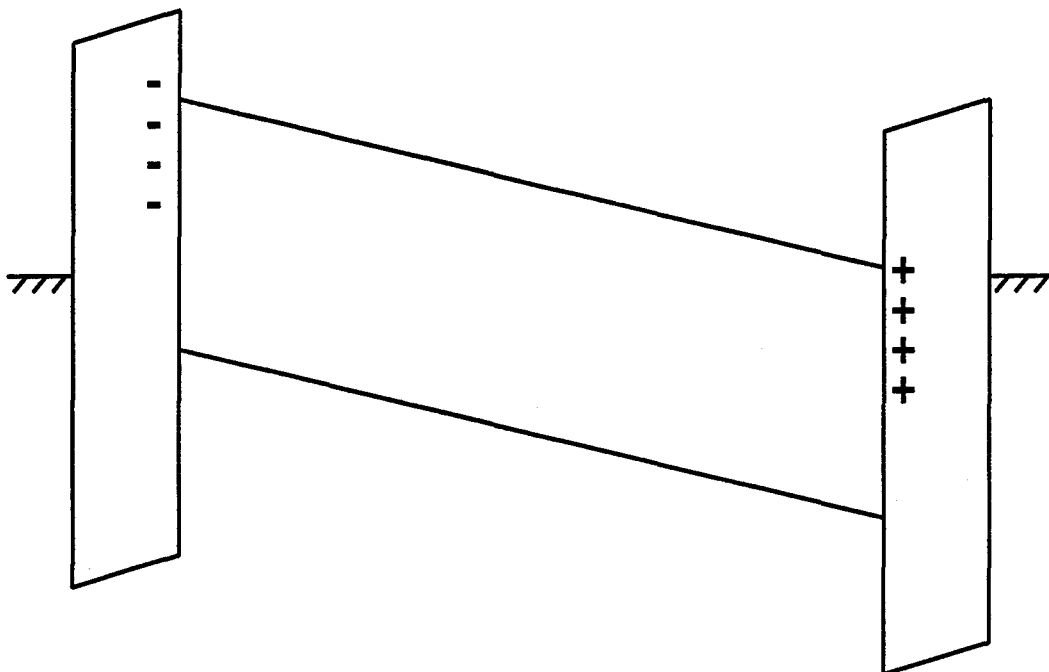


Figure 2.5: ACTFEL device energy-band diagram showing a counterfield in the phosphor region.

2.3 Phosphor Space Charge

Previous work has shown that space charge in the phosphor region is an important aspect of the performance of ACTFEL devices. [1, 2, 3, 4] Phosphor space charge effects have been cited as a cause of the overshoot seen in experimental C-V and $Q - F_p$ curves. [3, 4] Figure 2.7 shows the energy-band diagram of an ACTFEL device with positive space charge in the phosphor region and a positive voltage applied to the Al electrode. The presence of space charge in the phosphor region perturbs the electric field in this region, such that it is no longer a constant, as in Sec. 2.2. This variable field in the phosphor region complicates the problem of modeling ACTFEL devices. [3] As Fig. 2.7 shows, positive space charge in the phosphor region leads to a higher field near the cathodic interface and a lower field near the anodic interface. The higher cathodic region field

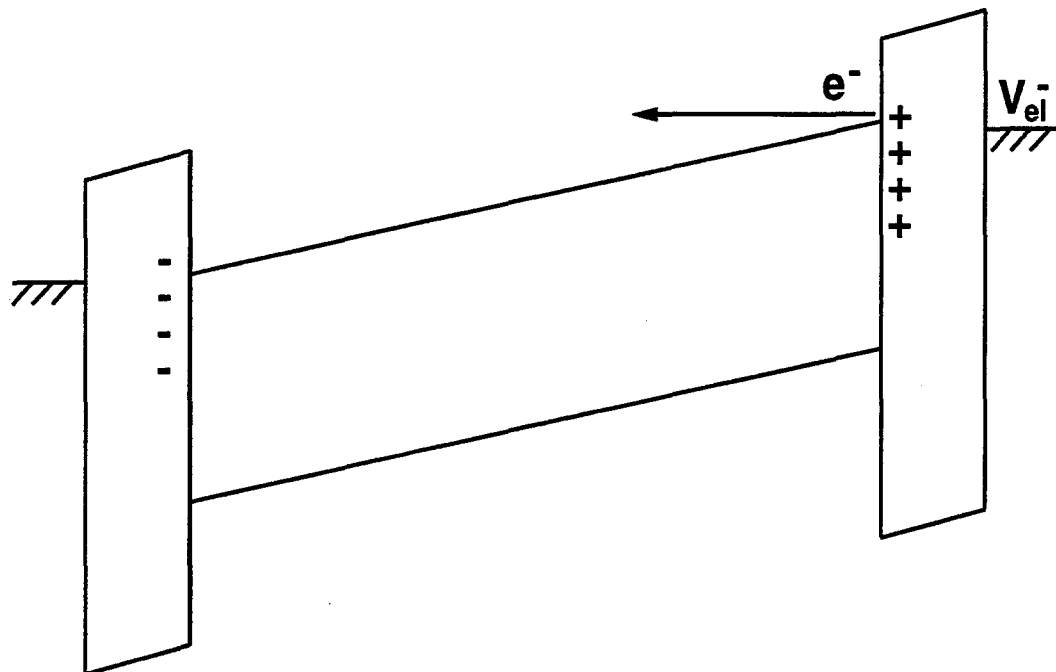


Figure 2.6: ACTFEL device energy-band diagram under a negative applied voltage.

increases the electron emission rate from this interface, and can therefore lead to model instability.

Researchers have proposed several different possible mechanisms for phosphor space charge creation. One of the most often encountered theories in the literature is that phosphor space charge is created by the trapping of holes created by band-to-band impact ionization. [1, 2, 5, 6] This process is shown in Fig. 2.8. Although the high fields in the phosphor region of the ACTFEL device certainly increase the probability that band-to-band impact ionization occurs, high electric fields also reduce the probability of capture processes. This means that hole capture may not be the most likely mechanism for space charge creation in ACTFEL devices. Others have proposed that space charge is created by field emission from bulk traps within the phosphor region or by trap-to-band impact ionization. [3, 4] It is important to note that because all of the space charge creation

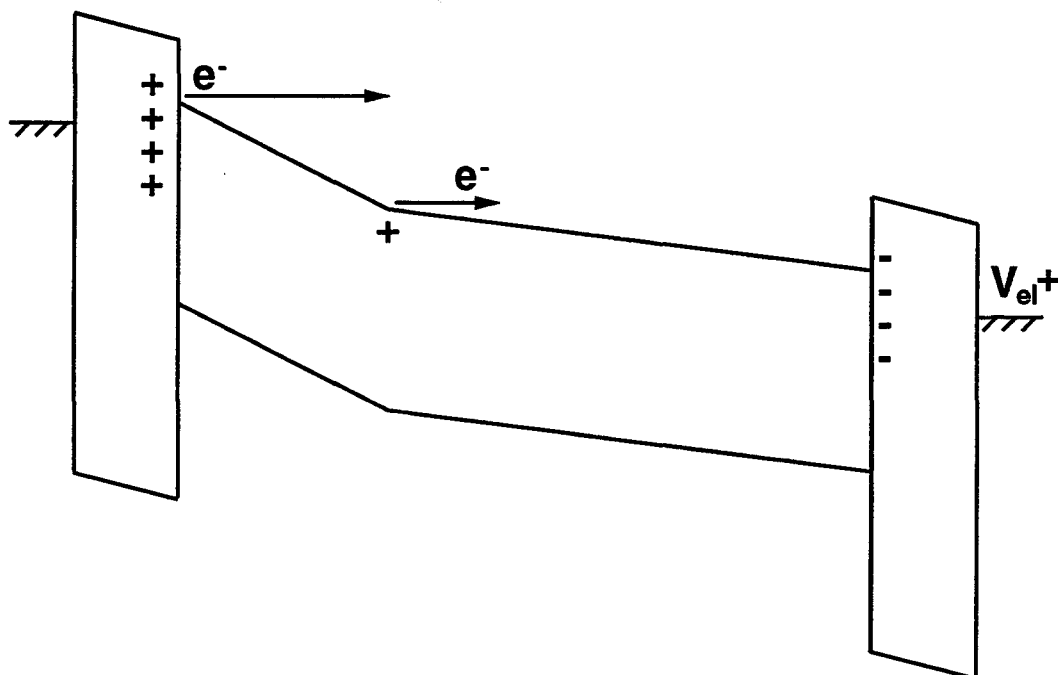


Figure 2.7: ACTFEL device energy-band diagram for a device with positive phosphor space charge.

mechanisms mentioned above result in electron emission into the phosphor conduction band, all mechanisms result in the creation of positive phosphor space charge.

2.4 Previous Modeling Efforts

This section presents a summary of previous modeling efforts in several different categories of modeling.

2.4.1 SPICE Modeling

The goal of SPICE modeling is to represent the ACTFEL device as an equivalent circuit consisting of basic circuit elements. The external voltage applied across an ACTFEL device, v_{el} , is not dropped solely across the phosphor region. Part of v_{el} is dropped across the two insulator layers on either side of the phosphor region. This situation leads to

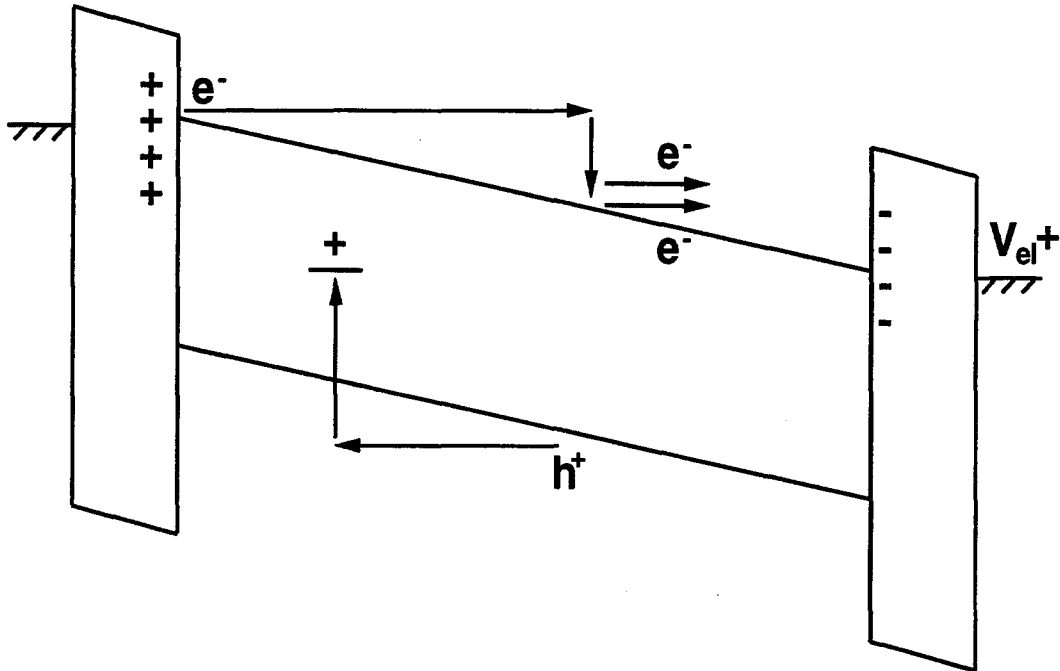


Figure 2.8: ACTFEL device energy-band diagram showing space charge creation by trapping of holes created by band-to-band impact ionization.

one of the simplest ways of viewing an ACTFEL device, as three capacitors in series; two capacitors associated with the insulators, c_{i1} and c_{i2} , and a phosphor region capacitance, c_p , as shown in Fig. 2.9. [7] When the turn-on voltage is reached and electron emission from the cathodic interface begins, the phosphor region is short circuited. The dynamic capacitance of a short circuit is infinity, so the total device capacitance above turn-on is the series combination of the two insulator capacitances, c_i . This turn-on effect is modeled by the back-to-back zener diodes shorting out the phosphor region in Fig. 2.9. Although this simple model is sufficient to simulate the basic characteristics of an ACTFEL device, it cannot accommodate second-order effects such as phosphor space charge.

Keir has proposed a much more complicated SPICE model [3], which can account for space charge creation in the phosphor region. This model involves the use of many current

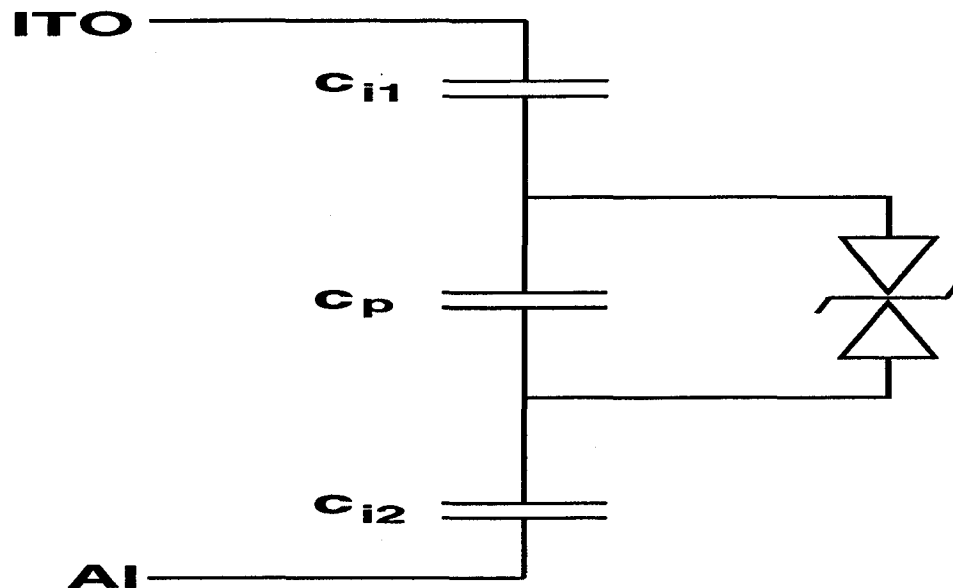


Figure 2.9: The capacitive stack equivalent circuit.

sources as well as passive circuit elements and produces more realistic simulation results than the capacitive stack. Some of the most interesting and realistic SPICE modeling has been performed recently by Bender and Wager. [8] Bender and Wager propose modeling the phosphor region of the ACTFEL device as a Fowler-Nordheim diode, which results in a close match between simulated and experimental data.

Although SPICE modeling is typically rather easy to implement and is a useful tool for circuit designers, it is not always the most satisfying form of device modeling. This is because SPICE equivalent circuits are often just simplified versions of more complicated models. Such processes as electron emission from a phosphor-insulator interface and impact ionization cannot be modeled easily by equivalent circuit elements. As a result, the parameters used in SPICE simulation are often far removed from their relation to actual physical device parameters.

2.4.2 Device Physics Modeling

Device physics modeling is the type of modeling in which simulation parameters are most closely related to the physics of the actual ACTFEL device. Device physics modeling also typically achieves the most accurate simulated results, but at a cost of increased model complexity and simulation time. Most of the modeling work with ACTFEL devices has been attempted from a device physics approach.

The early work in device physics modeling usually involved modeling an ACTFEL device with no phosphor space charge. [9] Although these models are capable of simulating the basic features of the ACTFEL device experimental curves, incorporating phosphor space charge into the model is necessary to achieve more accurate simulation. Several different methods of incorporating phosphor space charge into the model have been attempted. Jarem and Singh [1] assumed a homogeneous space charge distribution in the phosphor region and an amount of space charge equal to either zero or some maximum value. This is a considerable simplification of the actual situation, because the internal phosphor field conditions often dictate non-uniform space charge creation in the phosphor region. Neyts [2] incorporated a non-homogeneous, steady-state space charge distribution into his model, with space charge creation by trapping of holes created by band-to-band impact ionization. Modeling the space charge distribution as steady-state is equivalent to assuming that the space charge in the phosphor region is static. This assumption may explain many of the effects seen in ZnS devices, but is not appropriate for the simulation of dynamic space charge which is usually prevalent in SrS devices.

Singh *et al.* [10, 11] later modified their earlier model to incorporate space charge by dividing the phosphor region into several sections in which the space charge is located. Each of these sections can capture electrons transiting the phosphor region and emit electrons through thermal emission and field-assisted tunneling. A more advanced treatment of phosphor space charge was proposed by Keir [3] with his sheet-charge model. This model locates all the space charge at sheets in the phosphor layer. Space charge is created

by either field emission from bulk traps or by trap-to-band impact ionization. By changing the location of the sheets, the distribution of space charge in the phosphor region is controlled. Keir mainly presents results for the version of his model with one sheet of space charge in the phosphor region. The one-sheet charge model may be sufficient for simulation of ZnS devices, but more sheets are required to simulate the concomitant creation and annihilation of dynamic space charge.

In addition to the varying ways to model space charge, different treatments of electron emission from the insulator-phosphor interfaces have been proposed. Singh *et al.* [1, 10, 11, 12] assumed interface emission due to tunneling from interface states. In order to decrease the computational time required, Neyts [9] solved for the tunneling rate at one value of phosphor electric field and assumed an exponential dependence elsewhere. This simplification does reduce simulation time but does not produce results of the accuracy desired for this thesis. Keir computes the total interface emission rate due to three mechanisms, pure tunneling, phonon-assisted tunneling, and thermal emission. Computing the emission rate due to phonon-assisted tunneling is especially time-consuming. Although pure-tunneling typically is the dominate method of interface emission, the most accurate results under all conditions are achieved by including all three mechanisms in simulation.

2.4.3 State-Space Modeling

A form of device modeling somewhat between SPICE modeling and device physics modeling is state-space modeling. State-space modeling treats the ACTFEL device as a system composed of several elements, each of which is described by a differential equation. Many of the elements in the state-space description of an ACTFEL device are simply circuit elements, such as resistors and capacitors. The elements of the state-space system can, however, be used to describe highly nonlinear processes such as space charge creation which are not easily modelled in SPICE. Additionally, state-space modeling offers the possibility of greater programming simplicity and reduced computational time requirements when compared to device physics modeling.

Despite the advantages of state-space modeling, relatively little work has been done in this regard. Peery attempted to develop a state-space description of an ACTFEL device with phosphor space charge distributed homogeneously in the phosphor region [4], but his simulated results are not as realistic as those typically obtained through device physics simulation. Recent work by Hitt [13] has produced a much better state-space model of an ACTFEL device by adapting the sheet charge model into a system of state-space equations.

2.5 Electrical Characterization

The focus of this thesis is on the simulation of ACTFEL device electrical characterization curves produced by such experimental measurement techniques as external charge - external voltage (Q-V), capacitance - voltage (C-V), and internal charge - phosphor field ($Q - F_p$). Optical characterization techniques such as brightness - voltage (B-V) are not considered. This section presents an explanation of the different electrical characterization techniques and of the experimental test set-up.

2.5.1 The Experimental Test Set-up

A common test circuit often used to obtain raw data to generate the ACTFEL device experimental curves is shown in Fig. 2.10. The excitation waveform applied across the ACTFEL device in this thesis is the bipolar trapezoidal voltage waveform shown in Fig. 2.2. A low voltage version of this waveform is generated by the arbitrary waveform generator (AWG) shown in Fig. 2.10. This signal is then amplified by a high voltage amplifier to achieve the desired maximum applied voltage. R_s is a current-limiting resistor in series with the output of the amplifier and is usually less than 500 Ω . The sense capacitor, c_s , is several orders of magnitude larger than the value of the total ACTFEL device capacitance. This means that the voltage dropped across c_s is quite small. The voltage drop across R_s is also typically quite small, although dynamic space charge creation near device turn-on in SrS devices causes a large current through the ACTFEL device

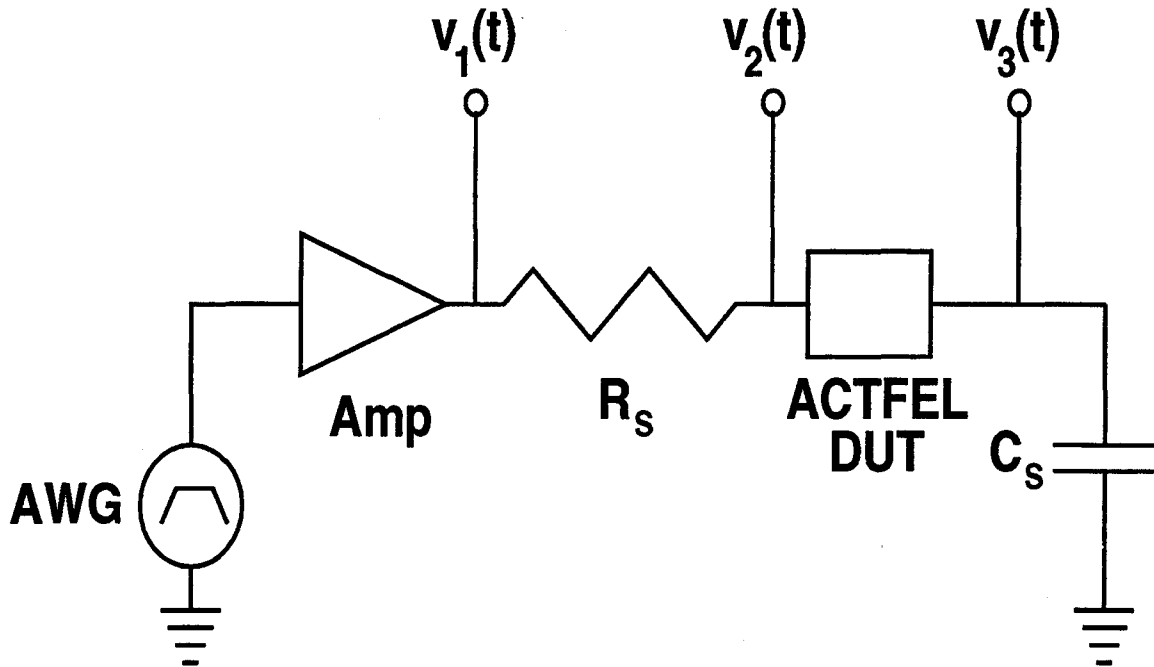


Figure 2.10: The experimental test circuit.

which increases the voltage drop across R_s . Reducing R_s reduces the influence that series resistance has on experimental results but leaves the ACTFEL device more vulnerable to burn-out due to current spikes. The voltages $v_1(t)$, $v_2(t)$, and $v_3(t)$ are sampled to generate the experimental curves.

2.5.2 External Charge - External Voltage (Q-V) Analysis

Q-V curves show the external charge across the entire ACTFEL device as a function of the voltage across the device. Figure 2.11 shows a typical ACTFEL device Q-V curve. The charge across the ACTFEL device is identical to the charge on c_s , which is found from

$$q_{ext}(t) = c_s v_3(t). \quad (2.1)$$

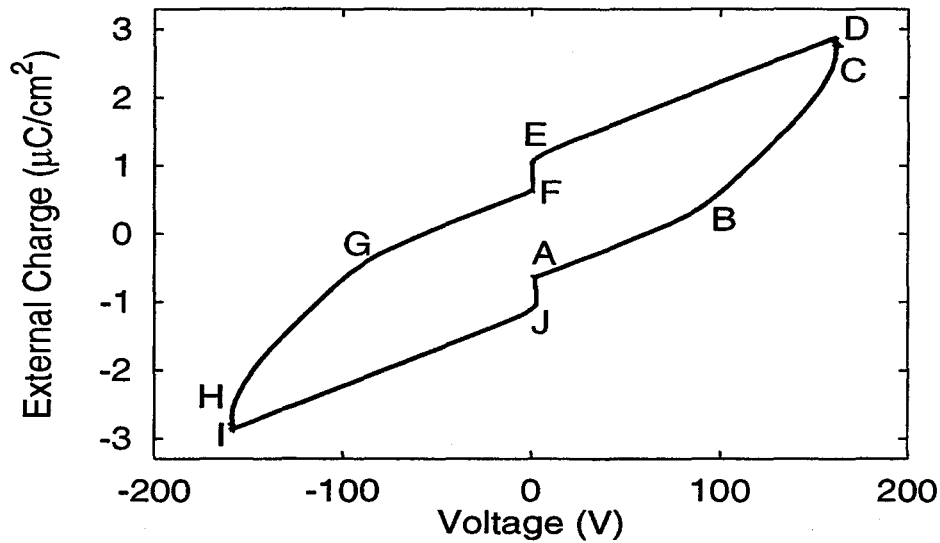


Figure 2.11: A typical experimental Q-V curve.

A number of the characteristics of the ACTFEL device under test can be observed from a Q-V curve. The letters on Figs. 2.2 and 2.11 correspond such that point A in Fig. 2.11 is the start of a positive voltage pulse. Point A is not located at the origin because of the residual field remaining in the phosphor region at the end of a voltage pulse. Under steady-state operation the amount of charge still present in the device at point A is called the polarization charge, Q_{pol} . As with many other characteristic values, polarization charge has two values, one each associated with a positive and negative voltage pulse. From points A to B, the applied voltage is ramping up and the device turn-on voltage is reached at point B. Above turn-on, charge is conducted across the phosphor region, shorting out c_p . The reduced total capacitance manifests itself in the change in slope between points B and C. At point C, the maximum voltage across the device is reached and at point D the voltage begins falling. The amount of charge that flows between points B and D is known as the conduction charge, Q_{cond} , which is the amount of charge which

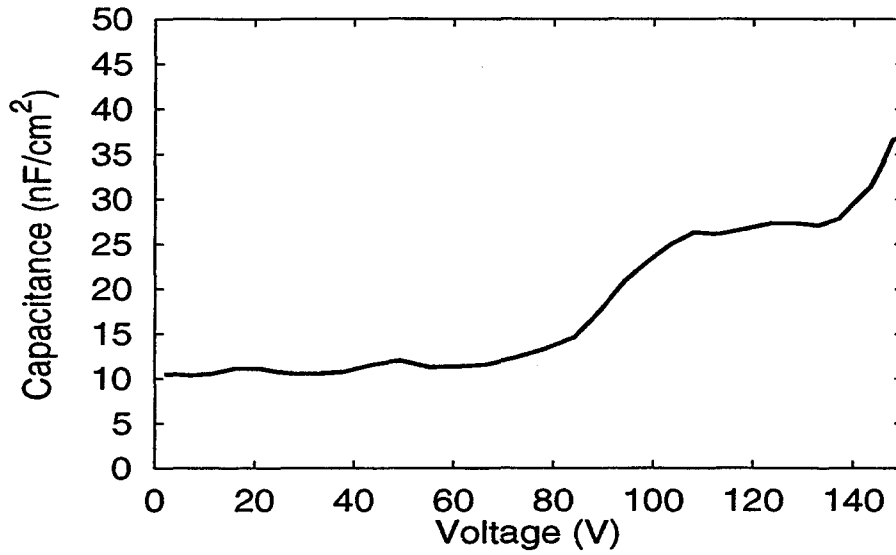


Figure 2.12: A typical experimental C-V curve for a ZnS:Mn device.

flows between the cathodic and anodic interfaces for one voltage pulse. At point E, the applied voltage reaches zero and between points E and F leakage charge, Q_{leak} , flows. The analysis for a negative applied voltage pulse, from points F to A, is similar so the details are omitted.

2.5.3 Capacitance - Voltage (C-V) Analysis

C-V curves show the dynamic capacitance of the ACTFEL device as a function of applied voltage. The easiest way to obtain a C-V curve is to differentiate Q-V curve data to obtain the total device capacitance,

$$c_t = \frac{dQ}{dV}. \quad (2.2)$$

Figure 2.12 shows a typical experimental C-V curve for a ZnS:Mn device. This curve clearly shows that c_t increases above turn-on, corresponding to the shorting of the phos-

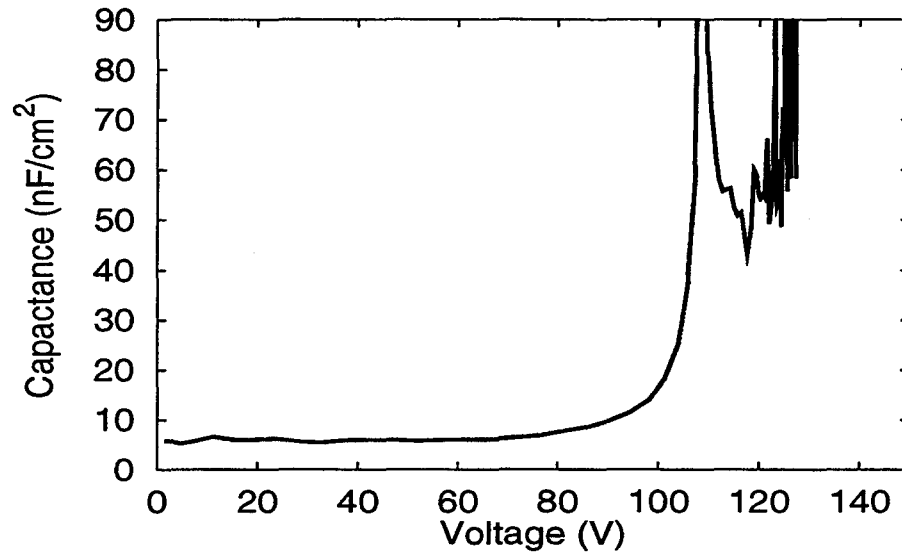


Figure 2.13: A typical experimental C-V curve for an SrS ACTFEL device.

phor capacitance. The fact that the transition between c_i and c_t in Fig. 2.12 is not instantaneous means that some electrons are being emitted from shallow interface states at a lower applied voltage than is required to emit a large number of electrons from deeper interface states.

Figure 2.13 shows an experimental C-V curve that is more typical of SrS ACTFEL of devices. Before reaching a value corresponding to c_i above threshold, the curve shown in Fig. 2.13 exhibits a great deal of capacitance-voltage overshoot. The cause of C-V overshoot is linked to dynamic space charge creation.

2.5.4 Internal Charge - Phosphor Field ($Q - F_p$) Analysis

Figure 2.14 shows a typical ZnS:Mn experimental $Q - F_p$ curve, which is a plot of internal charge in the phosphor region, $q_{int}(t)$, versus the average electric field in the phosphor region, $f_p(t)$. $q_{int}(t)$ and $f_p(t)$ are found from

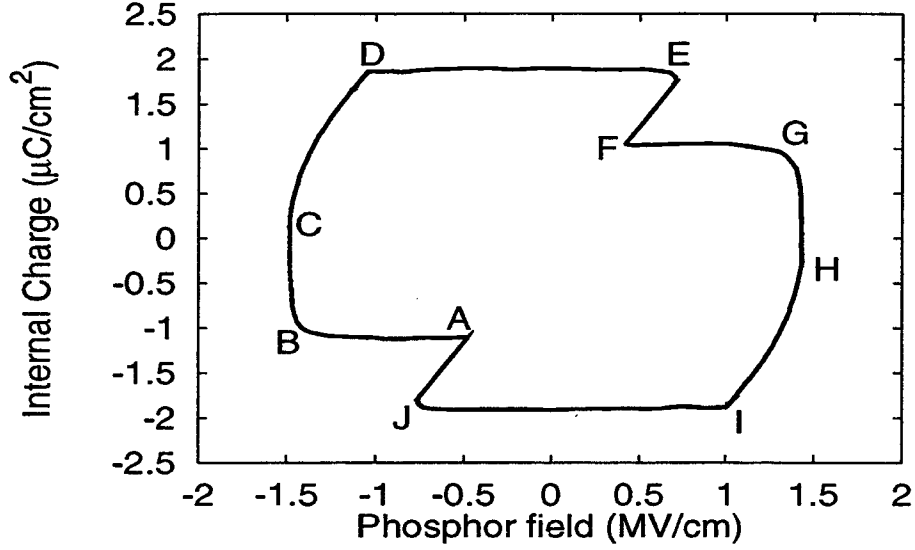


Figure 2.14: A typical experimental $Q - F_p$ curve.

$$q_{int}(t) = \frac{c_i + c_p}{c_i} q_{ext}(t) - c_p v_{el}(t) \text{ and} \quad (2.3)$$

$$f_p(t) = \frac{1}{d_p} \left[\frac{q_{ext}(t)}{c_i} - v_{el}(t) \right], \quad (2.4)$$

where d_p is the thickness of the phosphor region, $v_{el}(t)$ is the voltage across the ACTFEL device, and q_{ext} is the external charge across the ACTFEL device as determined in Eq. 3.6. It is important to note that a $Q - F_p$ curve displays entirely internal quantities which are solved for using external quantities.

The letters on Fig. 2.14 once again correspond to the letters of Fig. 2.2. Many of the same quantities that can be observed on Q-V curves, such as Q_{pol} and Q_{cond} , are also visible on $Q - F_p$ curves. $Q - F_p$ curves, however, reveal some details not apparent from Q-V curves. The charge that flows from points C to D, the relaxation charge (Q_{relax}), is more easily seen on a $Q - F_p$ than a Q-V curve. Q_{relax} corresponds to the amount of

charge that flows in the phosphor region while the applied voltage is at its maximum and the average phosphor field relaxes from its maximum value.

$Q - F_p$ curves generated using SrS ACTFEL devices usually show a large field overshoot between points B and C as well as between points G and H. The increased average field in these regions of operation corresponds to dynamic space charge creation. The increased cathode field caused by the presence of space charge gives rise to an increase in average phosphor field, f_p , hence the field overshoot.

3. DERIVATION OF DEVICE EQUATIONS FOR THE TWO-SHEET CHARGE MODEL

This chapter presents a derivation of the two-sheet charge model from device physics based equations. The two sheet charge model provides for dynamic space charge creation along two separate planes, or sheets, within the phosphor region of the ACTFEL device. This particular model also allows for the concomitant creation of space charge at one sheet and annihilation at the second sheet in the phosphor region. Simultaneous creation and annihilation of space charge is especially relevant for the simulation of SrS devices. The model presented herein provides for the creation of dynamic space charge by trap-to-band impact ionization. After the presentation of the two-sheet charge model, equations are developed which allow the ACTFEL device to be simulated with the external test circuit presented in Chapter 2. The simulation results presented in Chapter 4 as well as the work of others [4, 14] has shown that realistic simulation of Q-F_p and C-V overshoot is not possible without considering the effects of the external circuit on the ACTFEL device. Finally, the issues of feedback effects and model stability are addressed.

3.1 The Two-Sheet Charge Model

This section presents the quasi-statics and dynamics of the two-sheet charge model. The derivation presented herein is very similar to Keir's derivation for the single sheet charge model. [3]

3.1.1 Basic Operation of the Modeling Program

Before deriving the ACTFEL device equations that lead to the computer simulation model, it is useful to discuss the methodology of the simulation program used to generate the data presented in this thesis. The simulation program, written in C, operates by taking small timesteps and solving for the value of electric field in various device regions

at the end of each timestep. From the movement of charge within the phosphor region, the time derivatives of electric field are calculated. A differential equation solver utilizing the Runge-Kutta-Fehlberg algorithm is employed to solve for the electric field values at the end of each timestep based on these electric field time derivatives. From the electric field values, as well as from various device constants such as insulator capacitance and phosphor region thickness, various simulated electrical characterization curves can be generated. The goal, then, of the two-sheet charge model derivation is to obtain equations for electric field and electric field time derivatives in terms of quantities which can be easily evaluated.

3.1.2 The Quasi-Static Two-Sheet Charge Model

The two discrete sheets of space charge within the phosphor region in the two-sheet charge model give rise to three different electric field regions in the phosphor, as is shown in Fig. 3.1. The parameter names shown in Fig. 3.1 are used throughout the remainder of this thesis. v_{el} is the voltage applied to the ACTFEL device, the i and p subscripts refer to the insulator and phosphor layers, while d , f , and q denote distance, electric field, and charge density, respectively. The subscript sc refers to one of the sheets of space charge.

The goal of the quasi-static description of the ACTFEL device is to develop expressions for the electric fields in each of the phosphor regions in terms of parameters that can be evaluated. In this case these parameters are charge density at each of the device interfaces and the external charge density of the entire device. The first step in the development of the quasi-static model is to apply Kirchhoff's voltage law to the device shown in Fig 3.1 to obtain

$$d_{i1}f_{i1}(t) + d_{s1}f_{p1}(t) + (d_{s2} - d_{s1})f_{p2}(t) + (d_p - d_{s2})f_{p3}(t) + d_{i2}f_{i2}(t) = -v_{el}(t). \quad (3.1)$$

The sign convention for electric field in Eq. 3.1 is opposite to the usual convention, such that the field points in the direction that an electron will drift. This is done to remain consistent with the work of Bringuier [15], Keir [3] and others in order to obtain similar electrical characterization curves. The consequence of this new sign convention is that a

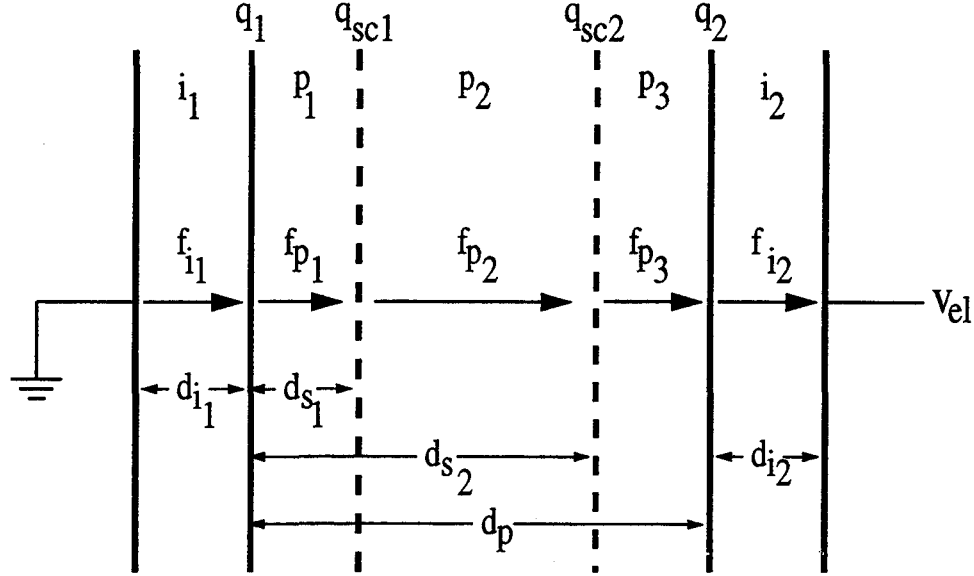


Figure 3.1: The two-sheet charge model of the ACTFEL device.

positive applied voltage pulse across the ACTFEL device will yield negative electric fields in the phosphor region. The next step towards solving the ACTFEL device electrostatics problem is to find relations for the charge density at each device interface. Using Gauss' Law the equations

$$c_{i1}d_{i1}f_{i1}(t) - c_p d_p f_{p1}(t) = -q_1(t), \quad (3.2)$$

$$c_p d_p [f_{p1}(t) - f_{p2}(t)] = -q_{sc1}(t), \quad (3.3)$$

$$c_p d_p [f_{p2}(t) - f_{p3}(t)] = -q_{sc2}(t), \text{ and} \quad (3.4)$$

$$c_p d_p f_{p3}(t) - c_{i2}d_{i2}f_{i2}(t) = -q_2(t) \quad (3.5)$$

emerge where the c terms refer to the capacitance of each device region. In addition to the above four relations for charge density, one other charge density equation is needed to solve the electrostatic problem of the ACTFEL device. The ACTFEL device can be thought of as one composite capacitor consisting of the series combination of the two insulator capacitances and the phosphor region capacitance. The charge on this composite capacitor

is called the external charge, q_e . This external charge can be expressed many ways since the charge on every capacitor is the same in equilibrium. One possible expression is

$$c_{i1}d_{i1}f_{i1}(t) = c_{i2}d_{i2}f_{i2}(t) = -q_e(t). \quad (3.6)$$

Since charge balance must be maintained within the device, the relation

$$q_1(t) + q_2(t) + q_{sc1}(t) + q_{sc2}(t) = 0 \quad (3.7)$$

is also obtained. The equations developed thus far completely describe the internal fields and charge densities within the ACTFEL device. These equations can now be manipulated to solve for the phosphor fields in terms of charge density.

Solving Eqs. 3.2-3.5 for phosphor electric field yields the relations

$$f_{p1}(t) = \frac{q_1(t) + c_{i1}d_{i1}f_{i1}(t)}{c_p d_p}, \quad (3.8)$$

$$f_{p2}(t) = \frac{q_{sc1}(t)}{c_p d_p} + f_{p1}(t), \text{ and} \quad (3.9)$$

$$f_{p3}(t) = \frac{-q_2(t) + c_{i2}d_{i2}f_{i2}(t)}{c_p d_p}. \quad (3.10)$$

Substituting Eq. 3.8 into Eq. 3.9 and then substituting Eq. 3.6 into Eqs. 3.8-3.10 gives the desired expressions for the three phosphor fields

$$f_{p1}(t) = \frac{1}{c_p d_p} [q_1(t) - q_e(t)], \quad (3.11)$$

$$f_{p2}(t) = \frac{1}{c_p d_p} [q_1(t) + q_{sc1}(t) - q_e(t)], \text{ and} \quad (3.12)$$

$$f_{p3}(t) = \frac{1}{c_p d_p} [-q_2(t) - q_e(t)]. \quad (3.13)$$

Now that these quasi-static equations for phosphor field have been derived, the model can easily be extended to the dynamic case.

3.1.3 The Dynamic Two-Sheet Charge Model

The expressions found for phosphor field in Eqs. 3.11-3.13 are easily extended to form the basis of the dynamic model by taking the partial derivative of these equations with respect to time. This differentiation results in the first order differential equations

$$\frac{\partial f_{p1}}{\partial t} = \frac{1}{c_p d_p} \left(\frac{\partial q_1}{\partial t} - \frac{\partial q_e}{\partial t} \right), \quad (3.14)$$

$$\frac{\partial f_{p2}}{\partial t} = \frac{1}{c_p d_p} \left(\frac{\partial q_1}{\partial t} + \frac{\partial q_{sc1}}{\partial t} - \frac{\partial q_e}{\partial t} \right), \text{ and} \quad (3.15)$$

$$\frac{\partial f_{p3}}{\partial t} = \frac{-1}{c_p d_p} \left(\frac{\partial q_2}{\partial t} + \frac{\partial q_e}{\partial t} \right). \quad (3.16)$$

The partial derivatives of charge density in Eqs. 3.14-3.16 above represent the ACTFEL device current densities. In order to numerically evaluate the expressions for the time derivatives of electric field, Eqs. 3.14-3.16 must be expressed in terms of internal current densities only. This necessitates finding a relation for $\frac{\partial q_e}{\partial t}$ in terms the internal current densities. Substituting Eq. 3.6 into the Kirchhoff's voltage law relation (Eq. 3.1) and solving for q_e yields

$$q_e(t) = \frac{c_i}{2} [d_{s1} f_{p1}(t) + (d_{s2} - d_{s1}) f_{p2}(t) + (d_p - d_{s2}) f_{p3}(t) + v_{el}(t)]. \quad (3.17)$$

By substituting charge density expressions for electric field into Eq. 3.17, performing a few algebraic manipulations and then differentiating with respect to time, the expression

$$\frac{\partial q_e}{\partial t} = \frac{c_i}{c_i + c_p} \left[\frac{\partial q_1}{\partial t} \frac{d_{s2}}{d_p} + \frac{\partial q_{sc1}}{\partial t} \frac{(d_{s2} - d_{s1})}{d_p} + \frac{\partial q_2}{\partial t} \frac{(d_p - d_{s2})}{d_p} + c_p \frac{\partial v_{el}}{\partial t} \right] \quad (3.18)$$

is obtained. Note that several other equivalent solutions for $\frac{\partial q_e}{\partial t}$ are possible. Now acceptable equations for the electric field time derivatives can be found by substituting Eq. 3.18 back into Eqs. 3.14-3.16. The external voltage slew rate across the ACTFEL device is generally a known quantity. In order to numerically evaluate the partial electric field derivatives, it necessary to develop expressions for the internal charge density terms $\frac{\partial q_1}{\partial t}$, $\frac{\partial q_2}{\partial t}$, $\frac{\partial q_{sc1}}{\partial t}$, and $\frac{\partial q_{sc2}}{\partial t}$. Before presenting equations for the current density terms, it is useful to examine current flow within the ACTFEL device more closely.

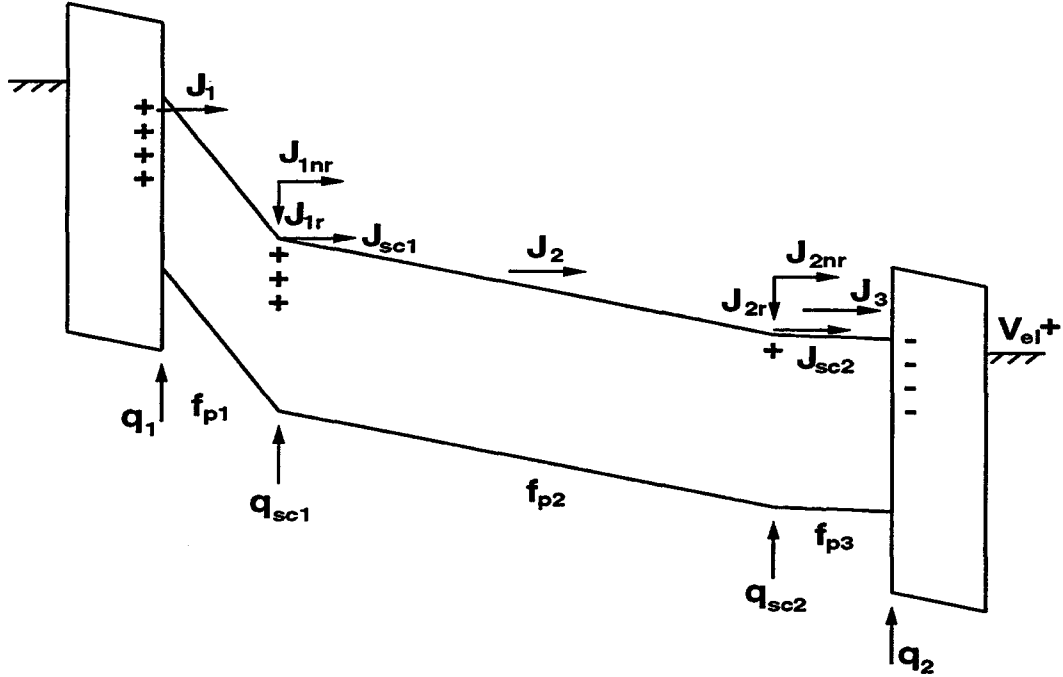


Figure 3.2: Energy band diagram showing current flow in the two-sheet charge model.

The version of the two-sheet charge model used for ACTFEL device simulation in this thesis allows for charge to be either emitted or captured by any of the four device interfaces which include the two phosphor-insulator interfaces and the two sheets of space charge. In fact, electron emission and capture in this model are allowed only at these four interfaces. Figure 3.2 shows an energy band diagram depicting charge flow in the two-sheet charge model for an ACTFEL device with a positive voltage pulse applied to the aluminum electrode. Note that the arrows in this figure represent the direction of electron movement, not the direction of current. As the externally applied voltage pulse is ramped up, electrons trapped in interface states at the phosphor-insulator interface on the ITO side of the device begin to tunnel into the phosphor region. This tunneling gives rise to the current J_1 shown in Fig. 3.2 and creates positive charge at the cathodic phosphor-insulator interface.

As the electrons emitted from the cathodic interface travel along the length of the phosphor, they may be captured by positive space charge in the phosphor region and recombine. Current lost due to this type of recombination is denoted with the subscript r in Fig. 3.2 and is shown going into the sheets of space charge. In addition to capturing electrons, the space charge sheets may also emit electrons and add to the device current density (the form of the equations for the trap-to-band impact ionization process assumed for space charge creation is presented in Section 3.3.1). Electron emission from one of the space charge sheets leads to the creation of positive space charge, while electron capture at a space charge sheet eliminates this positive space charge. The different amount of positive space charge at the two space charge sheets is what causes the electric field to be different in each of the three phosphor regions. Finally, the net number of electrons which flow across the entire phosphor region are captured by the anodic interface and give rise to a net negative charge at this insulator-phosphor interface.

Returning to the development of expressions for the $\frac{\partial q}{\partial t}$ terms, it is found that

$$\frac{\partial q_1}{\partial t} = J_1 \quad (3.19)$$

for the case of a positive applied voltage pulse, as shown Fig. 3.2. The current density into the sheet of space charge q_{sc1} is simply

$$J_{1r} = J_1 sccf_1 \quad (3.20)$$

where $sccf$ is a parameter known as the space charge capture factor. This parameter is a field-dependent number between zero and one that corresponds to the probability that charge emitted from the cathodic phosphor-insulator interface is captured at a given space charge sheet. The number of electrons emitted from the cathodic interface which do not recombine at q_{sc1} , J_{1nr} , is equal simply to the total number of electrons emitted minus the electrons which recombine at the first space charge sheet,

$$J_{1nr} = J_1(1 - sccf_1). \quad (3.21)$$

In the simulation model for ACTFEL devices presented in this thesis, the method for space charge creation is assumed to be trap-to-band impact ionization. This means that the current due to electron emission from q_{sc1} is based on the flux of electrons between the cathodic insulator-phosphor interface and q_{sc1} . The additional electrons generated from impact ionization are typically described by a multiplication factor per unit distance, mf , so

$$J_{sc1} = (mf_1 - 1)J_{1nr} = (mf_1 - 1)(1 - sccf_1)J_1 \quad (3.22)$$

is the equation for current from q_{sc1} . Before moving on, several things should be noted about Eq. 3.22. First, since the magnitude of mf_1 is based on the distance between the cathodic interface and q_{sc1} , as well as the electric field f_{p1} , it may seem strange to apply an equation of this sort to a discrete model. Despite the fact that additional carriers are being generated continuously across the phosphor layer in the actual ACTFEL device, the creation of space charge and carrier emission is allowed to occur only at the interfaces in the model presented in this thesis. This means that all the electrons gained from impact ionization between the cathodic interface and q_{sc1} are added to the total current only at q_{sc1} . This is a good approximation of the actual device if q_{sc1} is located very close to the cathodic interface (d_{s1} is very small).

Secondly, the multiplication factor is applied only to electrons which are not captured at q_{sc1} , and not to the total electron current from the cathodic interface, J_1 . This means that an electron cannot be multiplied in the field region f_{p1} if it is ultimately captured at q_{sc1} . This may seem like a poor assumption, but the implications of using an equation like

$$J_{sc1} = (mf_1 - 1)J_1 \quad (3.23)$$

for the current from q_{sc1} are worse. If the multiplication factor is applied to the total current from the cathodic interface, J_1 , this is equivalent to creating an amount of positive space charge located somewhere between the cathodic interface and q_{sc1} equal in magnitude to $J_1 sccf_1 dt$. Since electrons can only recombine at the four interfaces in the

model presented herein, the use of Eq. 3.23 leads to the creation of pseudo-dynamic space charge that cannot be annihilated because it is not located at an interface. The net result is model instability. In any event, since electron multiplication becomes more likely at high electric fields and electron capture becomes more likely at low fields, capture and multiplication mechanisms really are not operative at a single interface simultaneously. Therefore, using Eq. 3.22 for the current from q_{sc1} results in model stability and does not represent much of a compromise in terms of the physics of the actual device.

Finally, it may not be readily apparent why the factor $(mf_1 - 1)$ is used in Eq. 3.22 instead of simply mf_1 . The origin of the $(mf_1 - 1)$ term is as follows. The total current due to impact ionization at a given distance along a semiconductor device is typically expressed as an initial current multiplied by a position-dependent multiplication factor; this general situation is also the case here. The total current between q_{sc1} and q_{sc2} is

$$J_2 = (mf_1)J_{1nr} \quad (3.24)$$

as shown in Fig. 3.2. Current flow in the two-sheet charge model can only originate at the phosphor-insulator interfaces and at the space charge layers. For the case shown in Fig. 3.2, J_2 is written in terms of current originating from q_1 and q_{sc1} to yield

$$J_2 = J_{sc1} + J_{1nr}. \quad (3.25)$$

Substituting Eq. 3.25 into Eq. 3.24 and subtracting J_{1nr} from both sides of the equation gives

$$J_{sc1} = (mf_1)J_{1nr} - J_{1nr}, \quad (3.26)$$

which shows the origin of the $(mf_1 - 1)$ term in Eq. 3.22.

Analysis of the currents into and out of the second phosphor space charge sheet, q_{sc2} , leads to the set of equations

$$J_{2r} = J_2 scf_2, \quad (3.27)$$

$$J_{2nr} = J_2(1 - sccf_2), \text{ and} \quad (3.28)$$

$$J_{sc2} = (mf_2 - 1)J_{2nr}, \quad (3.29)$$

which are similar to Eqs. 3.20, 3.21 and 3.22 for q_{sc1} . The final current density term to consider is the total current into the anodic interface,

$$J_3 = J_{sc2} + J_{2nr}. \quad (3.30)$$

Now that solutions have been obtained for the various current density terms, it is possible to solve for the remaining $\frac{\partial q}{\partial t}$ terms. By summing all the currents associated with q_{sc1} , with q_{sc2} , and with the anodic insulator-phosphor interface, it is found that

$$\frac{\partial q_{sc1}}{\partial t} = J_{sc1} - J_{1r}, \quad (3.31)$$

$$\frac{\partial q_{sc2}}{\partial t} = J_{sc2} - J_{2r}, \text{ and} \quad (3.32)$$

$$\frac{\partial q_2}{\partial t} = J_3 \quad (3.33)$$

which completes the dynamic two-sheet charge model.

An alternate way to consider the $\frac{\partial q}{\partial t}$ terms is as the sum of generation and recombination terms at each interface leading back to emission from the cathodic insulator-phosphor interface. For example, manipulation of Eqs. 3.20 - 3.22 and 3.24 - 3.26 yields the expression

$$\frac{\partial q_{sc1}}{\partial t} = J_1(1 - sccf_1)(mf_1 - 1) - J_1 sccf_1 \quad (3.34)$$

for the first space charge sheet. The first term on the right hand side of Eq. 3.34 is the generation term while the second term is the recombination term. Similarly, the expression

$$\frac{\partial q_{sc2}}{\partial t} = J_1(1 - sccf_1)(mf_1 - 1)(1 - sccf_2)(mf_2 - 1) - J_1(1 - sccf_1)(mf_1 - 1)sccf_2 \quad (3.35)$$

is obtained for generation and recombination at the second space charge sheet. From inspection of Eqs. 3.34 and 3.35, the logical extension of the model to n sheets of charge becomes apparent:

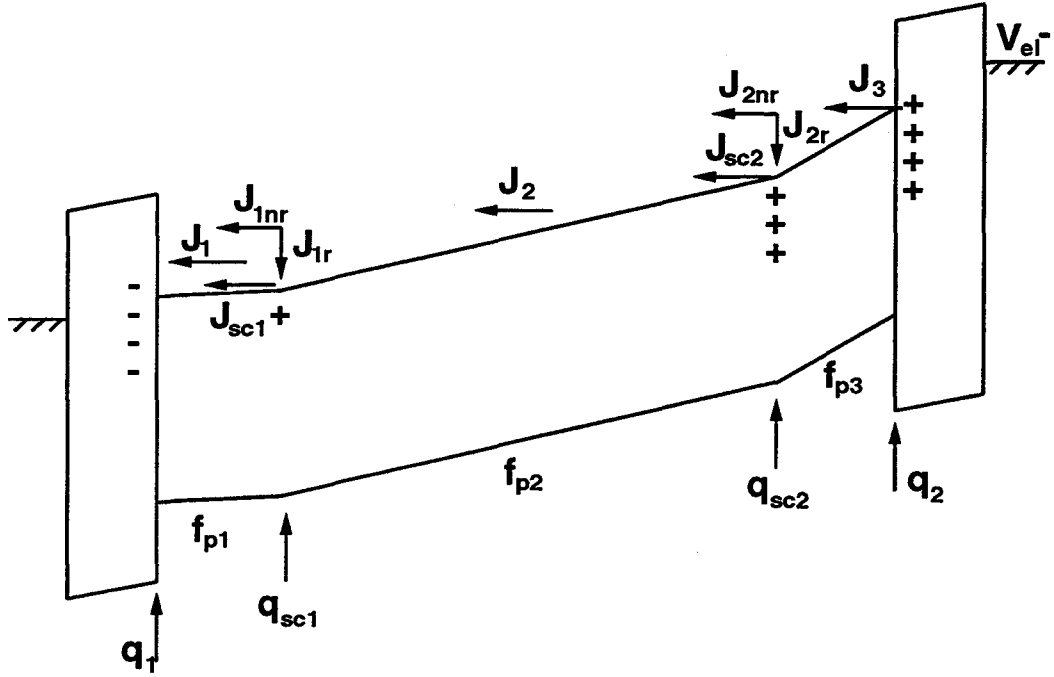


Figure 3.3: Energy band diagram showing current flow for a negative applied voltage.

$$\begin{aligned} \frac{\partial q_{scn}}{\partial t} = & J_1(1 - sccf_1)(mf_1 - 1)\dots(1 - sccf_n)(mf_n - 1) - \dots \\ & - J_1(1 - sccf_1)(mf_1 - 1)\dots(1 - sccf_{n-1})(mf_{n-1} - 1)sccf_n. \end{aligned} \quad (3.36)$$

It should be noted that Eqs. 3.19 and 3.31-3.33 hold just as well for a negative applied voltage pulse or during the interval between voltage pulses. The difference is that in these situations the opposite interface, as shown in Fig. 3.2, acts as the cathodic interface; additionally, under certain phosphor field conditions both insulator-phosphor interfaces may act as electron emitting interfaces. If the applied voltage pulse is negative, as shown in Fig. 3.3, electrons are emitted from insulator-phosphor interface q_2 and received by q_1 . Additionally, electrons generated by impact ionization multiplication travel toward q_1 for a negative applied voltage pulse. The analysis of the internal current density terms for this case proceeds exactly the same as for the analysis for a positive applied

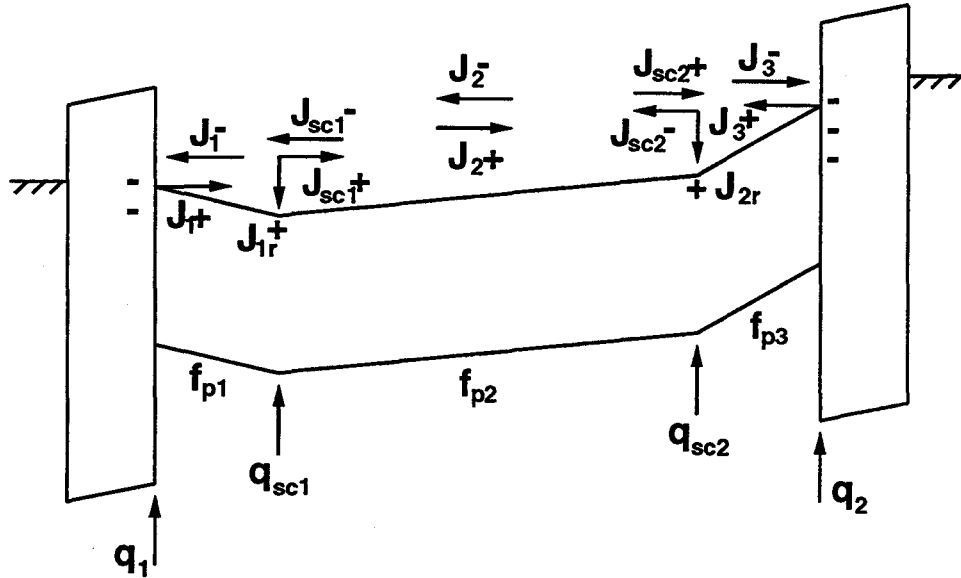


Figure 3.4: Energy band diagram showing current flow during unusual field conditions in which both phosphor-insulator interfaces emit electrons.

voltage pulse, so the details are omitted. The main difference is that the signs of the current density terms J_1 , J_2 , and J_3 are reversed for a negative voltage pulse.

A third possible internal field condition is shown in Fig. 3.4. During the interval between externally applied voltage pulses, or during the falling portion of an applied voltage pulse, internal phosphor fields such as those shown in Fig. 3.4 are possible. In this case, electrons are emitted from both phosphor-insulator interfaces. This means that q_{sc1} and q_{sc2} may capture electrons traveling in either direction across the phosphor and that both space charge layers may emit electrons which then travel towards either q_1 or q_2 . This situation seems complicated, but it can be simulated quite easily. By simply superimposing the situation of negative and positive applied pulses on top of each other, the current density terms J_1 , J_2 , and J_3 become simply the addition of their magnitudes for both directions across the phosphor region, as shown in Fig. 3.4. In this figure, the terms with a positive suffix refer to the current directions normally expected for a positive

applied voltage, while a negative suffix indicates the usual current flow for a negative pulse.

3.2 Electron Emission from Insulator-Phosphor Interfaces

The dynamic two-sheet charge model has now been developed to the point where expressions for the internal current density terms need to be obtained. In order to accomplish this, it is necessary to obtain equations for the electron emission rates from the insulator-phosphor interfaces in terms of the phosphor electric field. In the model presented herein, all the electrons at the insulator-phosphor interfaces are assumed to be trapped in a discrete trap below the conduction band. When a large enough electric field exists in the phosphor region adjacent to the cathodic phosphor-insulator interface, a significant number of electrons may be emitted into the phosphor region from the discrete coulombic well at the interface. The derivation of the interface emission equations closely follows the derivation presented by Keir. [3]

In this thesis the contributions of three different mechanisms are considered when calculating the the total electron emission rates from the interfaces. These mechanisms, as shown in Fig. 3.5, are thermal emission ($e_n^{thermal}$), phonon-assisted tunneling (e_n^{PAT}), and pure tunneling (e_n^{PT}). In most cases considered in this thesis, pure tunneling dominates the total interface emission rate. Especially at room temperature, thermal emission is typically several orders of magnitude smaller than the other mechanisms. For large interface trap depths (E_{it} in Fig. 3.5) phonon-assisted tunneling may become as important as pure tunneling. In the case of SrS devices, as considered in this thesis, E_{it} is typically around 1 eV and the emission rate due to phonon-assisted tunneling is orders of magnitude smaller than electron emission from pure tunneling. For very low phosphor fields, thermal emission may in fact dominate interface emission. The total emission rate at low phosphor fields is negligible, however, compared to the total emission rate at device turn-on. Despite the fact that pure tunneling often dominates, for completeness all three emission mechanisms are included in the total emission rate as calculated in this thesis.

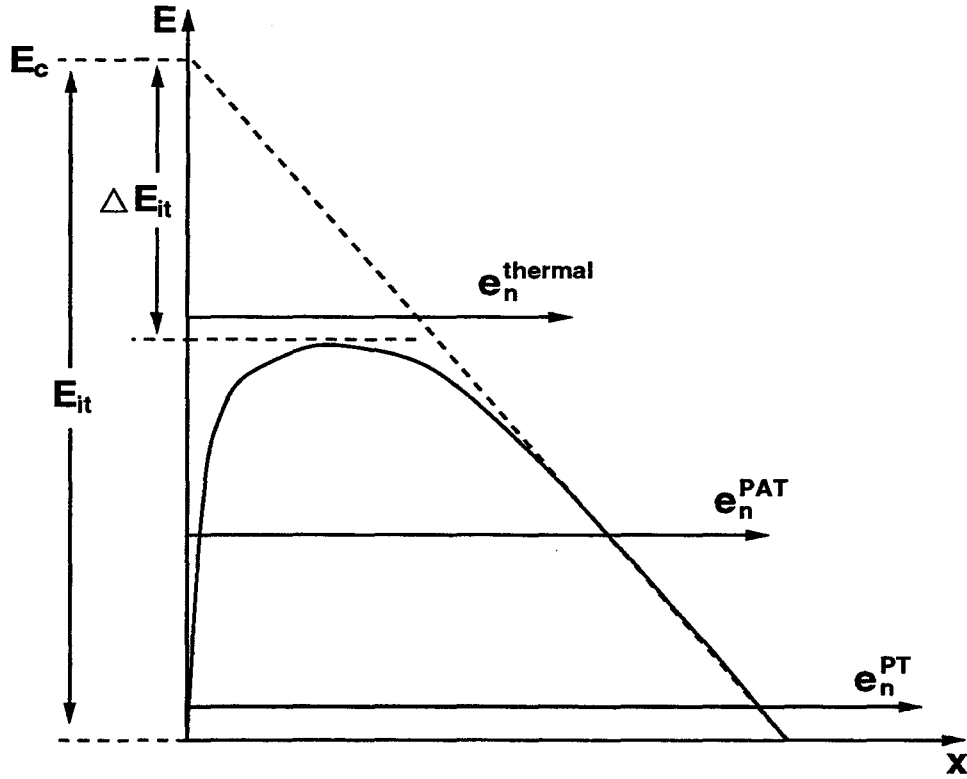


Figure 3.5: The three field emission mechanisms from the phosphor-insulator interfaces.

The total emission rate from a given phosphor-insulator interface is found simply from the sum of the three different emission rates

$$e_n = e_n^{PT} + e_n^{PAT} + e_n^{thermal}. \quad (3.37)$$

Now, expressions for each of the separate emission mechanisms must be found. These expressions have been reported in the literature [16, 17] and are repeated from Keir. [3] The expression for electron emission rate due to pure tunneling from a discrete Coulombic well as a function of electric field is

$$e_n^{PT}(f_p) = \frac{q f_p}{4(2m^* E_{it})^{1/2}} \exp \left[\left(-\frac{4}{3} \frac{(2m^*)^{1/2} E_{it}^{3/2}}{q \hbar f_p} \right) \left(1 - \left(\frac{\Delta E_{it}}{E_{it}} \right)^{5/3} \right) \right] \quad (3.38)$$

where f_p is the phosphor field in the region immediately adjacent to the phosphor-insulator

interface in question - f_{p1} for interface q_1 and f_{p3} for q_2 . ΔE_{it} is defined as:

$$\Delta E_{it} = q \left(\frac{q f_p}{\pi \epsilon_p} \right)^{1/2}. \quad (3.39)$$

The expression for thermal emission from a discrete trap is

$$e_n^{thermal}(f_p) = \sigma v_{th} N_c \exp \left(-\frac{E_{it} - \Delta E_{it}}{kT} \right) \quad (3.40)$$

where σ is the capture cross section for thermal emission and v_{th} is the thermal velocity. By substituting Eq. 3.39 into Eq. 3.40 it is clear that thermal emission is only a slightly increasing function of field. The expression for phonon-assisted tunneling is more complex than the expressions for the other mechanisms:

$$e_n^{PAT} = e_n^{thermal} \int_{\Delta E_{it}/kT}^{E_{it}/kT} \exp \left[z - z^{3/2} \left(\frac{4}{3} \frac{(2m^*)^{1/2} (kT)^{3/2}}{q \hbar f_p} \right) \right] \times \dots \times \left(1 - \left(\frac{\Delta E_{it}}{z k T} \right)^{5/3} \right) dz. \quad (3.41)$$

Now that each of the terms in Eq. 3.37 has been defined, the total emission rate from the insulator-phosphor interfaces can be calculated. This total emission rate can be used to solve for the interface current density terms $\frac{\partial q_1}{\partial t}$ and $\frac{\partial q_2}{\partial t}$. The current density out of a given interface at time t is

$$\frac{\partial q_x}{\partial t} = -q e_n n_x(t) \quad (3.42)$$

where $n_x(t)$ is the number of electrons present at interface x at time t . In order to calculate the number of electrons present at an interface at a given time, it is necessary to know the trap occupancy for zero applied field, $N_o f_o$. Using this no-field occupancy, the expression

$$q_x(t) = q [N_o f_o - n_x(t)] \quad (3.43)$$

is obtained, relating occupancy to the amount of charge at the interface. Eq. 3.43 can easily be solved for $n_x(t)$ and the result substituted into Eq. 3.42. Additionally, $q_x(t)$ can

be obtained from Eqs. 3.2 and 3.5 in terms of the phosphor fields. Finally the equation for the interface current density terms,

$$\frac{\partial q_x}{\partial t} = -e_n[qN_o f_o - q_x(t)] \quad (3.44)$$

emerges. Substituting the three emission mechanisms from Eq. 3.37 into Eq. 3.44 yields the complete expression for the interface current density terms.

3.3 Electron Multiplication

As energetic electrons transit the phosphor layer, they may cause an increase in the total number of carriers in the phosphor by participating in a trap-to-band or band-to-band impact ionization event. This section presents a derivation of model parameters for both types of impact ionization.

3.3.1 Trap-to-Band Impact Ionization

Now that expressions for $\frac{\partial q_1}{\partial t}$ and $\frac{\partial q_2}{\partial t}$ have been found, in order to complete the model it is necessary to find expressions for $\frac{\partial q_{sc1}}{\partial t}$ and $\frac{\partial q_{sc2}}{\partial t}$. As stated previously, the sole mechanism for the creation of space charge in the model presented in this thesis is trap-to-band impact ionization. Any emission of electrons from a space charge layer results in the creation of positive space charge. Therefore the phosphor layer current density terms, $\frac{\partial q_{sc1}}{\partial t}$ and $\frac{\partial q_{sc2}}{\partial t}$, associated with the space charge sheets can be evaluated by considering only trap-to-band impact ionization.

A trap-to-band impact ionization event occurs when an energetic conduction band electron ionizes a trap in the phosphor layer, as shown Fig. 3.6. As a result of this impact ionization event, a previously trapped electron is injected into the conduction band and positive space charge is created in the phosphor layer. Since space charge creation is allowed only at the two sheets of space charge in this model, trap-to-band impact ionization can only occur at the two space charge sheets.

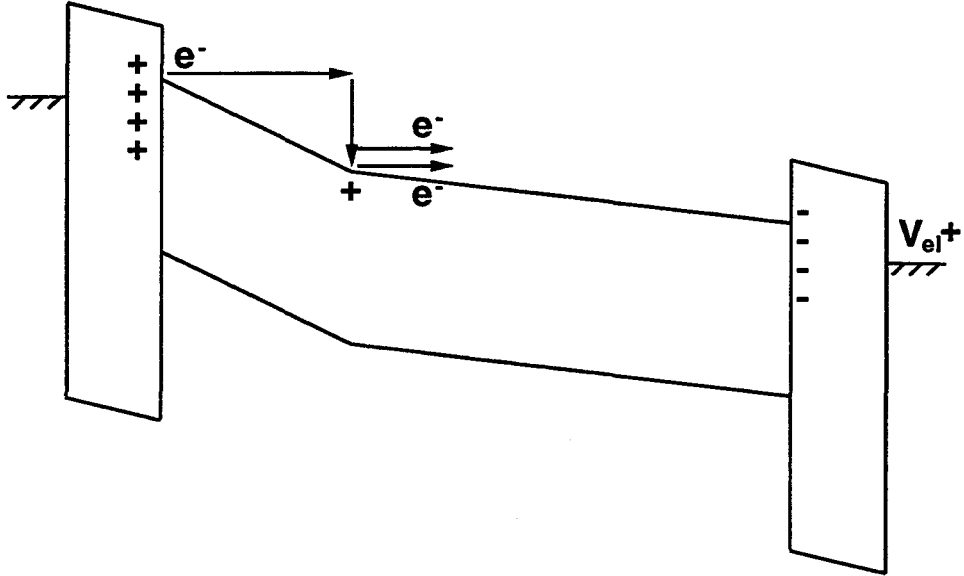


Figure 3.6: A trap-to-band impact ionization event.

The derivation of equations for carrier multiplication by trap-to-band impact ionization presented herein is similar to that presented by Keir. [3] The derivation presented is for a positive voltage pulse only, although the derivation for a negative pulse follows similarly. Capture cross-sections for impact ionization in a semiconductor have been shown to fit [18]

$$\sigma(f_p, N_t) = B(f_p, N_t) \exp \left[- \left(\frac{f_o}{f_p} \right)^n \right] \quad n = 1, 2 \quad (3.45)$$

where N_t is trap concentration in the phosphor. Note that in the two-sheet charge model all of the traps in the phosphor layer are located at one of the two-sheets of space charge.

The form of $B(f_p, N_t)$ used is

$$B(f_p, N_t) = \frac{q f_p}{N_t E_{ion}}. \quad (3.46)$$

Expressing $B(f_p, N_t)$ in this way maintains consistency with Bringuier's treatment of band-to-band impact ionization for phosphor materials. [19] The ionization function for trap-

to-band impact ionization, $\alpha(f_p, n_t, N_t)$, is [18, 20]

$$\alpha(f_p, n_t, N_t) = \left(1 - \frac{n_t}{N_t}\right) \sigma(f_p, N_t) \quad (3.47)$$

where n_t is the total number of empty traps in the phosphor,

$$n_t = N_t - N_{filled}. \quad (3.48)$$

The ionization function can now be used to write a current continuity equation. If generation and recombination in the phosphor region are neglected,

$$\frac{\partial J}{\partial x} = \alpha(f_p)J. \quad (3.49)$$

Solving this first order differential equation gives an expression for current as a function of time and position in the phosphor layer:

$$J(x, t) = J(0, t) \exp[\alpha(f_p)x]. \quad (3.50)$$

Since the phosphor electric fields f_{p1} , f_{p2} , and f_{p3} are in general not equal, the value of α , and hence the current continuity equations in each of the three phosphor regions, will be different. In the region closest to the cathodic interface,

$$J(x, t) = J(0, t) \exp[\alpha(f_{p1})x] \quad 0 \leq x \leq d_{s1} \quad (3.51)$$

where $J(0, t)$ refers to the electrons emitted from the cathodic insulator-phosphor interface, simply J_1 of Fig. 3.2. In the middle phosphor region

$$J(x, t) = J(d_{s1}, t) \exp[\alpha(f_{p2})(x - d_{s1})] \quad d_{s1} \leq x \leq d_{s2}. \quad (3.52)$$

In this case $J(d_{s1}, t)$ is the net current after the first space charge layer. Again, using terms from Fig. 3.2,

$$J(d_{s1}, t) = J_{1nr} + J_{sc1} = J_2. \quad (3.53)$$

In the final phosphor region,

$$J(x, t) = J(d_{s2}, t) \exp[\alpha(f_{p3})(x - d_{s2})] \quad d_{s2} \leq x \leq d_p \quad (3.54)$$

where $J(d_{s2})$ is equal to J_3 of Fig. 3.2. To maintain current conservation in the phosphor, Eq. 3.51 and Eq. 3.52 must be equated at d_{s1} , and Eqs. 3.52 and 3.54 must be equated at d_{s2} . Performing these manipulations, the relations

$$J(d_{s1}, t) = J(0, t) \exp[\alpha(f_{p1})d_{s1}] \text{ and} \quad (3.55)$$

$$J(d_{s2}, t) = J(d_{s1}, t) \exp[\alpha(f_{p2})(d_{s2} - d_{s1})] \quad (3.56)$$

are obtained. From charge conservation

$$\frac{\partial q_{sc1}}{\partial t} = J_{sc1} - J_{1r} \text{ and} \quad (3.57)$$

$$\frac{\partial q_{sc2}}{\partial t} = J_{sc2} - J_{2r}. \quad (3.58)$$

Substituting Eq. 3.53 into Eq. 3.57 and performing a similar manipulation of Eq. 3.58 it is possible to write the equations

$$\frac{\partial q_{sc1}}{\partial t} = J(d_{s1}, t) - J_{1nr} - J_{1r} \text{ and} \quad (3.59)$$

$$\frac{\partial q_{sc2}}{\partial t} = J(d_{s2}, t) - J_{2nr} - J_{2r}. \quad (3.60)$$

By substituting Eqs. 3.55 and 3.56 into Eqs. 3.59 and 3.60, respectively, the equations

$$\frac{\partial q_{sc1}}{\partial t} = J_1(\exp[\alpha(f_{p1})d_{s1}] - 1) \text{ and} \quad (3.61)$$

$$\frac{\partial q_{sc2}}{\partial t} = J_2(\exp[\alpha(f_{p2})(d_{s2} - d_{s1})] - 1) \quad (3.62)$$

for the space charge layer current densities are finally obtained. An observant reader will note that carrier multiplication in the region between q_{sc2} and the anodic interface has not been included yet. To include this effect, slight modifications to Eqs. 3.61 and 3.62 are necessary. In reality, carrier multiplication occurs continuously across the phosphor region, while in the discrete two-sheet charge model additional carriers can only be added at the two space charge sheets. In order to limit the effects of this non-ideality of the model, the additional electrons generated from trap-to-band impact ionization are treated

in the model as follows: All of the electrons created in field region f_{p1} and half of the electrons created in f_{p2} are added at q_{sc1} ; the other half of the electrons created in f_{p2} and all the electrons created in f_{p3} are added at q_{sc2} . This method of handling the additional electrons leads to the following modifications to Eqs. 3.61 and 3.62:

$$\frac{\partial q_{sc1}}{\partial t} = J_1 \left(\exp \left[\alpha(f_{p1})d_{s1} + \frac{\alpha(f_{p2})(d_{s2} - d_{s1})}{2} \right] - 1 \right) \text{ and} \quad (3.63)$$

$$\frac{\partial q_{sc2}}{\partial t} = J_2 \left(\exp \left[\frac{\alpha(f_{p2})(d_{s2} - d_{s1})}{2} + \alpha(f_{p3})(d_p - d_{s2}) \right] - 1 \right). \quad (3.64)$$

It should be noted that Eqs. 3.63 and 3.64 are similar to Eqs. 3.22 and 3.29. From these equations the multiplication factors

$$mf_1(f_{p1}, f_{p2}) = \exp \left[\alpha(f_{p1})d_{s1} + \frac{\alpha(f_{p2})(d_{s2} - d_{s1})}{2} \right] \text{ and} \quad (3.65)$$

$$mf_2(f_{p2}, f_{p3}) = \exp \left[\frac{\alpha(f_{p2})(d_{s2} - d_{s1})}{2} + \alpha(f_{p3})(d_p - d_{s2}) \right] \quad (3.66)$$

are easily obtained, completing the derivation of the trap-to-band impact ionization parameters.

3.3.2 Band-to-Band Impact Ionization

Another possible method for carrier multiplication in ACTFEL devices is band-to-band impact ionization. When band-to-band impact ionization occurs, an energetic conduction band electron in the phosphor collides with an atom in the lattice. This collision excites an electron into the conduction band and therefore also results in a hole in the valence band. Others have asserted that trapping of holes created by band-to-band impact ionization is a method for positive space charge creation in ACTFEL devices. In this model, however, holes created by band-to-band impact ionization are not trapped - they instead recombine instantaneously at the cathodic interface, as shown in Fig. 3.7. Since band-to-band impact ionization is a field-dependent phenomenon most carrier multiplication occurs where the electric field is highest, near the cathodic interface. Holes

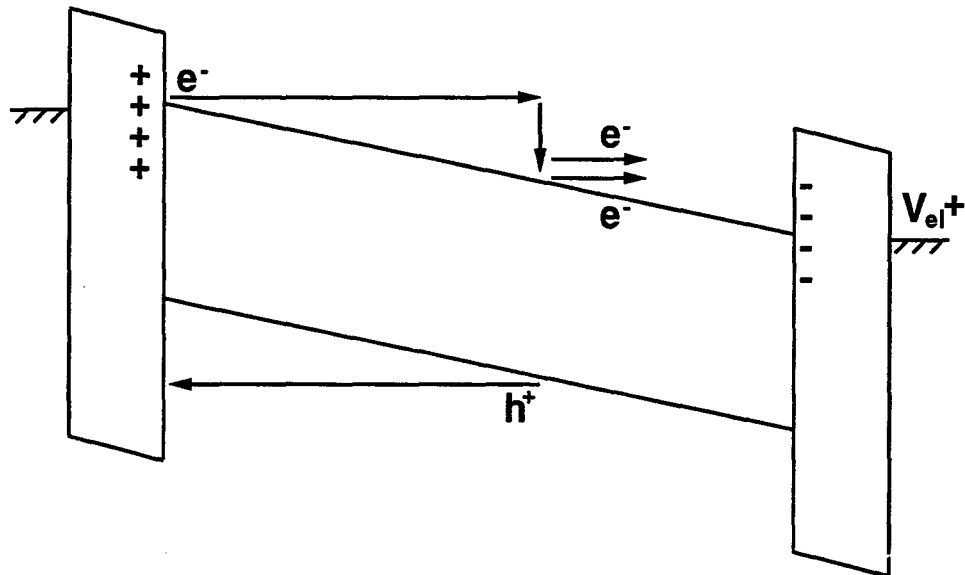


Figure 3.7: Band-to-band impact ionization.

created by band-to-band impact ionization therefore have to travel only a short distance through a high field region to reach the cathodic interface. This makes trapping of holes less likely.

The equations for band-to-band impact ionization are similar to those for trap-to-band impact ionization. The form of the ionization function used is

$$\alpha_{band}(f_p) = \frac{qf_p}{E_{ion}} \exp \left[- \left(\frac{f_0}{f_p} \right)^n \right] \quad n = 1, 2 \quad (3.67)$$

where f_0 is the characteristic field at which band-to-band impact ionization becomes important. Like for the trap-to-band impact ionization case, the three different phosphor fields lead to a different multiplication factor in each region. The final net multiplication factor across the entire phosphor region can be found from the product of the multiplication factors in the three separate regions to yield

$$mf_{bb} = \exp\{\alpha(f_{p1})[d_{s1}] + \alpha(f_{p2})[d_{s2} - d_{s1}] + \alpha(f_{p3})[d_p - d_{s2}]\}. \quad (3.68)$$

The simplest way to incorporate the effect of the band-to-band impact ionization factor, mf_{bb} , into the model is to modify the the insulator-phosphor interface current density terms

$$\frac{\partial q_1}{\partial t} = J_1 + J_1(mf_{bb} - 1) \text{ and} \quad (3.69)$$

$$\frac{\partial q_2}{\partial t} = J_3 - J_1(mf_{bb} - 1). \quad (3.70)$$

If capture of the additional conduction band electrons created by band-to-band impact ionization is allowed at the space charge sheets, modifications to $\frac{\partial q_{sc1}}{\partial t}$ and $\frac{\partial q_{sc2}}{\partial t}$ are also required.

Note that incorporating the band-to-band multiplication factor in the preceding manner will not allow for the additional electrons created to be captured at the space charge sheets.

3.4 Field-Dependent Capture

Thus far, the space charge capture factor, $sccf$, has been mentioned but has not been explained. $sccf$ is a simulation parameter that corresponds to the probability that an electron transiting the phosphor region of the ACTFEL device will be captured at a particular space charge sheet. Because of the two separate sheets of space charge in the two-sheet charge model, two different capture factors, $sccf_1$ and $sccf_2$, are required.

The simplest way to treat $sccf$ is to leave it as a simulation constant and simply choose a value that achieves a match between simulated and experimental data. This solution is not preferred, however, because electron capture is much more likely during certain portions of the applied voltage pulse than others. For example, during the falling portion of the applied voltage pulse or during the interpulse interval, electron capture is much more likely than during the rising portion of the pulse because the average internal field in the phosphor region is lower. To accommodate this effect, one possible treatment of $sccf$ is to set it to zero during the rising portion of an applied voltage pulse and then

to set it to some finite value between zero and one during the remainder of the excitation waveform.

Previous work [4] has shown, however, that capture during the rising portion of a voltage pulse, although unlikely, is in fact an important aspect of ACTFEL device operation. Furthermore, the capture probability during the interpulse interval and falling portion of the applied voltage waveform is not likely to be constant because of changing phosphor field conditions. These realities are the motivation for a field-dependent model for $sccf$. The simplest way to incorporate a field dependency for $sccf$ into the model is to assume that $sccf$ varies linearly with electric field. A possible linear relationship is

$$sccf(f_p) = 1 - \left| \frac{f_p}{f_{0c}} \right| \quad (3.71)$$

where f_{0c} is a critical field below which electron capture is possible. Note that since the capture factor cannot be less than zero, for values of f_p greater than f_{0c} $sccf$ is set to zero. A more complex way to handle $sccf$ is to model its dependence on field as

$$sccf(f_p) = \left(1 - \left| \frac{f_p}{f_{0c}} \right| \right)^n, \quad (3.72)$$

where n is another simulation parameter. The linear model of Eq. 3.71 is just a special case of Eq. 3.72 where $n = 1$. The two-sheet charge model presented in this thesis does not allow negative space charge creation in the phosphor region. This means that when all phosphor traps are filled with electrons ($n_t = 0$), $sccf$ must equal zero regardless of the conditions of the phosphor electric fields. This occupancy correction for $sccf$ can be incorporated into the model by modifying Eq. 3.72 so that

$$sccf(f_p) = \left(1 - \frac{N_{filled}}{N_t} \right) \left(1 - \left| \frac{f_p}{f_{0c}} \right|^n \right). \quad (3.73)$$

It is worth taking a moment to consider how to choose which field value to use for f_p in Eqs. 3.71 - 3.73. First consider the situation shown in Fig. 3.8. When an electron moves from either insulator-phosphor interface towards the center of the phosphor region,

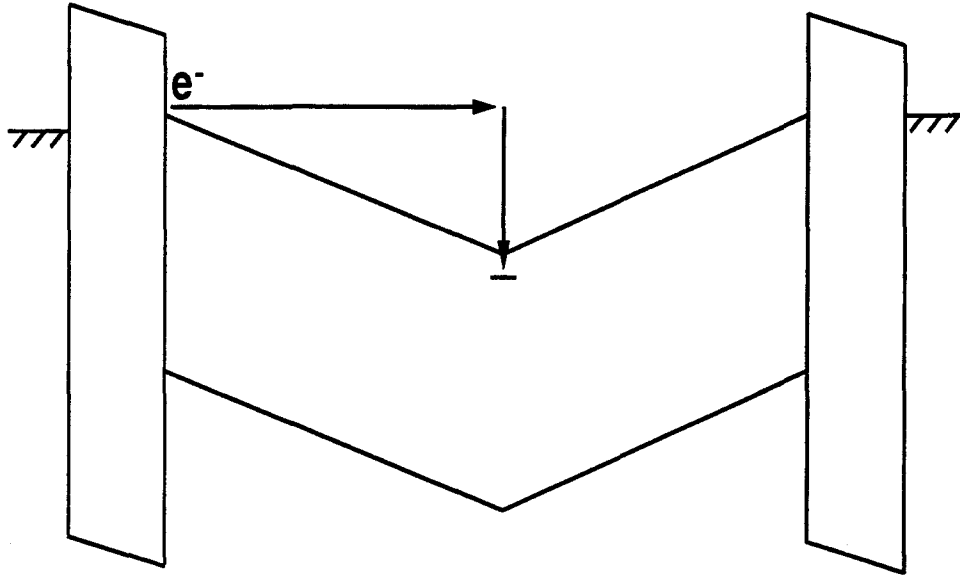


Figure 3.8: Field situation with trapping at the space charge layer likely.

it is likely to be trapped at the space charge layer because of the internal fields. Next, consider Fig. 3.9. An electron emitted from the cathodic interface in this situation is unlikely to recombine at a space charge sheet. These two examples show that both the magnitude and the sign of the electric field in the two regions adjacent to the space charge sheet in question are important. Therefore for q_{sc1} the field of interest that is used in Eqs. 3.71 and 3.72 is

$$f_p = \left| \frac{f_{p1} + f_{p2}}{2} \right| \quad (3.74)$$

and likewise for q_{sc2} ,

$$f_p = \left| \frac{f_{p2} + f_{p3}}{2} \right|. \quad (3.75)$$

Although trapping in phosphor materials has not been studied in detail, Buchanan *et al.* have presented a study of field-dependent capture in SiO_2 . [21] The result presented

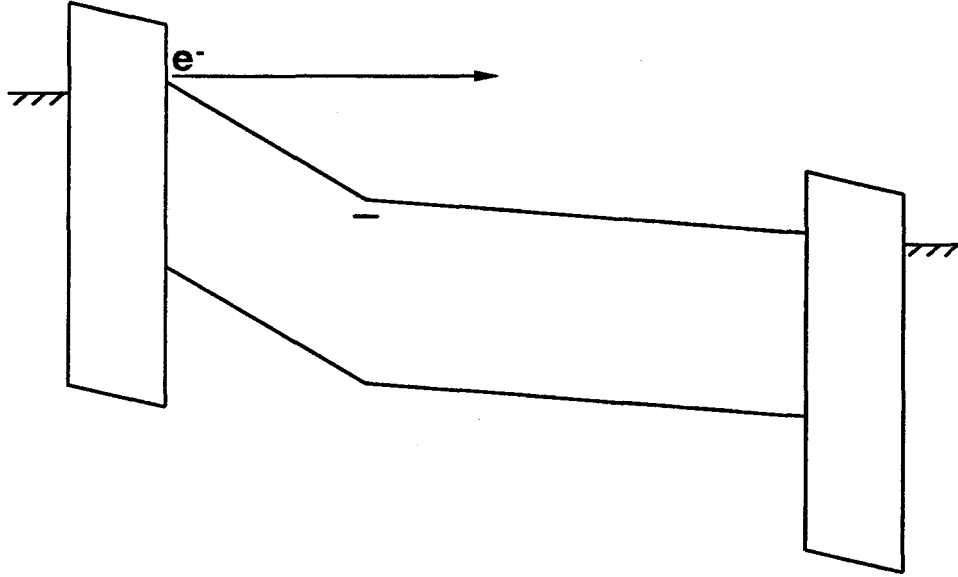


Figure 3.9: Field situation with trapping at the space charge layer unlikely.

in [21] is essentially a fit of the capture cross-section versus the electric field. The fit for SiO_2 is

$$\sigma(f_p) = \begin{cases} (8.944 \times 10^{-9}) f_p^{-1.5} & |f_p| \leq 1.2 \text{ MV/cm} \\ (11.76) f_p^{-3.0} & |f_p| > 1.2 \text{ MV/cm} \end{cases} \quad (3.76)$$

Although Eq. 3.76 is specific to SiO_2 , a generic form of this fit may be applicable to other materials. It should be possible to fit to the capture data of SrS if the prefactors and transition field of Eq. 3.76 are variables.

$sccf$ is a pure probability and not a capture cross-section, but since both σ and $sccf$ are proportional to the number of electrons captured, an equation of the form

$$\sigma(f_p) = \begin{cases} C_1 f_p^{-1.5} & |f_p| \leq f_{0c} \\ C_2 f_p^{-3.0} & |f_p| > f_{0c} \end{cases} \quad (3.77)$$

can be used to evaluate $sccf$ if the parameters are adjusted such that the $sccf$ approaches

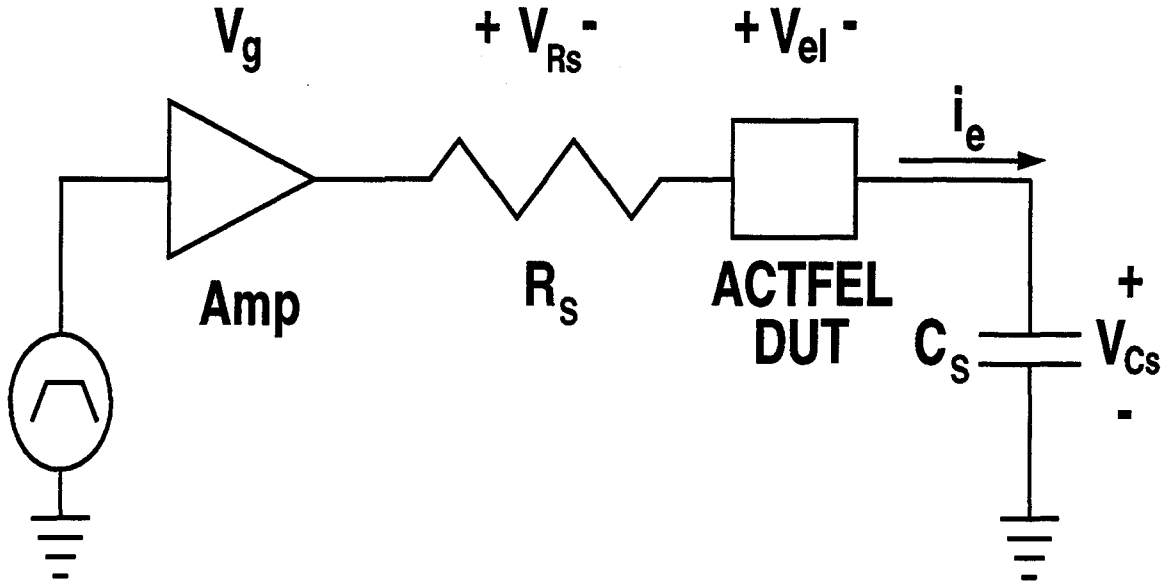


Figure 3.10: The ACTFEL device test circuit.

zero at high fields and one at low fields. C_1 and C_2 are simulation constants which are adjusted to best fit the experimental data.

For the most part, the simulation results presented in this thesis have utilized Eqs. 3.71 and 3.72 for *sccf*. Simulation has shown that results do not vary dramatically as the exponential factor, n , in Eq. 3.72 is varied.

3.5 Effects of the Test Circuit on Device Characterization

Despite the fact that the two-sheet charge model as presented thus far completely describes the relevant device physics behavior of the ACTFEL device, it is not sufficient to explain all of the trends observed experimentally. In order to more accurately simulate ACTFEL devices, it is necessary to include the effects of the external test circuit. Figure 3.10 shows the ACTFEL device test circuit and indicates how the applied voltage is dropped across the series resistance, v_{R_s} , and the sense capacitor, v_{C_s} , as well as across the ACTFEL device, v_{el} , during device operation. A typical voltage pulse applied across

an ACTFEL has a slew rate on the order of 30 V/ μ sec. This large slew rate causes a significant displacement current during the rising portion of the pulse,

$$i_e = c_{tot} \frac{dv}{dt}, \quad (3.78)$$

where i_e is external current, c_{tot} is the series combination of the ACTFEL device capacitance, c_t , and sense capacitor c_s ,

$$c_{tot} = \frac{c_t c_s}{c_t + c_s} \quad (3.79)$$

and $\frac{dv}{dt}$ is the slew rate across c_{tot} . From Kirchoff's Current Law, the current through the ACTFEL device found from Eq. 3.78 must be the same as the current through the sense resistor R_s . This current leads to a voltage drop across R_s and, therefore, v_{el} will be smaller than expected for experimental measurements. At device turn-on the ACTFEL device current is especially large because of dynamic space charge creation. As can be seen from Eq. 3.78, a reduction in $\frac{dv}{dt}$ and an increase in i_e increases the measured capacitance c_{tot} . An increase in measured capacitance means an increase in c_t since c_s is a fixed value. An increase in c_t above the value of the physical insulator capacitance is known as capacitance overshoot and is often seen in experimental C-V curves. Both a reduction in slew rate and an increase in current lead to capacitance overshoot, so both series resistance effects and dynamic space charge creation are responsible for the capacitance overshoot seen experimentally. Some of the applied voltage will also be dropped across c_s . This voltage drop is usually quite small compared to the voltage across R_s if c_s is much larger than the ACTFEL device insulator capacitance.

Simulated C-V and Q- F_p curves using ideal trapezoidal voltage pulses in the two-sheet charge model show less overshoot than found experimentally if external circuit effects are not accounted for in the simulation. One method for making simulated and experimental curves more similar is to use an extremely small R_s and long pulses when taking experimental data. [14] These long pulses are still bipolar trapezoidal voltage waveforms,

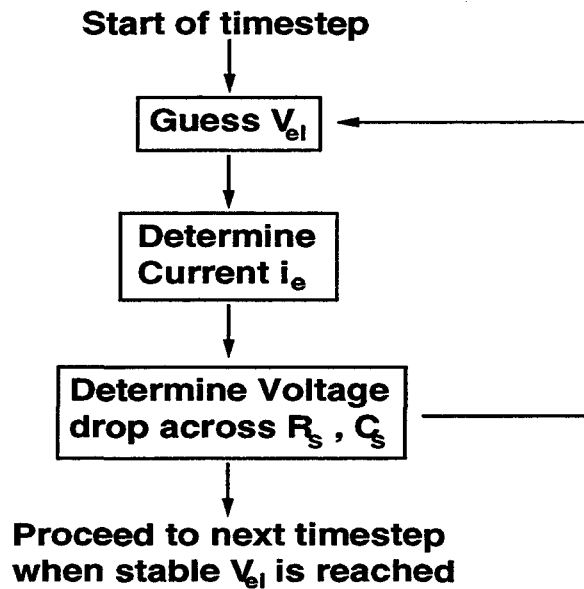


Figure 3.11: The iterative procedure used to include external test circuit effects.

but have a typical rise, fall, and pulse width time of $200 \mu\text{sec}$. These two changes result in a closer to ideal v_{el} because the voltage drop across R_s is small, due to the small value of R_s and the smaller slew rate. Although this long pulse method leads to better agreement between simulation and experiment, it only reduces the effects of the test circuit but does not account for or eliminate them. A superior approach is to simply include the effects of the test circuit in the simulation.

The objective of the external circuit routine in the simulation program is to determine the voltage drop across the ACTFEL device, v_{el} , at each timestep. v_{el} must be solved for in an iterative fashion because the ACTFEL device acts as a voltage-variable capacitor, as explained in Chapter 2. Figure 3.11 shows the general iterative procedure employed. At the start of each timestep, a guess for the voltage across the ACTFEL device at the end of the timestep is made. From this guess, the slew rate across the ACTFEL device, $\frac{dv_{el}}{dt}$, is calculated. Next, the external current is found from

$$i_e = A \left[c_i \frac{dv_{el}}{dt} + \left(c_i d_{s1} \frac{\partial f_{p1}}{\partial t} + c_i (d_{s2} - d_{s1}) \frac{\partial f_{p2}}{\partial t} + c_i (d_p - d_{s2}) \frac{\partial f_{p3}}{\partial t} \right) \right] \quad (3.80)$$

where c_i is the insulator capacitance and A is the cross sectional area of the ACTFEL device. Once the external current is obtained, the slew rate across c_s is obtained from

$$\frac{dv_{c_s}}{dt} = \frac{i_e}{c_s}. \quad (3.81)$$

The voltage drop across c_s at the end of the timestep can now be calculated from the previous value of v_{c_s} ,

$$v_{c_s} = v_{c_s \text{old}} + \frac{dv_{c_s}}{dt} \Delta T \quad (3.82)$$

where ΔT is the value of the timestep. The voltage across R_s is

$$v_{R_s} = i_e R_s. \quad (3.83)$$

Now that the voltage drop across the series resistor and the sense capacitor are known, the voltage across the ACTFEL device is calculated by subtracting from the externally applied voltage:

$$v_{el} = v_a - v_{R_s} - v_{c_s}. \quad (3.84)$$

The value of v_{el} from Eq. 3.84 is compared to the initial guess for v_{el} . If the values are not reasonably close, a new guess for v_{el} is made and the iterative process begins again. By using the routine described above, simulated C-V and $Q - F_p$ curves with realistic more overshoot are obtained.

Despite the fact that v_{c_s} is calculated at the end of each timestep, this voltage cannot be used to calculate C-V and $Q - F_p$ electrical characterization curves as in the experimental case. The purpose of including circuit effects in the simulation is to give an estimate of the voltage dropped across the ACTFEL device in relation to the externally

applied voltage. The external circuit routine is a late addition to the program and the results obtained via this routine are estimates of limited precision, not suited to the generation of characterization curves. Instead, simulated C-V and $Q - F_p$ curves are generated from internal quantities.

$Q - F_p$ curves show the internal charge in the phosphor region of an ACTFEL device plotted versus the average electric field in the phosphor region. The average phosphor field, f_p , is determined directly from the internal fields,

$$f_p = \left(\frac{1}{d_p} \right) (d_{s1}f_{p1} + (d_{s2} - d_{s1})f_{p2} + (d_p - d_{s2})f_{p3}). \quad (3.85)$$

Instead of calculating the external charge from the sense capacitor, as in the experimental case, q_{ext} is found from

$$q_{ext} = c_i(v_{el} + f_p d_p) = c_i v_i \quad (3.86)$$

where v_i is the voltage dropped across the ACTFEL device insulators. The desired quantity of internal charge is then calculated from q_{ext} ,

$$q_{int} = \left(\frac{c_i + c_p}{c_i} \right) q_{ext} - c_p v_{el} \quad (3.87)$$

where c_p is the capacitance of the phosphor region. The total ACTFEL device capacitance used in simulated C-V curves is determined from the slew rate across the ACTFEL device,

$$c_t = c_i + c_i \left(\frac{dv_{el}}{dt} \right)^{-1} \left(d_{s1} \frac{\partial f_{p1}}{\partial t} + (d_{s2} - d_{s1}) \frac{\partial f_{p2}}{\partial t} + (d_p - d_{s2}) \frac{\partial f_{p3}}{\partial t} \right). \quad (3.88)$$

3.6 Model Stability

Before discussing experimental results, a brief discussion of the stability of the two-sheet charge model is in order. Several criteria must be met in order to insure successful ACTFEL device simulation. Most importantly, charge must be conserved within the

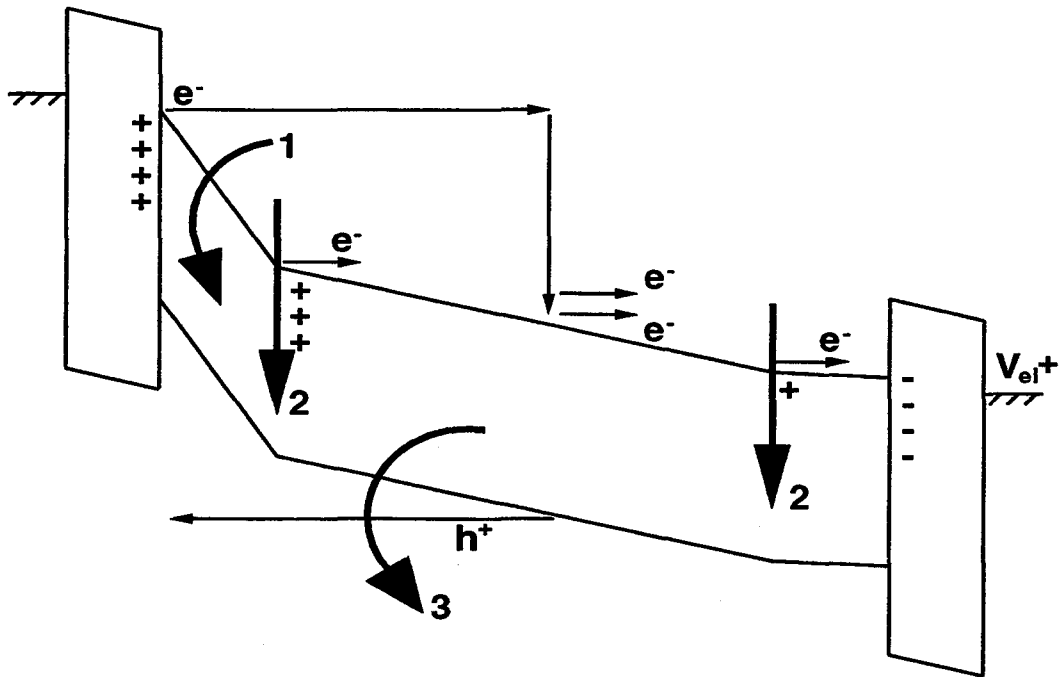


Figure 3.12: Energy band diagram illustrating feedback effects during the rising edge of a positive voltage pulse for (1) interface emission (negative feedback), (2) space charge creation (positive feedback), and (3) band-to-band impact ionization (negative feedback). A downward arrow indicates a lowering of the energy band at a sheet in the phosphor region, while a curved arrow indicates a reduction in the slope of a portion of the energy band.

ACTFEL device. If the $\frac{\partial q}{\partial t}$ terms are written in such a way that excess charge is being created, the simulation very quickly proves unstable. Additionally, in order to obtain reliable results, dynamic space charge must reach a steady-state condition. This means that as much space charge as is created through trap-to-band impact ionization must be annihilated through electron capture. This effect is more subtle than charge balance, but is equally important. Using an equation such as Eq. 3.23 results in more space charge creation than annihilation, and gives questionable simulation results.

The phosphor field differential equations presented in this chapter must be solved numerically in the simulation program. To insure that the solver can obtain reliable

solutions to the electric field differential equations it is important that the simulation parameters are adjusted such that charge flow within the ACTFEL device does not lead to positive feedback effects. Avoiding positive feedback is especially critical at device turn-on. Figure 3.12 shows some of the feedback effects that are active during the rising edge of a positive voltage pulse. Emission of electrons from the cathodic interface and collection at the anodic interface is a negative feedback effect. Transport of electrons across the phosphor region results in positive charge at the cathodic interface and negative charge at the anodic interface, causing a counterfield in the phosphor region that opposes the applied voltage, as discussed in Chapter 2. This reduction in average phosphor field leads to a lower electron emission rate from the cathode.

The feedback effects resulting from space charge creation by trap-to-band impact ionization are initially positive. Space charge creation tends to reduce the phosphor field nearer the anode but to increase the field near the cathode, resulting in increased electron emission from the cathodic interface. The increased cathode field also means that trap-to-band impact ionization is more likely. The exponential nature of trap-to-band impact ionization, however, means that this positive feedback effect is short lived. Soon after device turn-on, all the phosphor traps are empty. Simulation results suggest that excess space charge creation by impact ionization has a destabilizing effect on ACTFEL device simulation. In order to balance the feedback effects of trap-to-band impact ionization, it is sometimes necessary to increase the amount of band-to-band impact ionization occurring in the simulation. Band-to-band impact ionization is clearly a negative feedback effect, as the holes traveling towards the cathodic interface and electrons towards the anodic interface will reduce the average phosphor field.

The type of differential equation solver employed also has some effect on simulation stability. The relationships between the internal phosphor electric field, space charge creation, and interface emission are all highly non-linear. The relations for these quantities may be what is known as a set of stiff differential equations. Stiff equations vary on

two or more different timescales. [22] For example, the equations for field emission are highly time-dependent during the rising portion of the applied voltage pulse, but reach a near-steady-state condition later. In order for a traditional differential equation solver to accurately solve for the field emission rates, a small timestep is required. The small timestep is unnecessary, however, during much of the applied voltage pulse. A stiff differential equation solver may be able improve simulation accuracy during some portions of the waveform and increase computational efficiency in others. The results presented in this thesis were obtained using a fourth order Runge-Kutta solver with an adaptive stepsize algorithm, which probably works as well as would a stiff solver.

4. SIMULATION RESULTS

Presented in this chapter are simulation results obtained from a variety of different versions of the two-sheet charge model program. First, results from the two-sheet charge model with space charge creation by field emission from bulk traps are presented, using the model proposed by Keir. [3] The model described in Chapter 3 is then used to show the type of results possible when space charge is created through trap-to-band impact ionization. Results from these models are also presented with the effects of the test circuit considered.

4.1 Static and Dynamic Space Charge

A discussion of the nature of ACTFEL device space charge and the cause of overshoot is in order before the presentation of simulation results. ACTFEL devices are characterized by two types of space charge, static and dynamic. Both types of space charge are created simultaneously during the rising portion of an applied voltage pulse. When the first voltage pulse is applied to a reset ACTFEL device (a device containing no space charge), electrons may be emitted from traps in the phosphor as soon as electron emission from the insulator-phosphor interfaces begins. This electron emission from traps in the phosphor leaves behind positive space charge. During the falling portion of an applied voltage pulse or during an interpulse interval, electrons at the anodic interface may be re-emitted and flow back across the device. The field conditions during these portions of the applied waveform are such that some of the re-emitted electrons recombine in the phosphor region, thus annihilating positive space charge. Space charge that is created during the rising portion of the applied voltage pulse and annihilated at the end of the same pulse is known as dynamic space charge. If not enough electrons are captured at the end of the applied voltage pulse to eliminate all the space charge created, some space charge remains at the start of the next pulse. This charge is known as static space charge.

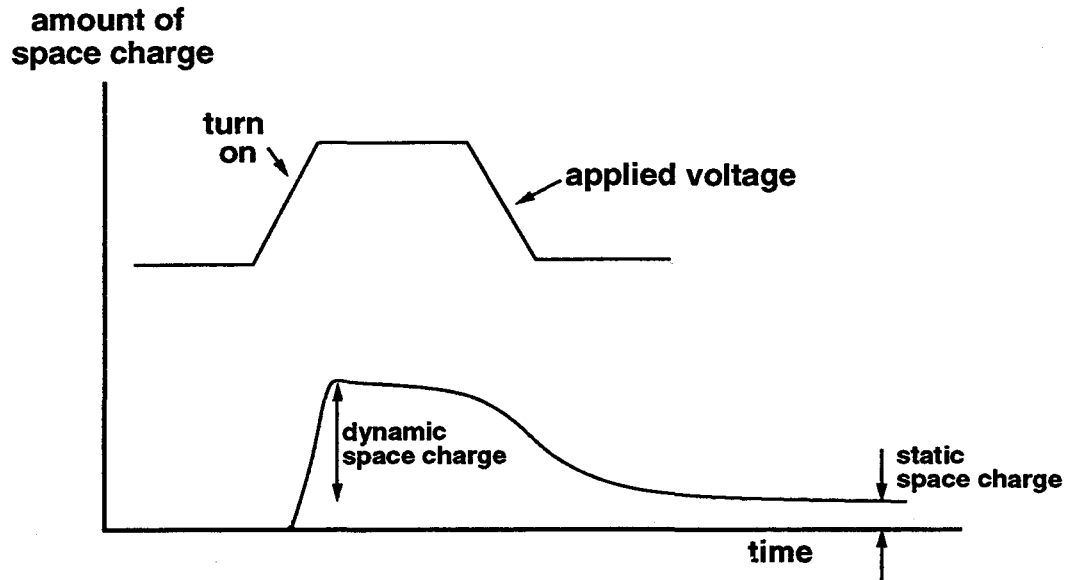


Figure 4.1: The space charge creation cycle.

Figure 4.1 is a plot of the steady-state space charge creation/annihilation cycle. The offset at the end of the pulse represents static space charge, while the peak near turn on represents dynamic space charge creation. The type of space charge of interest in this thesis is dynamic space charge. Dynamic space charge creation is thought to be the cause of overshoot because the charge flow that results from space charge creation perturbs the voltage drop across the phosphor layer. As the applied voltage across the ACTFEL device increases, dynamic space charge creation causes the voltage dropped across the phosphor region to decrease, causing an apparent negative dynamic phosphor capacitance. This negative phosphor capacitance is the cause of overshoot. The largest overshoot is observed when a large amount of space charge is created in a very brief period of time, because this leads to more charge flow and a greater reduction in phosphor voltage. The effects of static space charge are not discussed in any detail in this thesis, in part because an accurate model of the static space charge profile is not possible using

only two sheets of charge in the phosphor region. Additionally, the effects of static space charge are not directly evident in $Q - F_p$ and C-V electrical characterization, which are the two main types of results presented in this thesis.

4.2 Simulation Results Using the Two-Sheet Charge Model with Space Charge Creation by Field Emission

The two-sheet charge program with space charge creation by field emission from bulk traps can be used to generate accurate simulation results for ZnS:Mn devices. The field emission model parameters can be adjusted to create much static space charge and little dynamic space charge, so this model is appropriate for ZnS:Mn modeling. Field emission is not a suitable mechanism, however, for creating a large amount of dynamic space charge as sometimes observed in SrS devices. Two attempts at adapting the field emission model for simulation of SrS devices are presented in this section.

4.2.1 Simulation Results Using Standard Voltage Pulses

The field emission model is adapted to SrS devices by reoptimizing the simulation parameters from the values used in the simulation of ZnS:Mn devices. In this section standard short voltage pulses, as shown in Fig. 2.2, are used as the ACTFEL device voltage excitation waveform. Table 4.1 shows typical field emission simulation parameters used for SrS ACTFEL device simulation.

Figure 4.2 shows a typical experimental $Q - F_p$ curve along with a simulated curve for a SrS:Ce ACTFEL device. The simulation parameters for the curve shown are chosen to obtain a reasonable match for the maximum phosphor electric field, F_{max} , and the maximum internal charge, Q_{max} . With model parameters adjusted such that this match is obtained, the field overshoot during the rising part of the voltage pulse evident in the experimental curve is simply not present in the simulated curve.

Obtaining greater field overshoot in simulation using the field emission program is possible. Adjusting the simulation parameters such that the interface trap depth is 1.5

Table 4.1: Simulation parameters for the field emission two-sheet charge model.

Parameter	Description	Nominal Parameter Value
ϵ_p	phosphor dielectric constant	9.4
ϵ_i	insulator dielectric constant	18.6
d_{i1}	thickness of insulator 1	2700 Å
d_{i2}	thickness of insulator 2	2700 Å
d_p	thickness of phosphor layer	7000 Å
d_{s1}	space charge location 1	2000 Å
d_{s2}	space charge location 2	5000 Å
$N_0 f_0(ip)$	no-field interface occupation	$5 \times 10^{13} \text{ cm}^{-2}$
E_{ion}	band-to-band effective ionization energy	5.4 eV
f_0	band-to-band characteristic field	3.1 MV/cm
E_{it}	interface trap depth	1.0 eV
N_T	deep-level trap concentration	$5 \times 10^{17} \text{ cm}^{-3}$
E_{sc}	space charge trap depth	0.9 eV

eV and the phosphor trap is 0.75 eV, as well as moving the space charge sheets very close to the phosphor-insulator interfaces (about 50 Å) produces more overshoot. Figure 4.3 shows a simulated $Q - F_p$ curve with more overshoot, along with an experimental curve for a SrS:Ce ACTFEL device. Despite the larger phosphor field overshoot of the simulated curve shown in Fig. 4.3, the parameters used to obtain this curve are physically unrealistic. The shallow phosphor trap depth relative to the interface trap depth value means that a significant amount of space charge is created before turn on. Experimentally, however, ACTFEL devices do not appear to show a large amount of sub-turn-on space charge current. Furthermore, placing the space charge sheets extremely close to the two

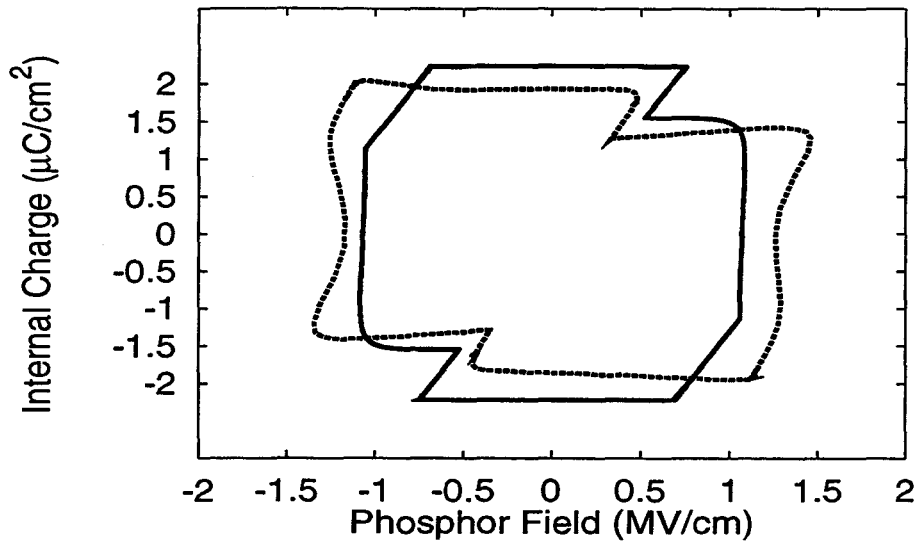


Figure 4.2: Simulated (solid line) and experimental (dashed line) $Q - F_p$ curves for a SrS:Ce ACTFEL device using the field emission program.

interfaces means that space charge is located entirely at the periphery of the phosphor region. Although field conditions may dictate that much dynamic space charge is created near the ends of the phosphor region, previous work has shown that space charge is created throughout the ACTFEL device. [13] Although simulated data has only been compared to SrS:Ce experimental data thus far, experimental curves obtained with other types of ACTFEL devices such as SrS:Cu are similar to those obtained with SrS:Ce ACTFEL devices. Since the field emission program cannot accurately match the experimental data for any type of SrS device when realistic simulation parameters are used, a detailed comparison of simulated curves to different kinds of SrS devices is omitted.

Simulated C-V curves using the field emission program also do not show as much capacitance overshoot as is seen experimentally. Figure 4.4 contains a typical experimental C-V curve for a SrS:Ce device along with a simulated C-V curve generated using the field emission program with the same parameters as the curve of Fig. 4.3. Clearly, the simulated

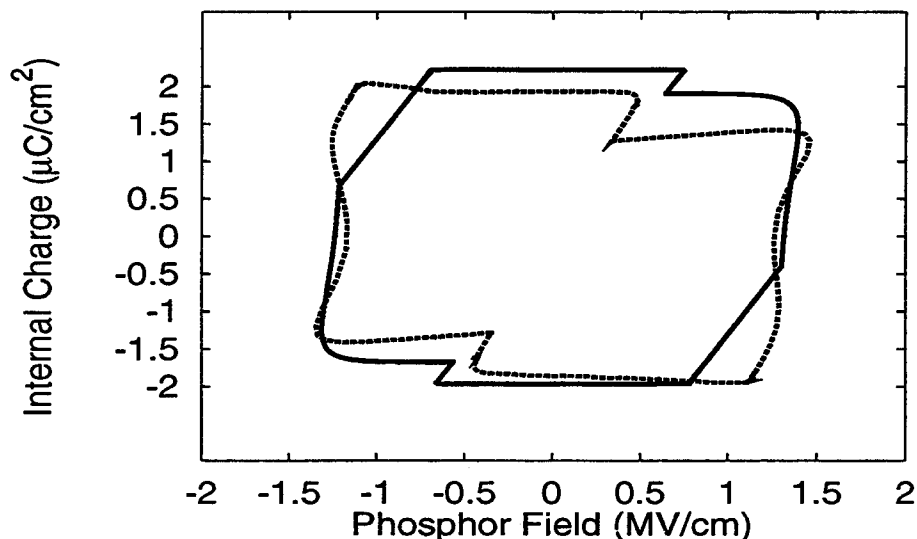


Figure 4.3: Simulated (solid line) and experimental (dashed line) $Q - F_p$ curves for a SrS:Ce ACTFEL device with greater simulated phosphor field overshoot.

curve does not show anywhere near as much capacitance overshoot as the experimental curve. Simulated C-V curves obtained from the field emission program do not show much capacitance overshoot, no matter what set of simulation parameters are chosen. Because of the inability of the field emission program to accurately simulate $Q - F_p$ and C-V curves for SrS ACTFEL devices using standard voltage pulses, a different approach to ACTFEL device simulation is necessary.

4.2.2 Simulation Results Using Long Voltage Pulses

One method used to obtain a better match between simulated and experimental data for SrS ACTFEL devices is to use long applied voltage pulses. [14] Figure 4.5 shows a long voltage pulse waveform. As discussed in Sec. 3.5, series resistance effects cause more $Q - F_p$ and C-V overshoot when the external slew rate across the ACTFEL device is larger. Using a long pulse, with its reduced slew rate, to obtain experimental data leads

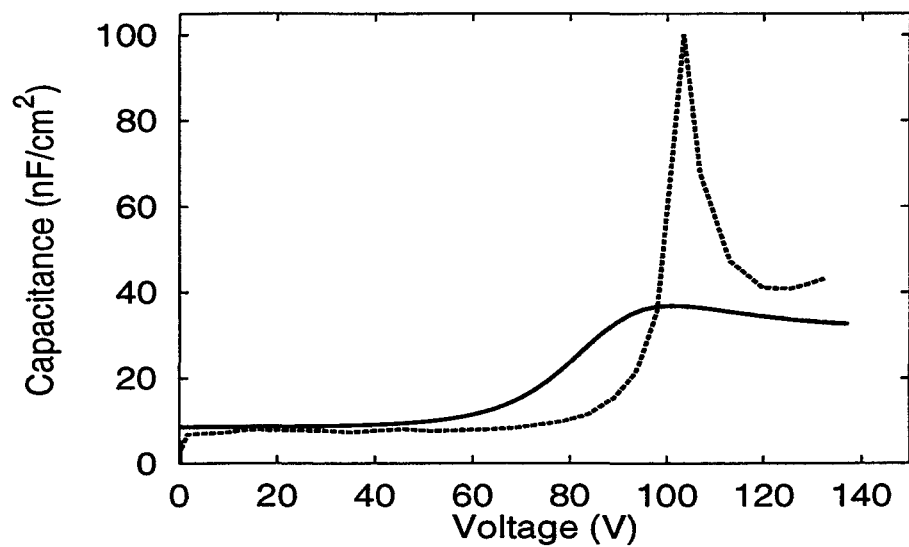


Figure 4.4: Simulated (solid line) and experimental (dashed line) C-V curves for a SrS:Ce ACTFEL device with a small amount of simulated overshoot.

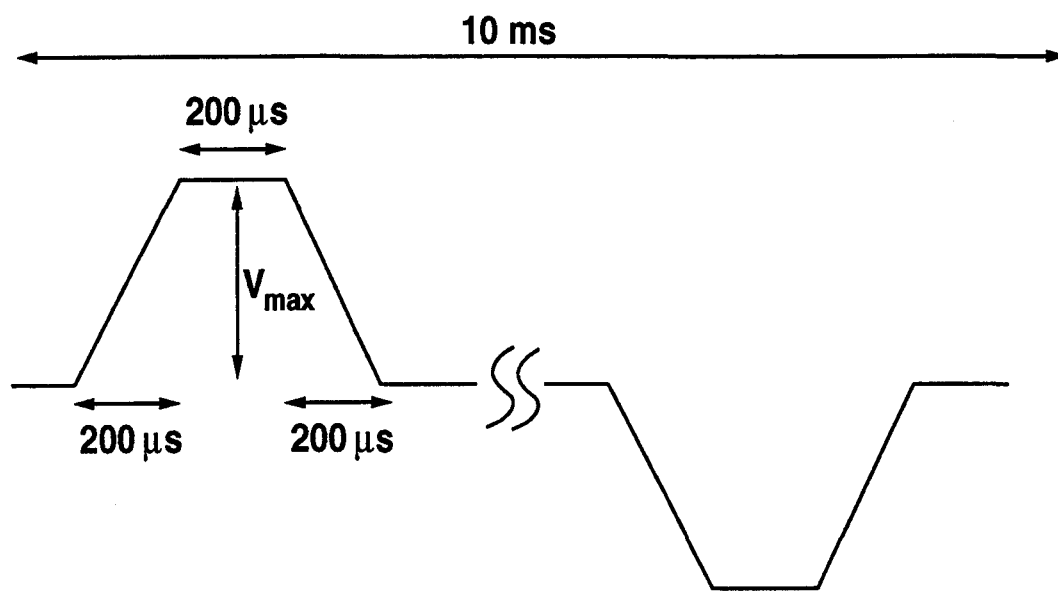


Figure 4.5: The long trapezoidal voltage pulse waveform.

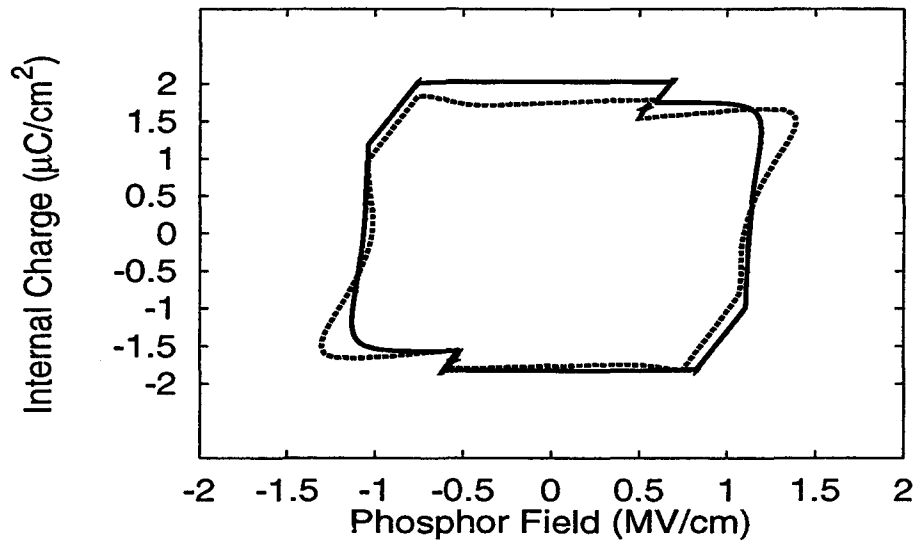


Figure 4.6: Simulated (solid line) and experimental (dashed line) $Q - F_p$ curves for a SrS:Ce device obtained using long pulses.

to smaller $Q - F_p$ and C-V overshoot and a better match with simulated data when circuit effects are not included in the simulation.

Figure 4.6 shows experimental and simulated $Q - F_p$ curves obtained using long pulses and the field emission program for a SrS:Ce ACTFEL device. The simulated data is obtained using simulation parameters similar to those used to obtain the curve of Fig 4.3. The experimental and simulated curves shown in Fig. 4.6 look more alike than do the two curves of Fig. 4.2. Specifically, the maximum field and charge match more closely and the shape of the relaxation charge now looks more similar for the two curves. This is not because of any improvement in the quality of the simulated curves, but because of a change in the experimental data. The more curved look of the short pulse experimental curve is due to RC effects which are not simulated in the basic version of the program; using a long pulse somewhat reduces the RC effect in the experimental curve. As with short pulses, it is possible to obtain more overshoot by using physically unrealistic simulation

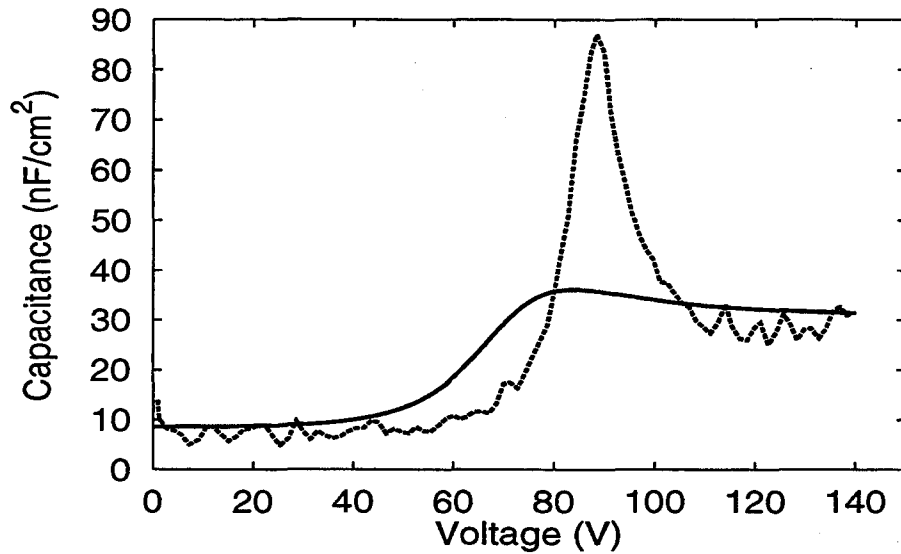


Figure 4.7: Simulated (solid line) and experimental (dashed line) C-V curves obtained for a SrS:Ce ACTFEL device using long pulses.

parameters. The goal of this thesis is accurate simulation with realistic parameters, so that course is not pursued further.

In Fig. 4.7, experimental and simulated C-V curves are plotted for a SrS:Ce device using long voltage pulses. Again, the match between simulated and experimental data is better than with standard voltage pulses, but the amount of simulated capacitance overshoot is still insufficient. Variation of the simulation parameters does not lead to an appreciably better match than that shown in Fig. 4.7. Analysis of the field emission simulation results leads to the conclusion that in order to account for the overshoot seen in experimental SrS curves, more dynamic space charge creation is necessary than is possible with this version of the simulation program.

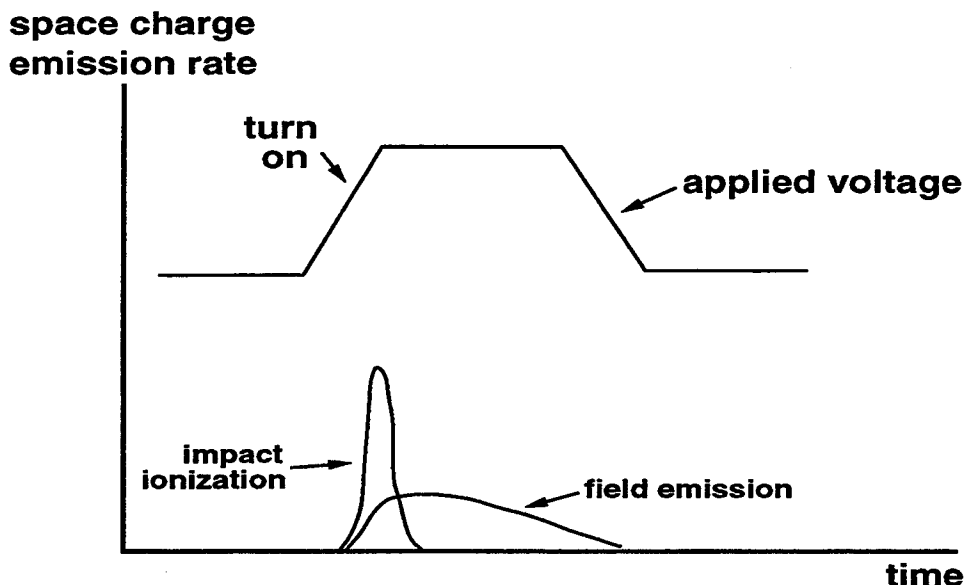


Figure 4.8: Electron emission rate from the space charge layer closest to the cathodic insulator-phosphor interface for both field emission and trap-to-band impact ionization.

4.3 Simulation Results With Space Charge Creation by Trap-to-Band Impact Ionization

There are two problems inherent with field emission simulations of dynamic space charge creation: (i) field emission is a negative feedback effect which tends to shut itself off, limiting the maximum amount of space charge created, and (ii) field emission tends to create space charge over a fairly long period of time. As discussed in Sec. 4.1, the maximum amount of overshoot is obtained when a large amount of space charge is created in a brief period of time. The exponential form of the equations for trap-to-band impact ionization (Sec. 3.3.1) and the fact that the amount of space charge created is a function of the cathode field means that trap-to-band impact ionization is likely to create a large amount of space charge very rapidly above device turn on.

Figure 4.8 is a plot of the electron emission rate from the space charge sheet closest to the cathodic insulator-phosphor interface as a function of time. As shown, trap-to-

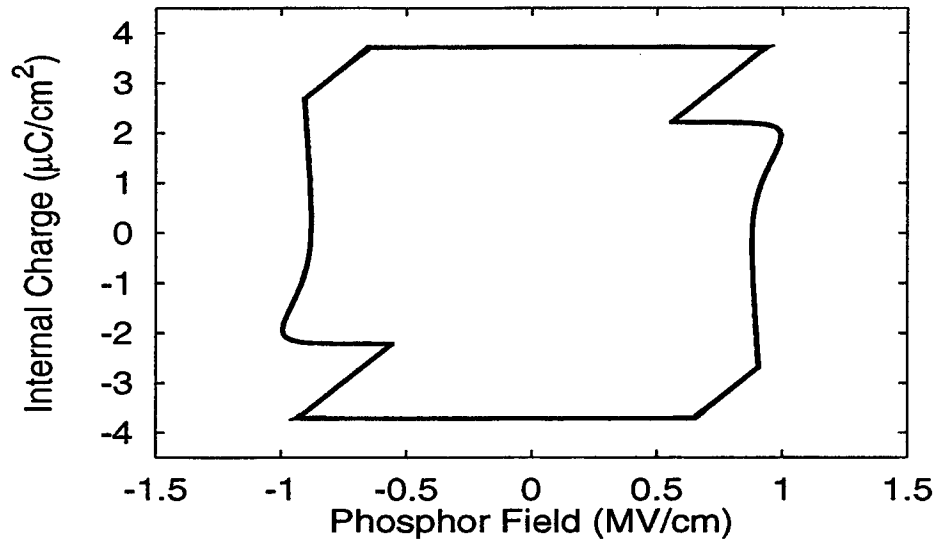


Figure 4.9: Generic simulated $Q - F_p$ curve obtained using the two-sheet charge model with space charge creation by trap-to-band impact ionization.

band impact ionization creates a large amount of space charge in a very brief period of time, while field emission creates space charge more slowly. The positive feedback effect inherent in trap-to-band impact ionization means that once space charge creation starts, all of the phosphor traps will be emptied very quickly. Field emission from bulk traps, on the other hand, depends on the anode field and therefore tends to slowly shut itself off. Thus, the emission rate characteristics of space charge creation by trap-to-band impact ionization make it the more likely mechanism for space charge creation in devices exhibiting significant overshoot.

Using the two-sheet charge model with space charge creation by trap-to-band impact ionization, as defined in Chapter 3, but without considering the effects of the external test circuit, simulated $Q - F_p$ and C-V curves are presented in Figs. 4.9 and 4.10, respectively. These curves are obtained using the standard applied voltage pulse waveform. The model parameters used to obtain these simulated curves are similar to those used to obtain the

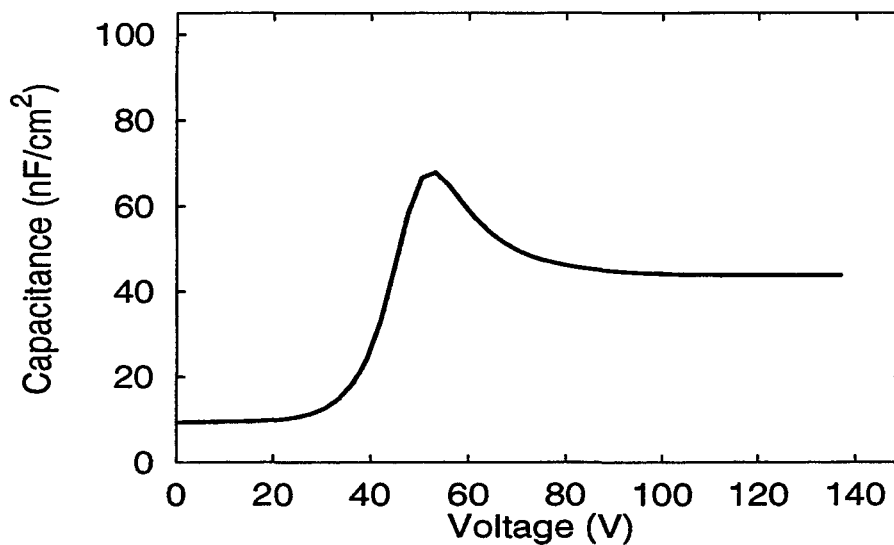


Figure 4.10: Generic simulated C-V curve obtained using the two-sheet charge model with space charge creation by trap-to-band impact ionization.

field emission curves presented previously in this chapter (see Table 4.1). The difference is that instead of specifying a space charge trap depth, as in the field emission case, a characteristic field for trap-to-band impact ionization of 3.0 MV/cm is used. Essentially, the results presented in the section are for a generic SrS ACTFEL device. Although the simulated curves presented exhibit more overshoot than their field emission counterparts, the magnitude of both the capacitance and field overshoot is not great enough to accurately reflect the amount of overshoot seen experimentally.

4.4 Simulation Results With Effects of the Test Circuit Considered

A method for obtaining more realistic simulation results when a standard applied voltage pulse waveform is used is to simulate the entire test circuit instead of simply simulating the ACTFEL device, as discussed in Sec. 3.5. If the effects of R_s are included in

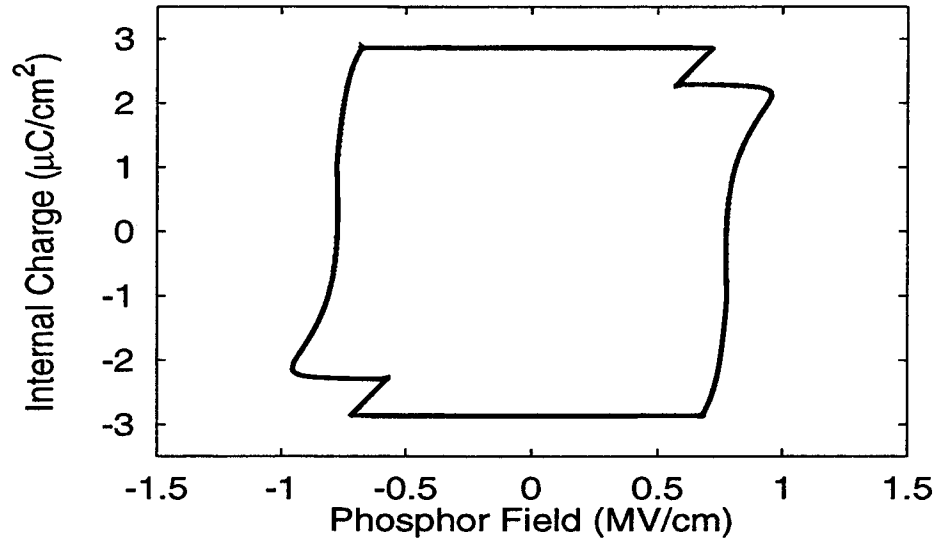


Figure 4.11: Simulated $Q - F_p$ curve obtained using the two-sheet charge model with space charge creation by trap-to-band impact ionization and effects of the test circuit considered, with $R_s = 400 \Omega$ and $C_s = 101 \text{ nF}$.

the simulation, long pulses are no longer required in order to obtain reasonable agreement between simulation and experiment.

4.4.1 Simulation With Space Charge Creation by Trap-to-Band Impact Ionization

For simulation of SrS ACTFEL devices, accounting for test circuit effects along with space charge creation by trap-to-band impact ionization provides the most realistic results. Figure 4.11 shows simulated $Q - F_p$ curves for a SrS ACTFEL device with space charge creation by trap-to-band impact ionization while considering the effects of the test circuit ($R_s = 400 \Omega$) and using a standard voltage pulse. Figure 4.12 shows the C-V curve corresponding to the $Q - F_p$ curve of Fig. 4.11. The model parameters used to obtain these results are the same as for the simulated curves presented in Sec. 4.3, with the addition of R_s and the sense capacitor. These figures show many of the features of the

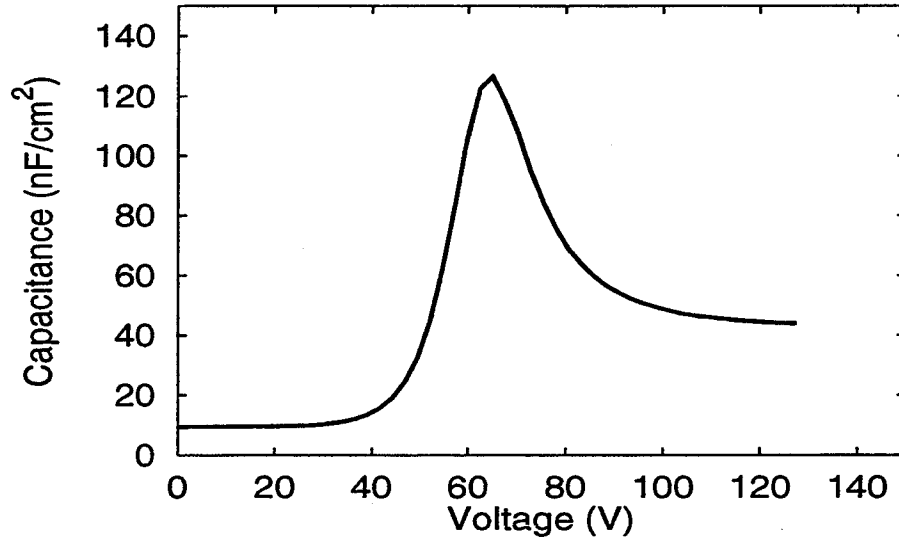


Figure 4.12: Simulated C-V curve obtained using the two-sheet charge model with space charge creation by trap-to-band impact ionization and effects of the test circuit considered, with $R_s = 400 \Omega$ and $C_s = 101 \text{ nF}$.

experimental characterization curves which were previously unattainable in simulation. Not only do these curves match up well with experimental data in terms of the magnitude of overshoot, they also exhibit the more rounded look of experimental data, especially with regard to the relaxation charge portion of the $Q - F_p$ waveform. This rounded look is essentially an RC effect which was not modeled previously simulation.

The $Q - F_p$ curve of Fig. 4.11, although it has the same general shape as experimental SrS $Q - F_p$ curves, does not match up well with experimental curves in terms of maximum field and maximum charge. The $Q - F_p$ curve of Fig. 4.13, however, is adjusted such that it closely matches the maximum field and maximum charge of an experimental curve obtained from a SrS:Ce ACTFEL device with $R_s = 100 \Omega$ and a phosphor region thickness of 7000 \AA . The model parameters shown in Table 4.2 are essentially the parameters used to obtain this simulated curve. The only different parameter is interface trap depth, E_{it} , which is set at 1.45 eV to obtain the simulated curve in Fig. 4.13. Despite the fact that

the simulated curve in Fig. 4.13 gives the closest least-squares fit when compared to the experimental curve, the shape of this simulated curve is far from that found experimentally. Specifically, no leakage charge flows in the simulated ACTFEL device, and the simulated curve does not show any phosphor field overshoot. In fact, the shape of the simulated curve of Fig. 4.11 is much closer to the shape of the experimental curve of Fig. 4.13 than is the simulated curve of Fig. 4.13.

Although it is possible to obtain a variety of different curves from simulation, obtaining an accurate match for maximum field, maximum charge, field overshoot, capacitance overshoot, and leakage charge simultaneously has proven impossible with the current model. Several factors contribute to the inability of the model to exactly reproduce any one, unique, experimental result. One of the limiting factors in the current model is that electron and hole trapping processes, as well as re-emission, are not accurately modeled. Revising the space charge capture equations presented in Sec. 3.4 may lead to more realistic device simulation. Additionally, the subtle differences between space charge creation by trap-to-band and band-to-band impact ionization and hole trapping should be explored. Another reason why the shape of the experimental curve in Fig. 4.13 is inaccurate may have to do with the the expression used for phonon-assisted tunneling in the current model (Eq. 3.41). This equation may need to be revised to improve the accuracy of future simulation. Non-ideal amplifier performance also contributes to some variation in experimental results. These amplifier effects are not modeled.

The model parameters used to obtain the simulated curve in Fig. 4.11 are taken as the basis for the variation of parameters performed throughout the remainder of this chapter, and are shown in Table 4.2. These parameters are chosen because the shape of the simulated curve in Fig. 4.13 is not interesting enough to warrant further investigation without model refinement, and because the simulated curve of Fig. 4.11 shows nearly all of the features of experimental curves.

Table 4.2: Simulation parameters for the trap-to-band impact ionization model.

ACTFEL Device and Measurement Circuit Parameters

Parameter	Description	Nominal Parameter Value
ϵ_p	phosphor dielectric constant	9.4
ϵ_i	insulator dielectric constant	20.3
d_{i1}	thickness of insulator 1	2000 Å
d_{i2}	thickness of insulator 2	2000 Å
d_p	thickness of phosphor layer	7000 Å
d_{s1}	space charge location 1	2000 Å
d_{s2}	space charge location 2	5000 Å
$N_0 f_0(ip)$	no-field interface occupation	$5 \times 10^{13} \text{ cm}^{-2}$
E_{ion}	band-to-band effective ionization energy	5.4 eV
f_0	band-to-band characteristic field	3.1 MV/cm
f_{0c}	capture characteristic field	5.0 MV/cm
E_{it}	interface trap depth	1.0 eV
m^*/m	electron effective mass	0.525
σ	capture cross section	10^{-16} cm^2
A	device area	.085 cm ²
R_s	series resistance	400 Ω
C_s	sense capacitance	101 nF

Impact Ionization Parameters

N_T	deep-level trap concentration	$2.3 \times 10^{17} \text{ cm}^{-3}$
E_{ion}^t	trap-to-band effective ionization energy	2.6 eV
f_{0t}	trap-to-band characteristic field	3.2 MV/cm

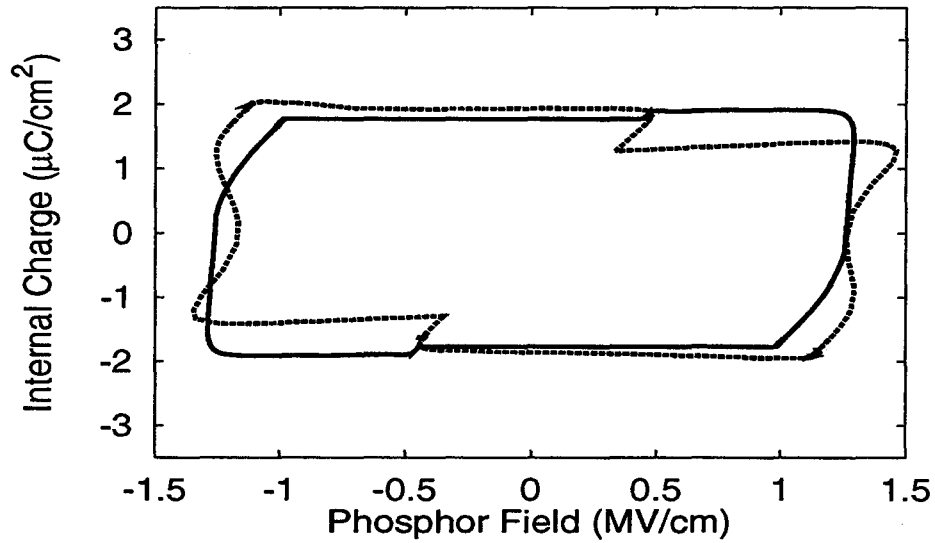


Figure 4.13: Simulated (solid line) and experimental (dashed line) $Q - F_p$ curves for a SrS:Ce ACTFEL device with matching maximum field and charge.

4.4.2 Variation of Simulation Parameters

Now that a model providing a reasonable simulation of SrS ACTFEL devices has been demonstrated, an examination of the model parameters is of interest to determine the sensitivity of the simulation to variation of the model parameters. Figures showing families of simulated curves with one of the model parameters varied while the others are held fixed are presented and discussed.

Trap density in the phosphor, N_T , has a large influence on the amount of dynamic space charge creation and hence on the magnitude of overshoot that an ACTFEL device exhibits. Figures 4.14 and 4.15 contain $Q - F_p$ and C-V curves plotted using different values of N_T . A larger N_T means that a larger amount of space charge creation is possible. This additional space charge is most clearly visible during the leakage charge portion of the $Q - F_p$ curves, as the curves with the larger N_T exhibit more leakage charge. This family of C-V curves reveals a very interesting result - the plot with the largest N_T does

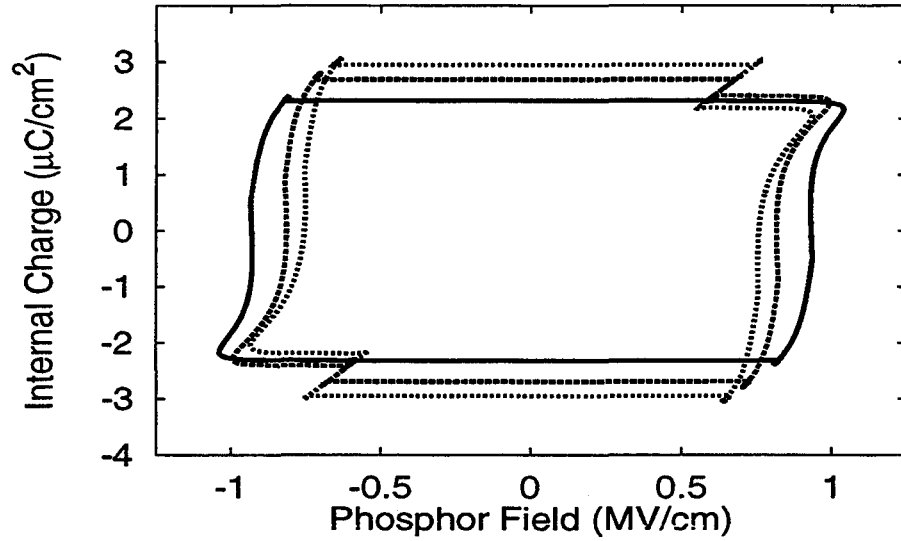


Figure 4.14: Family of simulated $Q - F_p$ curves with N_T set at $1.5 \times 10^{17} \text{ cm}^{-3}$ (solid line), $2 \times 10^{17} \text{ cm}^{-3}$ (dashed line), and $2.3 \times 10^{17} \text{ cm}^{-3}$ (dotted line). Nominal simulation parameters are given in Table 4.2.

not show the most capacitance overshoot. A possible explanation for this phenomenon is that the increased charge flow due to space charge creation in the device with the largest N_T leads to a large counterfield in the phosphor region of the ACTFEL device. The counterfield leads to less dynamic space charge creation on the next pulse, and a lower steady-state amount of dynamic space charge than for a smaller N_T .

One of the main assertions of this thesis is that series resistance effects contribute to capacitance overshoot. Figures 4.16 and 4.17 show $Q - F_p$ and C-V curves plotted for two different values of R_s . The $Q - F_p$ curves are very similar. The only major distinction between them is during the relaxation portion of the waveform, where the field of the device simulated with the larger R_s has a lower field than the device with the smaller R_s . This lower average phosphor field is due to the larger voltage drop across R_s . The C-V curves of Fig. 4.17 are more revealing in terms of overshoot than the $Q - F_p$ curves. The

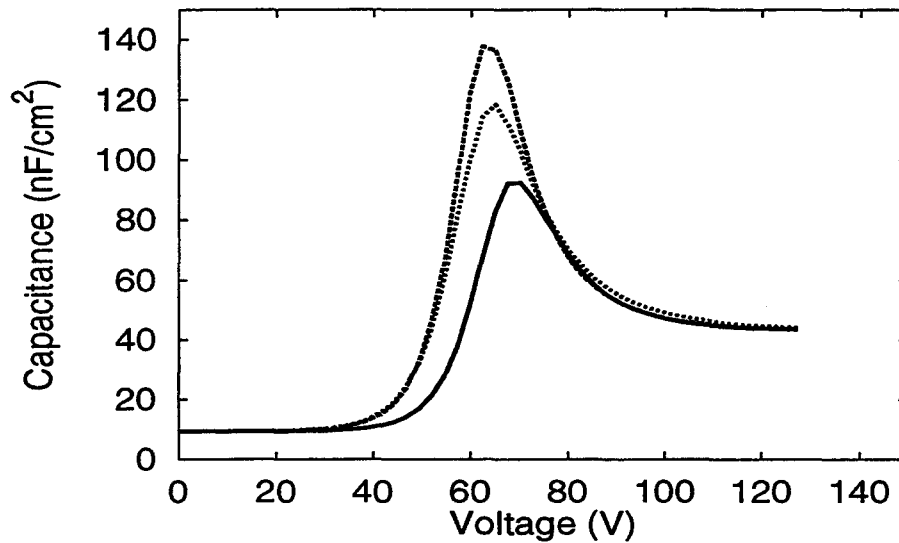


Figure 4.15: Family of simulated C-V curves with N_T set at $1.5 \times 10^{17} \text{cm}^{-3}$ (solid line), $2 \times 10^{17} \text{cm}^{-3}$ (dashed line), and $2.3 \times 10^{17} \text{cm}^{-3}$ (dotted line). Note that maximum C-V overshoot is obtained for the intermediate trap density case. Nominal simulation parameters are given in Table 4.2.

C-V curve for the device simulated with the larger R_s has more capacitance overshoot and also a larger turn-on voltage. The larger turn-on voltage is also due to the large voltage drop across R_s , which limits the voltage drop across the ACTFEL device.

Since the difference in maximum C-V overshoot between the two curves of Fig. 4.17 is about $25 \frac{nF}{cm^2}$, a greater difference in the $Q - F_p$ curves than shown by the two curves of Fig. 4.16 is expected. From experimental data, $Q - F_p$ and C-V overshoot have been demonstrated to be directly correlated. Experimentally, a device showing more C-V overshoot than another is expected to show more $Q - F_p$ overshoot, and vice-versa. The simulated results presented in Figs. 4.16 and 4.17 do not show this same trend. The similarity of these two $Q - F_p$ curves appears to result from a peculiarity of the simulation program related to the calculation of the external test circuit effects. This peculiarity is discussed in more detail later.

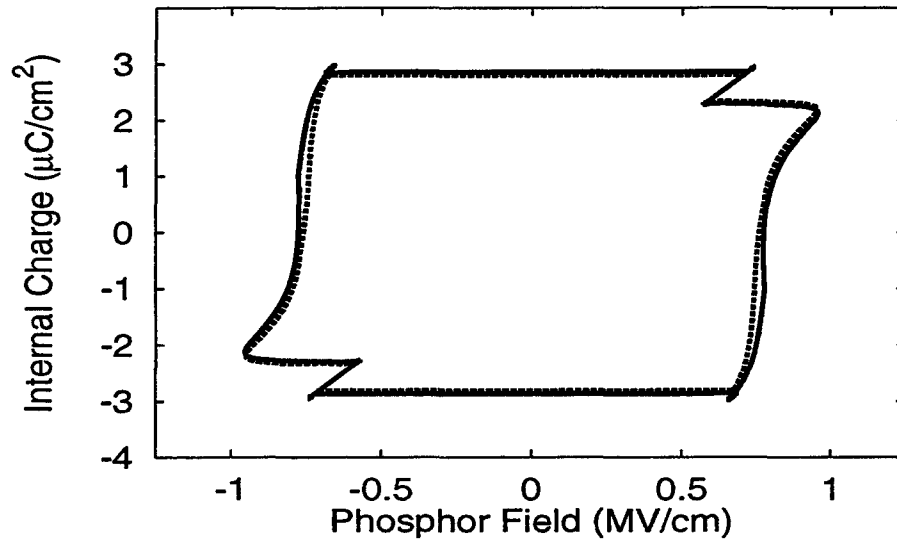


Figure 4.16: Simulated $Q - F_p$ curves with R_s varied from 400Ω (solid line) to 1000Ω (dashed line). Nominal simulation parameters are given in Table 4.2.

One of the key model parameters that influences the space charge emission profile (Fig. 4.8) is the characteristic field for trap-to-band impact ionization, f_{0t} . Setting f_{0t} to a small value causes trap-to-band impact ionization to occur at a smaller electric field if carriers are present, leading to a very large space charge emission rate precisely at device turn on. A larger f_{0t} leads to a broader space charge emission profile. Figures 4.18 and 4.19 show $Q - F_p$ and C-V curves plotted for different values of f_{0t} . The $Q - F_p$ curves show the interesting trend of increased average phosphor field for increased f_{0t} . The explanation for this effect is that the increased charge flow caused by the smaller characteristic field leads to a larger counterfield, and hence a smaller average phosphor field. Additionally, the curve with smallest f_{0t} has the most leakage charge. This is expected as this is the device with the most dynamic space charge.

As shown in Fig. 4.19, the intermediate C-V curve is again the one with the most overshoot. The reason for this is similar to the case in which N_T is varied - when too much

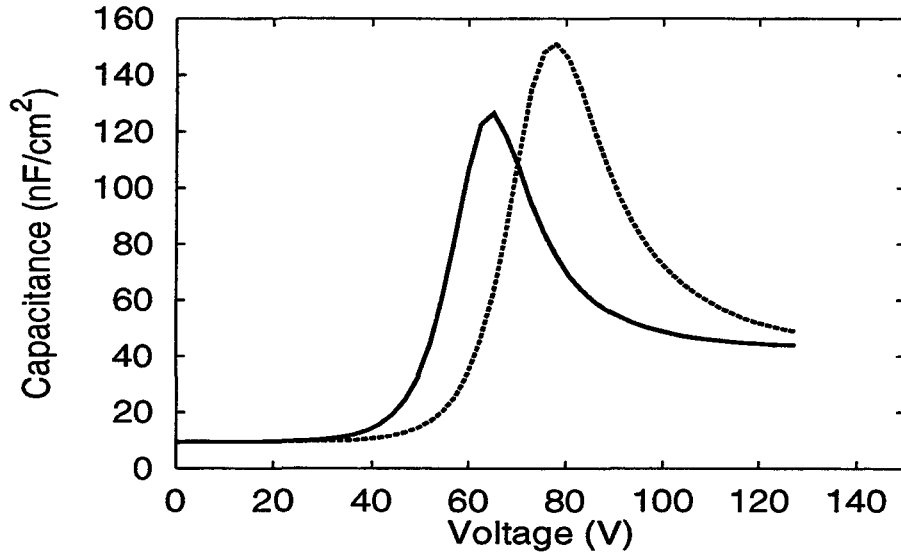


Figure 4.17: Simulated C-V curves with R_s varied from 400Ω (solid line) to 1000Ω (dashed line). Nominal simulation parameters are given in Table 4.2.

space charge is created, the counterfield becomes large and retards subsequent dynamic space charge creation. It is interesting to note that the parametric variations of both N_T and f_{0t} suggests that the effects of an increase in N_T are somewhat similar to a decrease in f_{0t} .

Band-to-band impact ionization is essentially a feedback effect that allows for stable device simulation when using the ACTFEL device model presented in this thesis. Figure 4.20 shows C-V curves plotted for different values of f_0 , the characteristic field for band-to-band impact ionization. Increasing f_0 decreases the importance of band-to-band impact ionization in the simulation. A reduced amount of band-to-band impact ionization means that the positive feedback effect of space charge creation by trap-to-band impact ionization dominates even more than usual. Greater values of f_0 lead to more capacitance overshoot, as shown in Fig. 4.20. Strangely, though, the $Q - F_p$ curves corresponding to the very different C-V curves of Fig. 4.20 are almost identical.

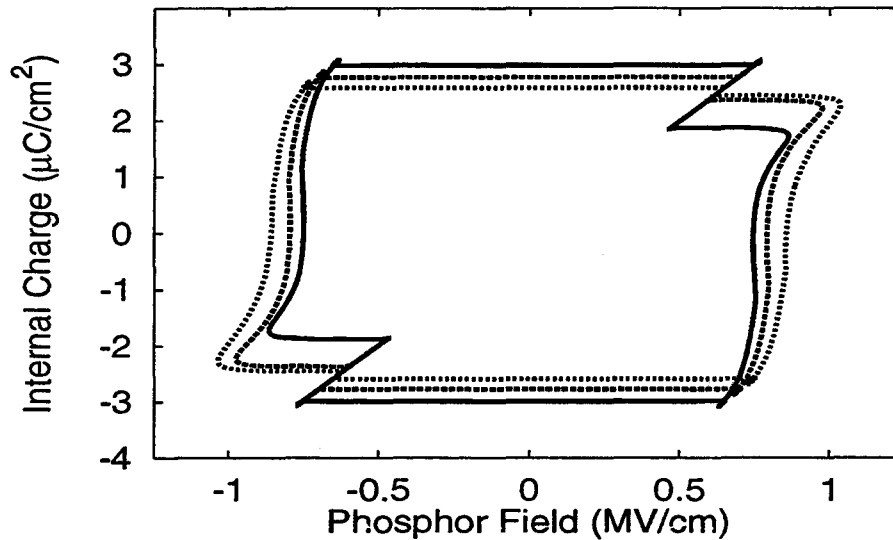


Figure 4.18: Family of simulated $Q - F_p$ curves with the characteristic field for trap-to-band impact ionization set at 2.6 MV/cm (solid line), 3.0 MV/cm (dashed line), and 3.4 MV/cm (dotted line). Nominal simulation parameters are given in Table 4.2.

The $Q - F_p$ curves corresponding to all three characteristic field values look almost exactly the same as the $Q - F_p$ curve of Fig. 4.11. As discussed previously, when a large difference in C-V overshoot is present, as in Fig. 4.20, differences in $Q - F_p$ overshoot are also expected. One possible reason for the lack of difference in $Q - F_p$ overshoot in this case is that the highest and lowest values for characteristic field for band-to-band impact ionization correspond to non-physical situations. Whether the simulated case is physically possible or not, however, C-V and $Q - F_p$ curves are mathematically related and should roughly correspond to each other. The discrepancy in this simulated case is probably related to the way in which the external circuit effects were added to the simulation program (see Sec. 3.5). The voltage dropped across the series resistor and sense capacitor elements is not solved for directly by the program's differential equation solver, but is instead computed in an iterative fashion. This method of solving for the

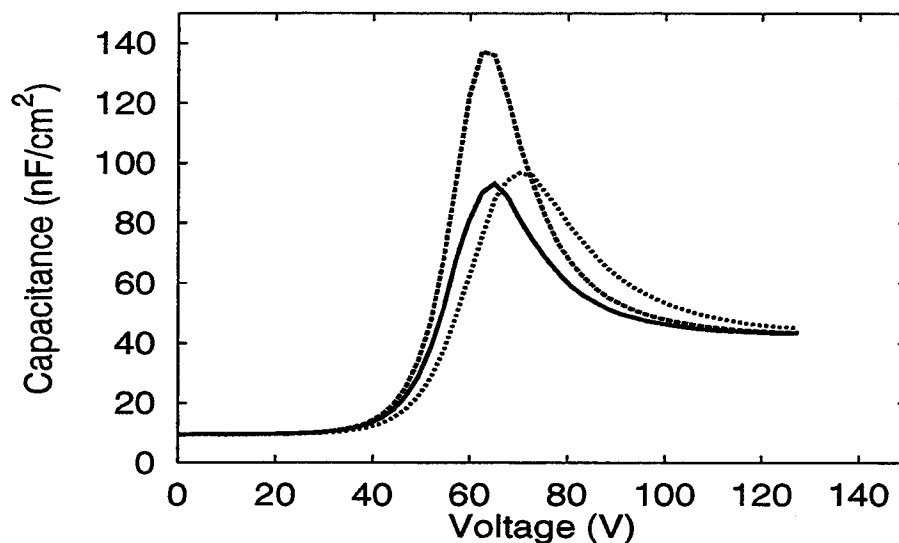


Figure 4.19: Family of simulated C-V curves with the characteristic field for trap-to-band impact ionization set at 2.6 MV/cm (solid line), 3.0 MV/cm (dashed line), and 3.4 MV/cm (dotted line). Nominal simulation parameters are given in Table 4.2.

circuit effects is not necessarily the preferred method, but was much less time consuming than rewriting the entire program. A by-product of the iterative process appears to be the strange lack of correlation between C-V and $Q - F_p$ overshoot as seen in Figs. 4.16 and 4.17 and in Fig. 4.20. More work needs to be done in order to understand this effect more completely.

Finally, Fig. 4.21 shows a family of $Q - F_p$ curves plotted for different values of characteristic field for electron capture, f_{0c} . f_{0c} is the field at which the probability of capture becomes zero; a larger f_{0c} leads to more electron capture. This trend is clearly visible in Fig. 4.21, as the most leakage charge flows in the device when the smallest value of f_{0c} is used. These $Q - F_p$ curves show that electron capture effects the shape of the curve during all portions of the applied waveform, so capture processes play an important role in ACTFEL device performance.

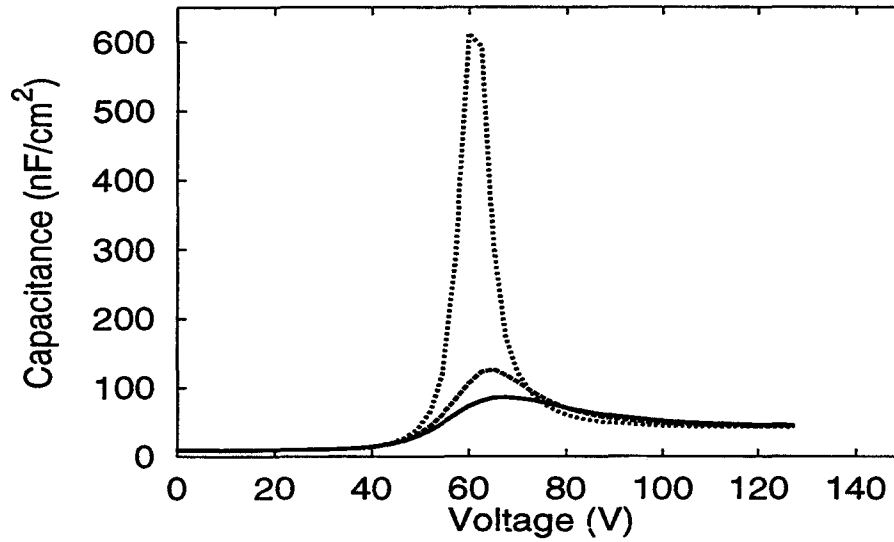


Figure 4.20: Simulated family of C-V curves with the characteristic field for band-to-band impact ionization set at 2.7 MV/cm (solid line), 3.1 MV/cm (dashed line), and 4.0 MV/cm (dotted line). $R_s = 600 \Omega$ for this plot. Note that maximum overshoot is obtained for the intermediate characteristic field value. Nominal simulation parameters are given in Table 4.2.

4.4.3 Simulation With Space Charge Creation by Field Emission

Including the effects of the test circuit yields reasonable simulation results when space charge is created through trap-to-band impact ionization, so it seems logical to expect improved results from the field emission program when effects of the test circuit are also considered. Figure 4.22 contains a $Q - F_p$ curve generated using a version of the field emission program modified to include the effects of the test circuit. The parameters used to generate this $Q - F_p$ curve are similar to those shown in Table 4.1, with the addition of a series resistance of 500Ω and a 101 nF sense capacitance. This $Q - F_p$ curve shows the characteristic effects of series resistance, as it is generally more rounded than the simulated curves presented in Sec. 4.2. The rounded look of this curve is not evidence of field overshoot, but is instead an effect caused by the fact that the voltage across the

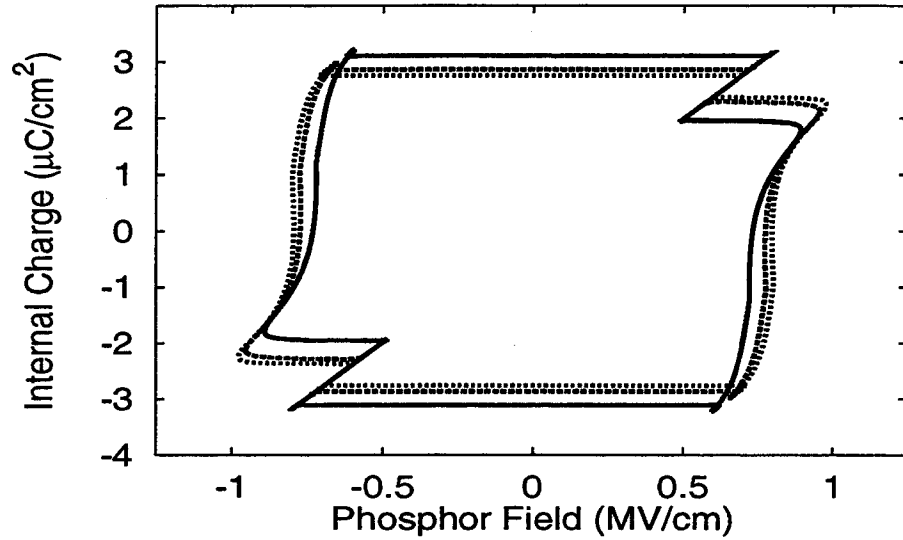


Figure 4.21: Family of simulated $Q - F_p$ curves with the characteristic field for electron capture set at 3 MV/cm (solid line), 5.0 MV/cm (dashed line), and 7.0 MV/cm (dotted line). Nominal simulation parameters are given in Table 4.2.

ACTFEL device is still increasing after the applied voltage has reached its maximum. Comparing the $Q - F_p$ curve of Fig. 4.22 to the $Q - F_p$ curves presented in Secs. 4.4.1 and 4.4.2 shows the distinct differences between real phosphor field overshoot and the RC effect of Fig. 4.22. Likewise, using the field emission program with circuit effects included does not yield significant capacitance overshoot when simulating C-V curves, as shown in Fig. 4.23. No more than a few $\frac{nF}{cm^2}$ of capacitance overshoot is ever obtained in C-V simulation no matter what model parameters are used.

The reason why $Q - F_p$ and C-V overshoot are not obtained when using the field emission program, even when the effects of the test circuit are considered, is because the broad field emission space charge creation profile does not lead to overshoot, as discussed in Sec. 4.3. By placing the space charge sheets very close to the insulator-phosphor interfaces and making the phosphor trap depth significantly smaller than the interface

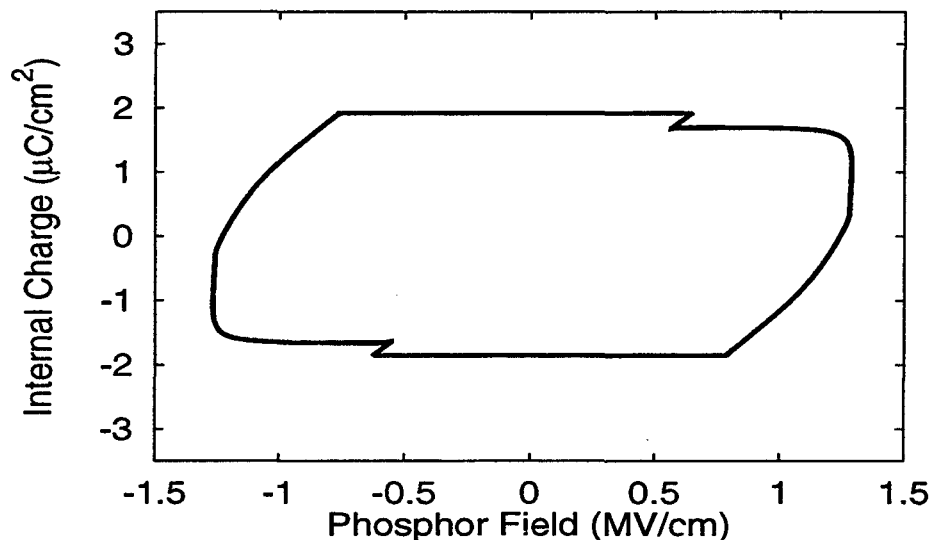


Figure 4.22: Simulated $Q - F_p$ curve obtained using the two-sheet charge model with space charge creation by field emission and effects of the test circuit considered for a SrS ACTFEL device

trap depth, it is possible to obtain some overshoot with the field emission program with circuit effects included. Using a small phosphor trap depth leads to a substantial amount of dynamic space charge creation prior to device turn-on. This space charge creation increases the cathode field and leads to a harder turn on than expected, giving rise to overshoot. Maximum overshoot is obtained when the space charge sheets are placed close to the interfaces because this leads to larger cathode fields, and hence more charge flow at turn on. Experimental results do not suggest that much space charge is created prior to device turn-on, however, and the creation of space charge is likely throughout the phosphor region, not just near the insulator-phosphor interfaces. These facts make the parameters necessary to achieve overshoot using the field emission program unattractive.

With trap-to-band impact ionization as the mechanism for space charge creation, placing the space charge sheets close to the interfaces is not necessary to achieve overshoot. This is because the amount of space charge created by multiplication is a function of the

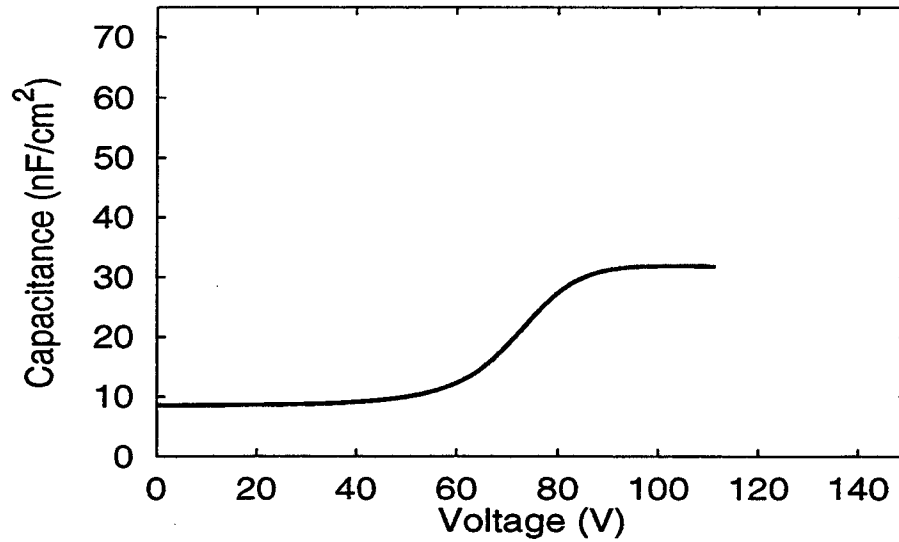


Figure 4.23: Simulated C-V curve obtained using the two-sheet charge model with space charge creation by field emission and effects of the test circuit considered for a SrS ACTFEL device.

distance traveled across the phosphor region, and not just the magnitude of the phosphor field.

4.4.4 Summary of Simulation Results

In this chapter an ACTFEL device model is presented which allows the simulation of devices with both $Q - F_p$ and C-V overshoot. Maximum overshoot is obtained when a simulation model with space charge creation by trap-to-band impact ionization is used. The importance of the effects of the experimental test circuit, particularly the series resistor, are also demonstrated. Inclusion of R_s in the simulation leads to more C-V overshoot, and a more realistically shaped $Q - F_p$ curve. The simulation results presented also demonstrate that field emission from bulk traps as a mechanism for space charge creation does not provide a sufficient amount of overshoot to agree with SrS ACTFEL device experimental characteristics.

Despite the achievements of the simulation model presented herein, it is still not at the level of complexity necessary to reproduce every subtle feature of experimental $Q - F_p$ curves. More work is required to accomplish an accurate trap-to-band impact ionization ACTFEL device model. In particular, electron capture needs to be modeled more realistically, and a new expression for phonon-assisted tunneling should be implemented. Additionally, band-to-band impact ionization and hole capture should be investigated as an additional mechanism for space charge creation. Finally, the $Q - F_p$ overshoot peculiarity associated with the external circuit effects should be investigated further.

5. CONCLUSIONS AND RECOMMENDATIONS FOR FUTURE WORK

This chapter presents a summary of the results achieved during the work accomplished in this thesis as well as suggestions for future work.

5.1 Achievements

The main reason for undertaking the simulation work presented in this thesis was to assess whether integration of trap-to-band impact ionization into a two-sheet charge model could account for the extremely large amounts of $Q - F_p$ and C-V overshoot measured experimentally in SrS:Ce ACTFEL devices. Previous two-sheet charge simulation work with field emission from bulk traps as a mechanism for space charge creation led to very limited amounts of overshoot, at best. Thus, the primary result of this thesis is the formulation of a trap-to-band impact ionization simulation program that implements the two-sheet charge model, as described in Chapter 3, and demonstrates conclusively that trap-to-band impact ionization is a viable overshoot mechanism. However, it is also found that large amounts of $Q - F_p$ and C-V overshoot can only be obtained in simulation when the effect of the series resistor in the measurement circuit is included in the simulation. Additionally, it is demonstrated that space charge creation by field emission cannot give rise to the large amounts of $Q - F_p$ and C-V overshoot measured experimentally, even when the series resistor measurement circuit effects are included. Several simulation trends in the model parameters have also been obtained. Specifically, the amount of dynamic space charge created is strongly dependent on the trap concentration in the phosphor region and on the characteristic field for trap-to-band impact ionization. The amount of C-V overshoot is a strong function of the characteristic field for band-to-band impact ionization, but also increases with increasing series resistance. Including the effects of the series resistance of the measurement circuit makes much more realistic ACTFEL device

simulation possible than before, but the model still has several inadequacies which need to be addressed.

5.2 Recommendations for Future Work

During the course of assembling the collection of simulation curves presented in Chapter 4, several weaknesses of the current model were revealed. One of the main weaknesses of the current model is the form of the equation used for electron capture (Eq. 3.72). This equation does not allow for an abrupt enough transition between electric field regimes in which capture is likely or unlikely. As a result, most values of f_{0c} lead to either too much electron capture during the rising portion of the applied voltage pulse or not enough capture during the interpulse intervals. Perhaps equations of the form suggested by Buchanan for SiO₂ (Eq. 3.76) should be investigated. [21] Not only is electron capture not handled realistically, but the capture of holes created through band-to-band impact ionization is not allowed in the current model. All in all, capture processes should be handled in a more sophisticated way in order to improve simulation accuracy.

The expression used for phonon-assisted tunneling in the current model (Eq. 3.41) is also problematic. Recent work by Hitt [13] has yielded a more realistic expression for the interface emission rate due to phonon-assisted tunneling, which should be incorporated into future versions of the model.

The results attainable using the current model are also somewhat limited by the number of space charge sheets. Two sheets allow for reasonably accurate simulation of dynamic space-charge creation, but much more information about static space charge could be gained with a larger number of sheets. With an n-sheet charge model it would be possible to plot the static space charge profile versus distance across the phosphor region, and to observe more accurately the locations in the phosphor region where impact ionization and electron capture occur.

The simulation program would also probably work better if it were re-written such that the differential equation solver solved for not just the electric fields in the phosphor

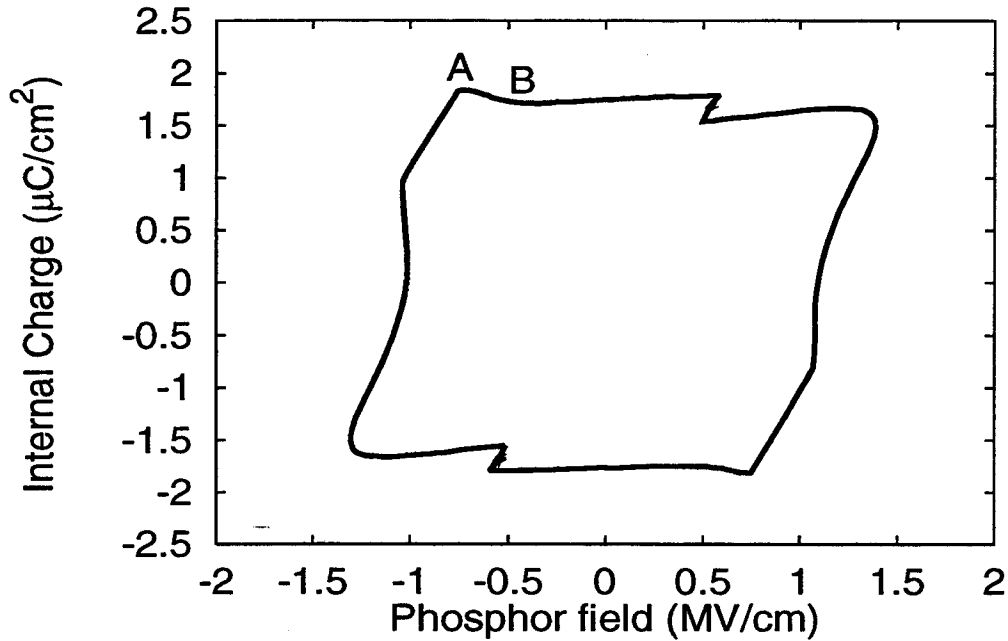


Figure 5.1: Experimental $Q - F_p$ curve demonstrating charge collapse.

region, but also for the voltage dropped across the insulator layers and the external circuit elements. This would allow the electrical characterization curves to be calculated the same way they are when taking experimental data; from the voltage across the sense capacitor. Taking the electrical characterization curves in this way would also likely eliminate the $Q - F_p$ overshoot peculiarities currently observed when certain simulation parameters are used.

A final weakness of the current model is that it cannot account for the charge collapse phenomenon that is sometimes observed in experimental $Q - F_p$ curves for SrS:Ce ACTFEL devices. Charge collapse is a reduction in internal charge that occurs during the fall-time portion of an applied voltage pulse; e.g. the SrS:Ce $Q - F_p$ curve shown in Fig. 5.1 shows charge collapse between points A and B. Charge collapse is thought to be due to electron capture and re-emission from shallow, normally empty interface or bulk states.

As soon as the applied voltage begins to decrease from its maximum value, electrons are re-emitted from these shallow states, resulting in a reduction in internal charge. Modeling these shallow states should be an easy addition to the model, and would likely have little effect on simulation during the rest of the voltage waveform.

A good candidate for future work is to use simulation to determine whether band-to-band or trap-to-band impact ionization is the more likely mechanism for space charge creation in SrS ACTFEL devices. Taking experimental data at a variety of temperatures might give some insight into this question.

BIBLIOGRAPHY

1. J. M. Jarem and V. P. Singh, "A computationally simple model for hysteretic thin-film electroluminescent devices," *IEEE Trans. Electron Devices*, vol. ED-35, pp. 1834–1841, Nov. 1988.
2. K. A. Neyts, "Simple model for the hysteretic behavior of thin-film electroluminescent devices," *IEEE Trans. Electron Devices*, vol. 38, pp. 2604–2611, Dec. 1991.
3. P. D. Keir, "Modeling phosphor space charge in alternating-current thin-film electroluminescent devices," M.S. thesis, Oregon State University, 1995.
4. J. B. Peery, "State space modeling of alternating-current thin-film electroluminescent devices," M.S. thesis, Oregon State University, 1997.
5. W. E. Howard, O. Sahni, and P. M. Alt, "A simple model for the hysteretic behavior of ZnS:Mn thin-film electroluminescent devices," *J. Appl. Phys.*, vol. 53, pp. 639–647, Jan. 1982.
6. K. A. Neyts, D. Corlatan, P. De Visschere, and J. Van den Bossche, "Observation and simulation of space-charge effects and hysteresis in ZnS:Mn ac thin-film electroluminescent," *J. Appl. Phys.*, vol. 75, pp. 5339–5346, May 1994.
7. D. H. Smith, "Modeling a.c. thin-film electroluminescent devices," *J. Lumin.*, vol. 23, pp. 209–235, 1981.
8. J. P. Bender and J. F. Wager, "Alternating current thin-film electroluminescent device modeling via a spice fowler-norheim diode," *IEEE Trans. Electron Devices*, vol. submitted, 1999.
9. K. A. Neyts and P. De Visschere, "Analytical model for thin-film electroluminescent devices," *J. Appl. Phys.*, vol. 68, pp. 4163–4171, Oct. 1990.
10. V. P. Singh and W. Z. Majid, "Effect of bulk space charge on the current and luminescence characteristics of zns:mn actfel display devices," *IEEE Trans. Electron Devices*, pp. 130–133, 1991.
11. V. P. Singh, W. Z. Majid, and D. C. Morton, "Analysis of zns:mn-typs ac thin-film electroluminescent devices with bulk space charge," *Journal of the SID*, vol. 1, no. 2, pp. 135–141, 1993.
12. J. M. Jarem and V. P. Singh, "Mechanism of electroluminescence in alkaline-earth sulfide actfel devices," *SID Digest*, vol. 19, pp. 27–30, 1988.
13. J. C. Hitt, Private communication, Feb. 1999.

14. A. S. Grudzinsky, "Simulations of electrical characteristics of SrS:Ce actfel devices with two-sheet space charge model," *unpublished paper*.
15. E. Bringuier, "Charge transfer in ZnS-type electoluminescence," *J. Appl. Phys.*, vol. 66, pp. 1314 – 1325, Aug. 1989.
16. G. Vincent, A. Chantre, and D. Bois, "Electric field effect on the thermal emission of traps in semiconductor junctions," *J. Appl. Phys.*, vol. 50, pp. 5484–5487, Aug. 1979.
17. E. Rosencher, V. Mosser, and G. Vincent, "Transient-current study of field-assisted emission from shallow levels in silicon," *Phys. Rev. B*, vol. 29, pp. 1135–1147, Feb. 1984.
18. A. W. Livingstone and J. W. Allen, "Impact ionization of deep impurities in zinc selenide," *J. Phys. C: Solid State Phys.*, vol. 6, pp. 3491–3500, 1973.
19. E. Bringuier, "Electron multiplication in zns-type electroluminescent devices," *J. Appl. Phys.*, vol. 67, no. 3, pp. 7040 – 7044, 1990.
20. D. J. Robbins, "Aspects of the theory of impact ionization in semiconductors (III)," *Phys. Stat. Sol.*, vol. 98, no. 11, pp. 11–36, 1980.
21. D. A. Buchanan, M. V. Fischetti, and D. J. DiMaria, "Coulombic and neutral trapping centers in silicon dioxide," *Phys. Rev. B*, vol. 43, pp. 1471–1486, Jan. 1991.
22. B. P. Flannery, W. H. Press, S. A. Teukolsky, W. T. Vetterling, *Numerical methods in C*. pp. 734–747, 1993.